



Delft University of Technology

Finding light in the darkness

Physics-based approaches for the manipulation of the QuasAr6a photocycle

Locarno, M.

DOI

[10.4233/uuid:7ac99b9f-38eb-4e13-8c2f-1a17abc15cd7](https://doi.org/10.4233/uuid:7ac99b9f-38eb-4e13-8c2f-1a17abc15cd7)

Publication date

2025

Document Version

Final published version

Citation (APA)

Locarno, M. (2025). *Finding light in the darkness: Physics-based approaches for the manipulation of the QuasAr6a photocycle*. [Dissertation (TU Delft), Delft University of Technology]. <https://doi.org/10.4233/uuid:7ac99b9f-38eb-4e13-8c2f-1a17abc15cd7>

Important note

To cite this publication, please use the final published version (if applicable).
Please check the document version above.

Copyright

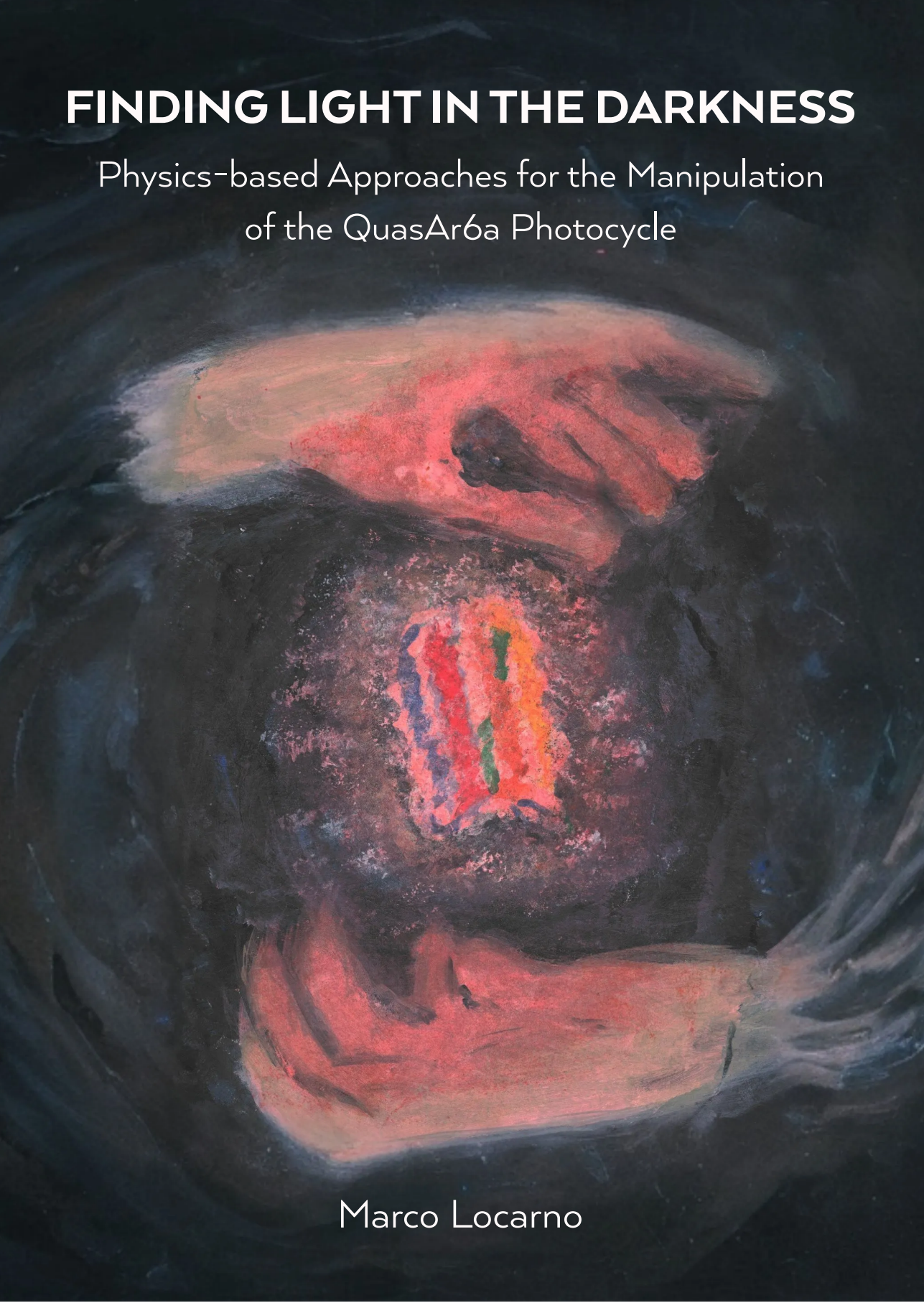
Other than for strictly personal use, it is not permitted to download, forward or distribute the text or part of it, without the consent of the author(s) and/or copyright holder(s), unless the work is under an open content license such as Creative Commons.

Takedown policy

Please contact us and provide details if you believe this document breaches copyrights.
We will remove access to the work immediately and investigate your claim.

FINDING LIGHT IN THE DARKNESS

Physics-based Approaches for the Manipulation
of the QuasAr6a Photocycle

An abstract painting of a face, possibly a self-portrait, set against a dark, textured background. The face is rendered with broad, expressive brushstrokes in shades of black, grey, and white. It features glowing red and orange highlights that suggest a fire or a setting sun. The eyes are particularly luminous, appearing as bright red and orange points of light. The overall mood is mysterious and dramatic, with the light elements contrasting sharply against the dark tones.

Marco Locarno

Propositions
accompanying the dissertation
FINDING LIGHT IN THE DARKNESS
by
Marco LOCARNO

1. The assumption that numerical simulations and quantum mechanics are necessary to describe plasmonic resonances is fundamentally false. *This proposition pertains to this dissertation.*
2. The perfect plasmonic nanoparticle morphology offering arbitrary tunability, thousandfold near-field enhancement and rotational robustness does not exist. *This proposition pertains to this dissertation.*
3. Coupling Genetically Encoded Voltage Indicators to resonant gold nanostars enables not only the manipulation of the proteins' fluorescence, but also of their conformational dynamics. *This proposition pertains to this dissertation.*
4. Unlike holistic models, reductionist photocycle models based on spectroscopic data provide incomplete insights.
5. Research in biosensor design will progress faster when the need for protein evolution is completely eliminated.
6. The rise of AI, adaptive learning, competency-based assessment and open science will inevitably drive the transformation of university structures and practices from a medieval social construct to modern, adaptable learning hubs.
7. Academic dress codes are archaic relics that reinforce elitism and prioritize appearance over intellectual achievement, and should therefore be abolished.
8. Eating cultured human meat is not ethically acceptable.
9. "They/them" are legitimate singular pronouns.
10. Spaghetti ≠ noodles.

These propositions are regarded as opposable and defendable, and have been approved as such by the promotor Prof. Dr. ir. J. P. Hoogenboom and the copromotor Dr. ir. D. Brinks.

FINDING LIGHT IN THE DARKNESS

**PHYSICS-BASED APPROACHES FOR THE
MANIPULATION OF THE QUASAR6A PHOTOCYCLE**

FINDING LIGHT IN THE DARKNESS

**PHYSICS-BASED APPROACHES FOR THE
MANIPULATION OF THE QUASAR6A PHOTOCYCLE**

Dissertation

for the purpose of obtaining the degree of doctor
at Delft University of Technology,
by the authority of the Rector Magnificus prof.dr.ir. T.H.J.J. van der Hagen,
chair of the Board for Doctorates,
to be defended publicly on
Thursday the 11th of September, 2025 at 12:30

by

Marco LOCARNO

Master of Science in Physics,
Università degli Studi di Genova, Genova, Italy,
born in Genova, Italy.

The dissertation has been approved by the promotores.

Composition of the doctoral committee:

Prof. Dr.ir. C. R. Kleijn,	Chairperson
Prof. Dr.ir. J.P. Hoogenboom,	Technische Universiteit Delft, promotor
Dr.ir. D. Brinks,	Technische Universiteit Delft, copromotor

Independent members:

Prof.dr. F.C. Grozema,	Technische Universiteit Delft
Prof.dr. L.D.A. Siebbeles,	Technische Universiteit Delft
Dr. S. Caneva,	Technische Universiteit Delft
Prof.dr. P. Zijlstra,	Technische Universiteit Eindhoven
Dr. O.S. Ojambati,	Universiteit Twente



Front & Back: Acrylic painting digitalized, by M. Locarno

Copyright © 2025 by M. Locarno

An electronic version of this dissertation is available available at
<http://repository.tudelft.nl/>.

*Life is a gradual series of revelations
That occur over a period of time.
It's not some carefully crafted story,
It's a mess and we're all gonna die.*

*If you saw a movie that was like real life
You'd be like "What the hell was that movie about?"
It was really all over the place.
Life doesn't make narrative sense.*

- Josh Groban

CONTENTS

Summary	xi
Samenvatting	xiii
1 Introduction	1
1.1 The photocycle of genetically encoded voltage indicators	2
1.2 Plasmonic enhancement	3
1.2.1 Excitation enhancement	4
1.2.2 Emission enhancement by LDOS engineering	4
1.2.3 Plasmonic hybridization	5
1.2.4 Plasmonic manipulation of the photocycle	5
1.3 Non-linear excitation	6
1.3.1 Ultrafast transitions in microbial opsins	8
1.3.2 Probing intermediate states with pump-probe experiments	8
1.3.3 Limitations of the canonical photocycle model	9
1.4 Thesis outline	10
2 Analytical calculation of plasmonic resonances	19
2.1 Introduction	20
2.2 Brief history of plasmonics	20
2.3 Classical derivation of plasmonic resonance	22
2.3.1 Drude model for metals	22
2.3.2 Quasi-Static Approximation	23
2.3.3 Generalization of the Clausius-Mossotti relation for ellipsoids	24
2.3.4 Plasmonic resonance	26
2.4 Beyond the Quasi-Static Approximation	29
2.4.1 Surface damping	29
2.4.2 Modified Long-Wavelength Approximation	30
2.5 Final remarks	33
3 Finite-Difference Time-Domain plasmonic simulations	39
3.1 On the method	40
3.1.1 Maxwell's equations in matter	40
3.1.2 Central difference approximation	41
3.1.3 Discretization of Maxwell's equations	42
3.2 Spherical gold nanoparticles	43
3.3 Smooth gold nanorods	44
3.4 Octahedral silver nanoparticles	47
3.5 Highly spiked gold nanostars	50
3.6 Realistic gold nanostars	51

3.7	Discussion and conclusions	55
4	Plasmonic enhancement of QuasAr6a	59
4.1	Introduction	60
4.2	Results	61
4.2.1	Particle design	61
4.2.2	Colloidal growth of nanostars	61
4.2.3	Calibration using Cyanine-5	63
4.2.4	Plasmonic enhancement in living cells	65
4.2.5	Plasmonic enhancement of protein function	66
4.3	Discussion	68
4.4	Methods	68
4.4.1	FDTD simulations	68
4.4.2	Colloidal synthesis	69
4.4.3	UV/Visible spectroscopy of gold nanostars colloid	69
4.4.4	MPTMS surface coating and nanoparticle immobilization	70
4.4.5	SEM/EDX characterization	70
4.4.6	SEM image analysis	70
4.4.7	Fluorescence assays in solution	71
4.4.8	Fluorescence spectroscopy assays on substrates	71
4.4.9	Supported lipid bilayer formation	71
4.4.10	TIRF microscopy	72
4.4.11	HEK293T culture	72
4.4.12	Lentivirus preparation and transduction	72
4.4.13	Widefield fluorescence microscopy	73
4.4.14	Whole-cell patch-clamp recordings	73
4.4.15	Photocycle modelling and simulation	74
4.5	Supplementary information	74
4.5.1	Individual simulations realistic nanostars	74
4.5.2	Energy-dispersive X-ray spectroscopy	75
4.5.3	Fröhlich-like shift due to PVP coating	76
4.5.4	Estimation of the quantum yield enhancement of Cy5	76
4.5.5	Estimation of the glycocalyx spacing effect	77
4.5.6	Photocycle fitting	78
5	Degenerate pump-probe non-linear excitation of QuasAr6a	87
5.1	Introduction	87
5.2	Theoretical framework for pump-probe excitation	88
5.2.1	Linear systems under pump-probe excitation	89
5.2.2	Non-linear systems in the weak-field regime	92
5.2.3	Non-linear systems under multi-photon excitation	94
5.3	Experimental setup design	96
5.4	Optical delay line calibration	97
5.5	Autocorrelation spatial imaging	100
5.6	Preliminary experiments on live cells	101
5.6.1	Autocorrelation regime	102

5.6.2	Molecular vibrations regime	103
5.6.3	Ultrafast transitions regime	104
5.7	Interpretation and future outlook	106
5.8	Methods	107
5.8.1	Iron iodate sample preparation	107
5.8.2	HEK293T culture	108
5.8.3	Lentivirus preparation and transduction	108
5.8.4	Multiphoton fluorescence microscopy	108
6	Conclusions, societal impact and future outlook	111
6.1	Key scientific contributions	112
6.2	Future outlook	113
6.3	Societal impact	114
6.4	Concluding remarks	116
Curriculum Vitæ		119
Acknowledgements		121

SUMMARY

This dissertation addresses one of the longstanding challenges in modern biomedical science: how to rapidly and precisely control the function of proteins in living cells. Traditionally, scientists have relied on genetic modifications to tweak proteins and improve their performance, but this approach has some inherent limitations in speed and adaptability. Instead, the work presented here explores an alternative strategy: manipulating the environment in which a protein operates to alter its behavior, rather than rewriting its genetic code. The study revolves around a genetically encoded voltage indicator known as QuasAr6a, a protein used to optically monitor electrical activity in cells, neurons in particular.

I first explain the problem of how minimal changes in a protein structure can dramatically alter its function. These changes often result from small mutations that can hinder or even completely disable the normal activity of the protein. This phenomenon, known as the sequence-structure-function paradigm, presents a major bottleneck when trying to engineer proteins with improved performance. In contrast to the conventional approach of inducing mutations, I propose the physical manipulation of the conditions around the protein to influence its behavior. This idea opens a new way of thinking about protein engineering, one that borrows concepts from other scientific fields to enhance biological function.

To explore this idea, I first developed a solid theoretical foundation. The early chapters offer an in-depth analytical treatment of how light interacts with metal nanoparticles, tiny particles that optically resonate when exposed to electromagnetic waves. Using classical models such as the Drude model and the Quasi-Static approximation, I derived equations that describe how these particles absorb and scatter light. A noteworthy achievement is the generalization of the Clausius-Mossotti relation to account for the shape and size of nanoparticles, leading to a robust model that predicts the behavior of metal nanoparticles under various conditions. This framework not only forms a reference for the study, but it also contributes valuable insights to the broader field of nanophotonics.

Building on these theoretical models, I then focused on numerical simulations. Using Finite-Difference Time-Domain (FDTD) methods, the study simulates the optical properties of nanoparticles with a variety of shapes, such as spheres, rods and spiked structures known as nanostars. These simulations revealed that nanostars, thanks to their sharp tips, are particularly effective at concentrating light into very small regions, dramatically enhancing the local electric field. This property is essential because it suggests that by carefully designing these nanoparticles, one can significantly amplify the fluorescence signal emitted by proteins like QuasAr6a.

Armed with these theoretical and numerical insights, I moved on to the application of nanostars to fluorescent living cells. In one set of experiments, gold nanostars were synthesized using advanced colloidal growth techniques. These nanostars were

designed to interact with QuasAr6a proteins expressed in living cells. The experiments demonstrated that by coupling the proteins to the plasmonic nanostars it is possible to enhance the fluorescence intensity and even modify the response speed of the proteins to electrical signals. This enhanced performance could be crucial for improving voltage imaging in neuroscience. The experiments show that the spatial arrangement between the nanostars and the proteins is the most critical factor: even minor differences in their relative positions can significantly affect the overall plasmonic enhancement. Through a series of fluorescence assays and live cell imaging, I identified the mechanism behind performance manipulation via plasmonic coupling. It became clear that the photocycle, the series of light-induced conformational changes that the protein undergoes, underlies any measurable effect.

Finally, I decided to study the first photoactivated transition in the photocycle with ultrafast optical techniques. In the last experimental chapter I explain the degenerate pump–probe method, where pairs of identical broadband laser pulses are used to excite the protein. This technique allowed me to probe the ultrafast dynamics of the protein. By adjusting the delay between the pulses on timescales ranging from fractions of a femtosecond up to the nanosecond, I discovered a non-linear response that was not apparent under conventional excitation methods. These ultrafast experiments give a hint of how the energy landscape of the protein can be manipulated, opening the possibility of controlling its function on timescales previously thought to be inaccessible.

The results I collected are both promising and thought-provoking. The analytical models and simulations validate the concept that physical manipulation can effectively alter the photocycle of fluorescent proteins. Experimentally, the coupling of nanostars to QuasAr6a in living cells leads to a measurable improvement in fluorescence signal and response speed, suggesting that this approach could significantly enhance voltage imaging techniques. Furthermore, the pump–probe experiments reveal non-linear behaviors that hint at the possibility of even more finely tuned control over protein dynamics in the future. The work suggests that by exploiting the principles of plasmonics and ultrafast optics it is possible to overcome the limitations imposed by traditional genetic engineering.

The potential applications of my research are far-reaching. In neuroscience, for example, enhanced voltage imaging could lead to breakthroughs in understanding the complex electrical activities of neurons, leading to better diagnosis and treatment of neurological disorders.

We are approaching a future where the boundaries between physics, biology and engineering are increasingly blurred. Approaching biological challenges from a multidisciplinary, holistic perspective holds immense potential and sets the stage for further advances that could fundamentally change how we interact with and manipulate biological systems.

SAMENVATTING

Dit proefschrift behandelt één van de langlopende uitdagingen in de moderne biomedische wetenschap: hoe kan de functie van eiwitten in levende cellen snel en nauwkeurig worden veranderd. Traditioneel hebben wetenschappers vertrouwd op genetische modificaties om eiwitten aan te passen en hun prestaties te verbeteren, maar deze benadering kent inherente beperkingen op het gebied van snelheid en aanpasbaarheid. In plaats daarvan verkent het hier gepresenteerde werk een alternatieve strategie: het manipuleren van de omgeving waarin een eiwit opereert om zo zijn gedrag te veranderen, in plaats van zijn genetische code te herschrijven. De studie draait om een genetisch gecodeerde spanningsindicator, bekend als QuasAr6a; dit is een eiwit dat wordt gebruikt om de elektrische activiteit in cellen optisch te monitoren, in het bijzonder in neuronen.

Ik begin met het uitleggen van het probleem: minimale veranderingen in de structuur van een eiwit kunnen zijn functie drastisch veranderen. Deze veranderingen zijn vaak het gevolg van kleine mutaties die de normale activiteit van het eiwit kunnen belemmeren of zelfs volledig uitschakelen. Dit fenomeen, bekend als het sequentie-structuur-functie paradigma, vormt een belangrijk knelpunt bij het ontwikkelen van eiwitten met verbeterde prestaties. In tegenstelling tot de conventionele benadering van het introduceren van mutaties, stel ik voor om de toestand rondom het eiwit fysiek te manipuleren om zo zijn gedrag te beïnvloeden. Dit idee opent een nieuwe manier van denken over eiwit-engineering, waarbij concepten uit andere wetenschappelijke disciplines worden overgenomen om de biologische functie te verbeteren.

Om dit idee te verkennen, ontwikkelde ik eerst een solide theoretische basis. De eerste hoofdstukken bieden een diepgaande analytische behandeling van hoe licht wordt beïnvloed door metalen nanodeeltjes, kleine deeltjes die optisch resoneren wanneer ze worden blootgesteld aan elektromagnetische golven. Met behulp van klassieke modellen zoals het Drude-model en de quasi-statische benadering leidde ik vergelijkingen af die beschrijven hoe deze deeltjes licht absorberen en verstrooien. Een opmerkelijke prestatie is de generalisatie van de Clausius-Mossotti-relatie waarbij er rekening gehouden wordt met de vorm en grootte van nanodeeltjes; dit leidt tot een robuust model dat het gedrag van metalen nanodeeltjes onder verschillende omstandigheden voorspelt. Dit raamwerk vormt niet alleen een referentie voor de studie, maar levert ook waardevolle inzichten voor het bredere veld van nanofotonica.

Voortbouwend op deze theoretische modellen richtte ik me vervolgens op numerieke simulaties. Met behulp van Finite-Difference Time-Domain (FDTD) methoden simuleert de studie de optische eigenschappen van nanodeeltjes met een verscheidenheid aan vormen, zoals bollen, staven en structuren met stekels, bekend als nanostars. Deze simulaties onthulden dat nanostars, dankzij hun scherpe punten, bijzonder effectief zijn in het concentreren van licht in zeer kleine gebieden, waardoor het lokale elektrische veld drastisch wordt versterkt. Deze eigenschap is essentieel en impliceert dat door het zorgvuldig ontwerpen van deze nanodeeltjes het fluorescentiesignaal dat door eiwitten

zoals QuasAr6a wordt uitgezonden, aanzienlijk kan worden versterkt.

Gewapend met deze theoretische en numerieke inzichten ben ik overgegaan tot de toepassing van nanostars op fluorescerende levende cellen. In een reeks experimenten werden gouden nanostars gesynthetiseerd met behulp van geavanceerde colloïdale groeitechnieken. Deze nanostars waren ontworpen voor beïnvloeding van QuasAr6a-eiwitten die in levende cellen tot expressie komen. De experimenten toonden aan dat door de eiwitten te koppelen aan de plasmonische nanostars het mogelijk is de fluorescentie-intensiteit te verhogen en zelfs de responsnelheid op elektrische signalen van de eiwitten te wijzigen. Deze verbeterde prestaties zouden cruciaal kunnen zijn voor het verbeteren van spanningsbeeldvorming in de neurowetenschappen. De experimenten laten zien dat de ruimtelijke ordening tussen de nanostars en de eiwitten de meest kritische factor is: zelfs kleine verschillen in hun relatieve posities kunnen de algehele plasmonische versterking aanzienlijk beïnvloeden. Door middel van een reeks fluorescentie-protocollen en live cell imaging identificeerde ik het mechanisme achter de prestatieverandering via plasmonische koppeling. Het werd duidelijk dat de fotocyclus, de reeks licht-geïnduceerde conformatieele veranderingen die het eiwit ondergaat, ten grondslag ligt aan elk meetbaar effect.

Ten slotte besloot ik de eerste foto-geactiveerde overgang in de fotocyclus te bestuderen met ultra snelle optische technieken. In het laatste experimentele hoofdstuk leg ik de degenerate pump-probe methode uit, waarbij paren identieke breedbandige laserpulsen worden gebruikt om het eiwit te exciteren. Deze techniek stelde mij in staat de ultra snelle dynamiek van het eiwit te onderzoeken. Door de vertraging tussen de pulsen af te stellen op tijdschalen variërend van fracties van een femtoseconde tot de nanoseconde, ontdekte ik een niet-lineaire respons die niet zichtbaar was bij conventionele excitatiemethoden. Deze ultra snelle experimenten geven een aanwijzing hoe het potentiaal-landschap van het eiwit gemanipuleerd kan worden, waardoor de mogelijkheid ontstaat om zijn functie te regelen op tijdschalen die voorheen als ontoegankelijk werden beschouwd.

De resultaten die ik heb verzameld, zijn veelbelovend en stemmen tot nadenken. De analytische modellen en simulaties bevestigen het concept dat fysieke manipulatie de fotocyclus van fluorescerende eiwitten effectief kan veranderen. Experimenteel leidt de koppeling van nanostars aan QuasAr6a in levende cellen tot een meetbare verbetering van het fluorescentiesignaal en de responsnelheid, wat suggereert dat deze benadering de spanningsindicatie-technieken aanzienlijk zou kunnen verbeteren. Bovendien ont-hullen de pump-probe experimenten niet-lineaire gedragingen die wijzen op de mogelijkheid van nog fijner afgestemde controle over de eiwitdynamica in de toekomst. Het werk suggereert dat door het benutten van de principes van plasmonica en ultra snelle optica het mogelijk is de beperkingen te overwinnen die door traditionele genetische engineering worden opgelegd.

De potentiële toepassingen van mijn onderzoek zijn verstrekkend. Bijvoorbeeld, in de neurowetenschappen zou verbeterde spanningsbeeldvorming kunnen leiden tot doorbraken in het begrijpen van de complexe elektrische activiteiten van neuronen, wat zou bijdragen aan een betere diagnose en behandeling van neurologische stoornissen.

Wij naderen een toekomst waarin de grenzen tussen natuurkunde, biologie en engineering steeds meer vervagen. Het benaderen van biologische uitdagingen vanuit een

multidisciplinaire, holistische invalshoek biedt enorme potentie en kan de basis voor verdere wetenschappelijke vooruitgang in het manipuleren van biologische systemen fundamenteel veranderen.

1

INTRODUCTION

When the COVID-19 pandemic hit and lockdowns froze the world in time, one question concerned everyone: when would life return to normal? In scientific terms, that meant one thing: when would a vaccine be available? History reminds us that for some diseases, such as human papilloma virus, decades of research were needed before a vaccine could be approved.¹ Yet, this time, with technologies like mRNA vaccines and viral vector platforms already in development, COVID-19 vaccines were distributed in just over a year.^{2,3} Now, imagine a world where every human disease, known or yet to be discovered, could be cured in a similarly short span. The quality of life would be dramatically improved, and only age might set a limit on life expectancy. The utopic vision of transforming biomedical research to achieve rapid, accurate and even personalized interventions has long inspired generations of doctors and scientists alike.

Despite unprecedented advances in our understanding of biology, a major bottleneck remains: the sequence–structure–function paradigm. A change in just one amino acid can drastically alter a protein’s structure, sometimes even preventing it from folding into a functional form.⁴ And when a structure changes, its function can be completely transformed too. For example, a single point mutation can dramatically shift an enzyme’s thermostability and function.⁵ In human biology, many diseases are caused by such small changes: the deletion of a single phenylalanine in the CFTR protein ($\Delta F508$) impairs its folding and trafficking, resulting in cystic fibrosis.⁶ In optogenetics, for instance, a single mutation in a light-sensitive ion channel may affect photocurrent, sensitivity, kinetics, spectral characteristics and photostability altogether.^{7,8,9} Biology does not progress along a smooth, continuous path: one cannot simply blend the genetic code of two perfectly functioning proteins and expect this intermediate to inherit a mixture of their properties. This inherent discontinuity hinders the necessary rapid development in protein engineering and biosensor development.

Now, imagine if we could unlock and control biological functions that were not efficient or altogether absent in nature, not by rewriting the genetic code but by modulating the environment in which proteins operate. What if, instead of relying solely on biology, we turned to physics, which offers a continuum of control? In optics, for exam-

ple, parameters such as the wavelength and intensity of a laser can be finely adjusted, nanoparticles can be engineered with precise size and composition, and even the time delay between laser pulses can be regulated with femtosecond precision. Such continuous tuning could provide a powerful alternative to the abrupt, unpredictable changes due to genetic mutations, and enable us to create "in-between states", conditions that do not exist naturally in biology but can be induced through physical manipulation.

Optics has always been at the heart of biomedical research. Fluorescence microscopy, for example, not only confirmed the cellular basis of life¹⁰ but also has been the key to countless discoveries in biology. Innovations such as light-sheet microscopy¹¹ and super-resolution imaging¹² have pushed temporal and spatial resolutions to their limits. Super-resolution techniques like single-molecule localization microscopy allow visualization at the nanoscale¹³ and groundbreaking methods like MINFLUX¹⁴ and MINSTED¹⁵ achieve molecular resolution. In this rich context, the integration of nanotechnology is already making its way into biomedical research. Smart nanomaterials can act as nanotransducers that absorb external energy (photons, magnetic fields, ultrasound) and release biochemical or physical signals to influence cell behavior.¹⁶ One team even managed to remotely trigger calcium-dependent insulin expression in beta cells of living mice by using magnetic nanoparticles and radio waves.¹⁷

Inspired by these advancements, our approach is grounded in the idea that, by using physical methods, we can manipulate biological function in ways that genetics alone cannot achieve. Instead of re-engineering a protein through mutations, we hypothesize we could alter its function by modulating the *environment* in which it operates. This thesis explores exactly that possibility by focusing on the manipulation of the function of fluorescent biosensors.

1.1. THE PHOTOCYCLE OF GENETICALLY ENCODED VOLTAGE INDICATORS

Genetically encoded voltage indicators (GEVIs) have emerged as useful tools in neuroscience for mapping fast electrical dynamics across neurons, from single synapses to large circuits.¹⁸ Their ability to optically capture membrane voltage changes at high speed has opened new possibilities in brain imaging. Achieving such performance, however, relies on the molecular mechanics of the protein's photocycle, the sequence of light-driven conformational transitions in the protein.^{18,19,20,21} In microbial rhodopsin-based GEVIs, this photocycle underpins how absorbed light energy is converted into a readable fluorescent signal, and understanding it is key to improving sensor speed and sensitivity.^{18,22}

Protein engineering aims at optimizing the features of GEVIs by altering their amino acid sequence. Typically, mutations are introduced to interrupt the normal ion transport cycle, creating a "detour" in the photocycle that favors a long-lived emissive state instead of quickly returning to the ground state via proton pumping.¹⁸ Traditional protein engineering strategies, which rely on directed evolution and high throughput screening, are inherently time-consuming and often yield suboptimal results. Among the many existing GEVIs,²³ the QuasAr family, evolved from the Archaeorhodopsin-3 microbial protein, has sparked interest due to its ability to rapidly and accurately transduce voltage

changes into changes in fluorescence.^{24,25,26}

In their physiological context, wildtype microbial rhodopsins are transmembrane proteins that function as light-driven ion pumps or channels.²² Absorbing a photon triggers isomerization of the covalently bound retinal chromophore, which in turn induces a cascade of conformational changes in the protein.¹⁸ These changes are organized into a series of intermediate states (often denoted by labels such as K, L, M, N, O in the case of bacteriorhodopsin^{27,28}) that each have distinct structural and spectral properties.¹⁸ For example, one intermediate may involve a deprotonated Schiff base and release of a proton on one side of the membrane, while a later state restores the proton to complete the cycle. The stability and transition rate of each state can be influenced by environmental factors, most importantly the transmembrane potential.¹⁸ An applied voltage can shift the equilibria or kinetics of certain steps, effectively modulating the photocycle progression. This is the biophysical principle behind voltage sensing: membrane potential alters the occupation of fluorescent and non-fluorescent states, causing the brightness of the GEVI to change under the influence of the membrane potential.

From a physics perspective, the photocycle can be mathematically modeled as a series of transitions between states using the finite-state continuous-time Markov chain formalism.^{27,28} Each transition has its own kinetic parameters, and by measuring the fluorescence in response to a stimulus in time we can infer the underlying dynamics. This formalism not only allows us to characterize the behavior of the system under standard conditions, but also provides a framework to predict how altering external factors might shift the balance between states.

By changing the environment in which the protein operates we hypothesize we can effectively modulate these kinetic transitions. The possibilities are nearly endless: one could adjust temperature, pH, pressure, local electromagnetic field or polarizability, membrane composition or curvature, buffer viscosity or viscosity gradient, and so forth. In this thesis, we apply physical methods to manipulate the photocycle of QuasAr6a. Instead of modifying the protein genetically, we explore two main approaches: plasmonic enhancement and ultrafast pump–probe excitation.

1.2. PLASMONIC ENHANCEMENT

Plasmonic nanoparticles are metal nanostructures that exhibit collective oscillations of conduction electrons when excited by light.²⁹ This phenomenon, known as localized surface plasmon resonance (LSPR), leads to the concentration of amplified electromagnetic fields at the nanoparticle's surface.

Essentially, any fluorophore positioned within the intense near-field of a plasmonic nanoparticle experiences a much higher effective light intensity than it would under the incident light alone.^{30,31} This means that a fluorophore near a plasmonic particle can absorb more photons due to the concentrated field.^{30,32,33} At the same time, the near-field can couple to the emission of the fluorophore, opening additional radiative pathways.^{30,32} These enhancements depend on the distance between the fluorophore and the metal nanostructure. Typically, fluorophores within a few to tens of nanometers from the metal experience the strongest field. If they are too far, the effect diminishes, and if they are too close, quenching of fluorescence can occur due to energy transfer to the metal.³²

Three distinct effects characterize plasmonic enhancement of fluorescence: excitation enhancement, emission enhancement and plasmonic hybridization. In the following sections, these effects are examined in detail to establish a comprehensive framework for understanding how plasmonic interactions can affect the photocycle.

1.2.1. EXCITATION ENHANCEMENT

When broadband light excites a metal nanoparticle, the LSPR causes the absorption and scattering cross-sections of the nanoparticle to become orders of magnitude larger than its physical size. This means the nanoparticle can capture and focus a wide-spectrum illumination, but selectively amplify only certain frequencies (those near the LSPR) in its near-field. Molecules in these “hotspots” experience a greatly increased excitation rate at the plasmonic resonance wavelength, compared to other off-resonant parts of the broadband spectrum.^{30,32,33}

The mechanism can be described by considering the molecule’s excitation rate Γ_{exc} as proportional to the local field intensity. One can show that:³²

$$\Gamma_{\text{exc}} \propto |\mathbf{p} \cdot \mathbf{E}_{\text{loc}}|^2 \quad (1.1)$$

where \mathbf{p} is the molecular transition dipole and \mathbf{E}_{loc} the local enhanced electric field where the molecule is located. This relation highlights that a molecule near a resonant nanoparticle (with large $|\mathbf{E}_{\text{loc}}|$) will have a much higher excitation probability than it would under the nominal incident field \mathbf{E}_0 .

In practice, plasmonic nanostructures can induce intensity enhancement factors of 10^2 – 10^4 in the near-field, dramatically increasing molecular absorption at the plasmon frequency.³³ Typical applications of this effect include surface-enhanced Raman scattering (SERS)^{34,35,36} and improved light-harvesting in solar cells.³⁵

1.2.2. EMISSION ENHANCEMENT BY LDOS ENGINEERING

When an excited molecule decays radiatively, the local density of optical states (LDOS) of its environment governs the emission rate. This is a direct consequence of Fermi’s golden rule, which states that the spontaneous transition rate Γ_r from an initial state $|i\rangle$ (excited molecule + no photon) to a final state $|f\rangle$ (ground-state molecule + emitted photon) is proportional to the photonic density of states $\rho(E_f)$ available for that transition:^{32,33}

$$\Gamma_r = \frac{2\pi}{\hbar} |\langle f | H' | i \rangle|^2 \rho(E_f) \propto |\mathbf{p} \cdot \mathbf{E}|^2 \rho(E_f) \quad (1.2)$$

where H' is the light-matter interaction Hamiltonian and $\rho(E_f)$ is the LDOS at the transition energy E_f . The subscript indicates that the decay process is radiative, as opposed to non-radiative processes.

In free space, $\rho(E_f)$ is low, so an excited molecule has a fixed spontaneous decay rate Γ_0 . In the proximity of a plasmonic nanoparticle, however, the LDOS can be dramatically higher due to the nanoparticle’s resonant modes. According to Eq. (1.2), increasing $\rho(E_f)$ increases the radiative transition rate. In other words, placing a fluorophore near a metal nanostructure can shorten its radiative lifetime and enhance its emission intensity,^{32,33} a phenomenon described as the Purcell effect in the context of resonant cavities.³⁷

It's important to note that the total decay rate $\Gamma = \Gamma_r + \Gamma_{nr}$ also includes non-radiative decay, corresponding to the energy dissipated as heat in the metal. Optimal LDOS engineering seeks to maximize Γ_r while minimizing additional Γ_{nr} losses. By keeping the emitter a few nanometers from the metal surface to avoid quenching, one observes a significant fluorescence enhancement: increased emission intensity and possibly modified spectra or directionality of emission. Pioneering experiments measured single-molecule emission near metal nanoparticles,^{31,32,33,38,39,40,41} confirming that emission rates follow LDOS changes as predicted by Fermi's rule.

1.2.3. PLASMONIC HYBRIDIZATION

Strong interactions between molecular transitions and plasmonic modes lead to the formation of hybridized states of light and matter. In the plasmonics community, the term "plasmonic hybridization" was first used to describe how different plasmon modes mix analogously to molecular orbital hybridization.⁴² For example, coupling between plasmons of two closely spaced nanoparticles⁴³ or between inner- and outer-surface plasmons in a metal nanoshell⁴⁴ gives rise to new resonance peaks that are shifted in energy relative to the original modes. In this hybridization framework, plasmons are treated like wavefunctions that can combine in-phase or out-of-phase, yielding bonding-like and anti-bonding-like plasmon modes (one lower in energy, one higher). This concept has a high impact on nano-optics because it lets us design complex plasmonic structures by intuitively "mixing" elementary plasmon modes, as much as chemists mix atomic orbitals to get molecular orbitals.

When a molecule is introduced into the picture, an even more striking form of plasmonic hybridization can occur: the molecule's exciton (electronic transition) can strongly couple with a plasmon resonance, forming delocalized hybrid excitations that are part molecule and part plasmon, called plexcitons.^{35,45} Under strong coupling conditions, the molecule and plasmon stop behaving as separate entities; instead, they generate new polariton states with energies split around the original transition energy. These plexcitons have altered transition energies resulting in the appearance of two distinct absorption peaks in place of one. This phenomenon is sometimes called "Rabi splitting".

Experiments have observed splitting energies on the order of hundreds of meV in plasmon-exciton systems. For instance, when J-aggregate dye molecules were coupled to metal nanorods, a spectral splitting ~ 200 meV was measured, indicating the formation of mixed states.⁴⁶ Additionally, single-molecule strong coupling in plasmonic nanocavities has been recently achieved at room temperature.⁴⁷

1.2.4. PLASMONIC MANIPULATION OF THE PHOTOCYCLE

In our work, gold nanostars are of particular interest because their sharp tips can produce extraordinarily high local field enhancements.^{48,49,50} We hypothesize these enhanced fields can interact with QuasAr6a to modulate its photocycle. The processes that predominantly contribute to the observations in this thesis are the excitation and the emission enhancement. The idea is that the intense near-fields around the nanoparticles can influence both the voltage sensitivity and the fluorescence intensity of the protein by altering specific transitions, whether conformational or electronic (**Fig. 1.1**). By tuning size, shape and material of the nanoparticles, we can optimize such interactions.

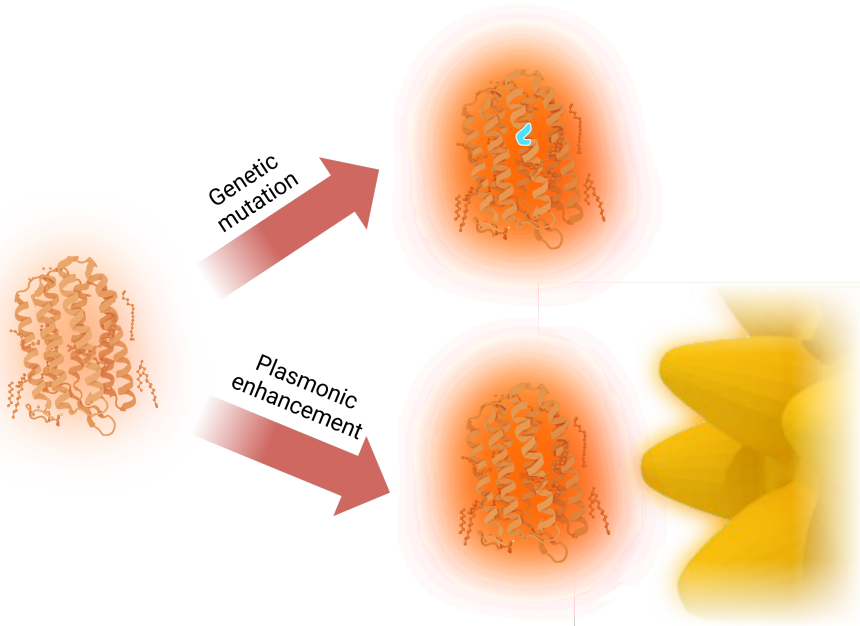


Figure 1.1: Protein engineering improves protein function through genetic mutation, while plasmonic enhancement interacts with proteins by modifying the electromagnetic nanoenvironment. Illustration made in BioRender.

1.3. NON-LINEAR EXCITATION

QuasAr6a can be driven through its photocycle by either 1-photon or 2-photon excitation, but these two modes have fundamentally different characteristics.^{51,52} In 1-photon excitation, a single high-energy photon directly stimulates the retinal chromophore from the ground state to an excited state, and the excitation probability increases linearly with light intensity. By contrast, 2-photon excitation employs two infrared photons that are absorbed simultaneously to reach an equivalent excited state via a virtual intermediate.⁵¹ Contextually, simultaneous means within a time delay smaller than the Heisenberg lifetime of the virtual state $\frac{\hbar}{E/2} = \frac{\lambda_{em}}{\pi c}$, where λ_{em} is the fluorescence emission wavelength and c the speed of light in vacuum, corresponding in the visible range to $\sim 10^{-15}$ s.⁵³ This makes 2-photon excitation a non-linear process, as the absorption rate depends on the square of the photon flux.

One practical consequence is that 2-photon excitation requires much higher photon densities to achieve the same excitation probability as 1-photon. In turn, 2-photon excitation is usually implemented with ultrafast pulsed lasers (femtosecond pulses) focused to a tight spot, which confines excitation to the focal volume only.⁵² Thus, unlike 1-photon excitation which can excite fluorophores along the entire light path, 2-photon excitation causes fluorescence only at the focal point, reducing out-of-focus excitation. This 3D localization of excitation is why 2-photon excitation is advantageous for imaging deep or thick samples with less background signal.⁵¹

The photocycle of QuasAr6a is initiated by a light-induced transition, yet the exact mechanisms and kinetics of this transition remain elusive, especially under 2-photon excitation, where the efficiency can be remarkably different compared to 1-photon conditions^{54,55} (Fig. 1.2). One hypothesis is that 1-photon and 2-photon excitation populate different excited states of the retinal and thereby influence which photochemical states are entered. From a physical perspective, 1-photon absorption follows the usual parity selection rules (allowing transitions from ground to excited states of opposite parity), whereas 2-photon absorption permits transitions that are parity-forbidden in 1-photon (therefore transitions between states of the same parity can become allowed).⁵⁶ This means 2-photon excitation can excite the retinal in ways that 1-photon excitation normally cannot.

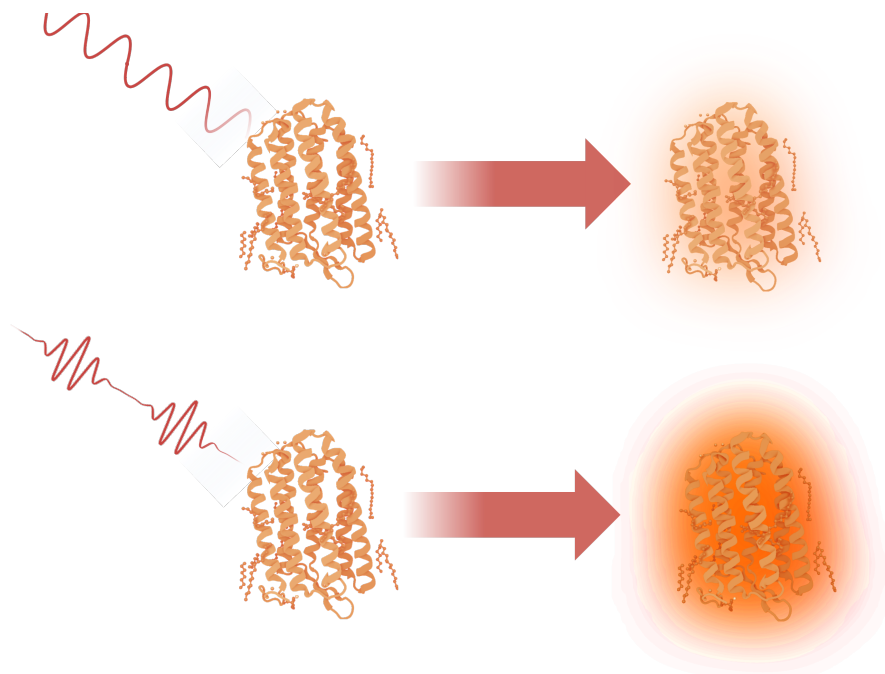
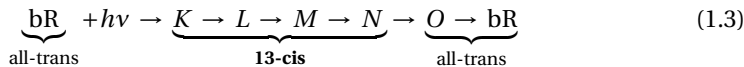


Figure 1.2: Protein performance under linear (above) and non-linear (below) excitation can vary significantly. The hypothesis is that the first transition of the photocycle is modified and, consequently, the function of a protein. Illustration made in BioRender.

We therefore hypothesize that there are non-linear processes involved, more complex than under continuous 1-photon illumination, and that by employing degenerate pump–probe excitation with femtosecond pulses we can probe these ultrafast dynamics. By controlling the delay between identical, phase-locked pulses, we aim to reveal and eventually manipulate the transition kinetics within the photocycle. To better understand the framework of the ultrafast experiments, the following sections will introduce important concepts like ultrafast transitions, intermediate state study with pump-probe excitation and the effect of retinal dynamics on voltage sensitivity.

1.3.1. ULTRAFAST TRANSITIONS IN MICROBIAL OPSINS

In the canonical photocycle model, the retinal chromophore of the opsin starts in its dark-adapted configuration, where it absorbs a photon. It then transitions through a series of photointermediate states before returning to the initial state. For example, bacteriorhodopsin (bR, a light-driven proton pump) follows a sequence often denoted as:^{18,22,27}



Each intermediate (K, L, M, N, O) has a characteristic retinal configuration and absorption maximum. The initial photoisomerization of retinal (all-trans to 13-cis) is extremely fast. In fact, femtosecond spectroscopy shows that retinal isomerization of bR happens on the order of ~ 500 fs.⁵⁷ Similar ultrafast primary events are seen in other microbial opsins: the same all-trans to 13-cis isomerization in channelrhodopsin-2 is ~ 600 fs, and in Anabaena sensory rhodopsin ~ 750 fs.⁵⁷ Such sub-picosecond transitions represent the formation of the earliest intermediate (often called K).

Subsequent intermediates form and decay on longer timescales. For instance, in Archaeorhodopsin-3 (Arch), an intermediate, analogous to N in bR, forms within tens of microseconds and decays with a time constant of ~ 390 μ s, while a later intermediate, analogous to O in bR, forms on the ~ 390 μ s and 4.1 ms timescales and decays in about 14 ms.⁵⁸ The ultrafast retinal twisting thus initiates a chain of slower thermal relaxations and proton transfers that define the canonical photocycle.

Notably, advanced techniques have even allowed coherent control over these ultrafast steps: in one study, femtosecond pulse shaping was used to enhance or suppress the yield of the 13-cis photoproduct in bR by $\sim 20\%$ relative to an unshaped pulse.⁵⁹ This demonstrates that the earliest sub-picosecond dynamics can significantly influence which intermediates are populated and the overall protein performance.

1.3.2. PROBING INTERMEDIATE STATES WITH PUMP-PROBE EXPERIMENTS

Pump-probe spectroscopy is a powerful method to resolve the short-lived intermediate states in the photocycle. In a pump-probe experiment, an initial ultrafast pump pulse excites the sample, triggering the photocycle, and a second time-delayed probe pulse monitors the state of the system.⁶⁰ By varying the pump-probe delay Δt , one can watch the population of intermediates rise and fall in real time, measuring their lifetimes. The probe detects changes in absorption, indicating the presence of specific intermediates at that delay.

The strength of this approach is that it can “stop the clock” at a chosen moment after excitation, capturing snapshots of the photocycle that are unobservable under continuous monochromatic excitation. This is crucial because many intermediates are transient, meaning they form and decay on picosecond to microsecond scales and never accumulate to detectable levels under continuous illumination.⁵⁸ Pump-probe experiments also enable access to states not reachable by a single pulse. A striking case is given by Arch: under a single pump pulse, the ground state does not yield fluorescence (since the primary photoproduct is non-fluorescent), however, by using a “probe” that serves as a secondary excitation, one can promote molecules that are in a metastable intermediate into an otherwise inaccessible excited state. More specifically, a single 640

nm pulse does not excite fluorescence, but a pump at 532 nm followed $\sim 20 \mu\text{s}$ later by a 640 nm probe produces a measurable fluorescent signal.⁵⁸ By adjusting the timing between pulses, one can effectively gate the excitation to a particular intermediate. Applying two closely spaced pump pulses before probing amplifies this effect, as more molecules are driven into an active photocycle, confirming the emergence of fluorescence from a multi-photon route.⁵⁸

Another advantage of using ultrafast pulses is that, to achieve pulses on the order of 100 fs, they must be broadband, with a typical FWHM of around 20 nm in wavelength. Timed, broadband sequences of pulses can unlock otherwise inaccessible states in a photocycle (Fig. 1.3). Pure monochromatic pulses, even if precisely timed, cannot excite the full range of intermediates. Simultaneous pulses at multiple wavelengths, on the other hand, lack the temporal gating needed for accessing the other photocycle states. This approach enables access to short-lived intermediates across a broad spectral range.

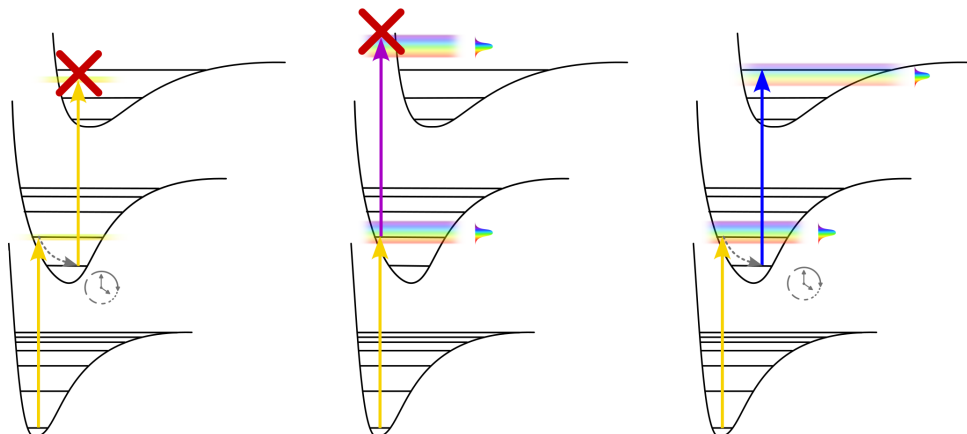


Figure 1.3: The use of timed, broadband pulses (right) allows the complete exploration of the energy states of complex molecules, inaccessible to timed but purely monochromatic pulses (left) or simultaneous pulses with different spectral components (center).

1.3.3. LIMITATIONS OF THE CANONICAL PHOTOCYCLE MODEL

While the canonical photocycle (Eq. (1.3)) is a useful framework, it oversimplifies retinal isomerization dynamics and protein conformational changes. For example, the standard model of bR assumes a single progression, but experiments have shown evidence of branched photocycles and additional intermediates.²⁸ Various studies at different temperatures and using different techniques have yielded conflicting formulations about intermediate states.⁶¹

Another simplification of the canonical model is that it often treats the retinal isomerization as an isolated, one-step event triggering subsequent protein changes. In truth, retinal's trajectory on the excited-state surface can involve multiple avoided crossings and intermediate minima.⁶² Moreover, the protein environment can actively steer these pathways: coherent control experiments demonstrated that by shaping the excitation pulse (hence altering the phases of vibrational modes), one can favor or suppress

certain product channels.⁵⁹

Changes in retinal isomerization dynamics can profoundly influence the protein conformations and thus its sensitivity to membrane voltage. In microbial rhodopsin-based voltage indicators like Arch, the voltage-sensitive optical signal arises not from the ground state, but from a particular photointermediate whose equilibrium is voltage-dependent.⁵⁸ If the retinal's isomerization dynamics are altered, the fraction of opsin in the protonated vs. deprotonated intermediate will change, and so will the voltage sensitivity.

Retinal isomerization is the trigger for protein conformational change, so any change in its dynamics could alter the timing and extent of protein motion. In channelrhodopsins, for example, the rate of isomerization and subsequent thermal steps determines how long the channel pore stays open or how quickly it inactivates.⁶³

In summary, while the canonical photocycle provides a useful starting point, there is plenty of room for model refinement to accurately capture and harness the complex interplay between isomerization and protein conformational changes to optimize voltage sensitivity.

1.4. THESIS OUTLINE

This dissertation is organized into six main chapters, each building on a specific aspect:

CHAPTER 2 – ANALYTICAL FOUNDATIONS

This chapter establishes the theoretical framework for plasmonic resonances in metal nanoparticles, necessary to guide rational design of nanoparticles resonant with the excitation and emission spectra of QuasAr6a. Using classical models such as the Drude model and the Quasi-Static Approximation, we derive a robust analytical model that accounts for material properties, nanoparticle geometry and environmental factors. Corrections for surface damping and dynamic depolarization are introduced, forming the basis for the subsequent numerical and experimental investigations.

CHAPTER 3 – FDTD SIMULATIONS

Recognizing the limitations of analytical models for complex nanoparticle geometries, this chapter employs Finite-Difference Time-Domain (FDTD) simulations to explore the optical properties of various nanoparticle shapes, including nanospheres, nanorods and nanostars. These simulations reveal that nanostars, with their sharp tips, provide the highest field enhancements, a critical insight that informs the design of nanoparticles for our biological application.

CHAPTER 4 – PLASMONIC ENHANCEMENT IN LIVING CELLS

This chapter translates the theoretical and numerical insights into practical applications by using gold nanostars to enhance the function of QuasAr6a in living cells. Through fluorescence assays and patch-clamp recordings, we demonstrate that plasmonic enhancement leads to brighter fluorescence and faster voltage-response kinetics. This work validates the central concept of using physical interventions to modulate protein function in a physiologically-relevant context.

CHAPTER 5 – ULTRAFAST PUMP–PROBE EXCITATION

In this chapter we extend our approach into the ultrafast domain by employing degenerate pump–probe spectroscopy to study the non-linear dynamics of the QuasAr6a photocycle. The chapter describes the design and calibration of an optical delay line capable of femtosecond precision, as well as the theoretical framework for distinguishing between linear and non-linear responses. Preliminary results suggest that non-linear behavior in the ultrafast regime may be exploited to further control the phototransitions in QuasAr6a.

CHAPTER 6 – CONCLUSIONS

The final chapter synthesizes the key scientific contributions, discusses the societal impact of the work and outlines future research directions. It emphasizes how the convergence of plasmonic enhancement and ultrafast spectroscopy can revolutionize voltage imaging and protein manipulation, setting the stage for transformative advances in biomedical sciences.

BIBLIOGRAPHY

- [1] Harald zur Hausen. "The search for infectious causes of human cancers: Where and why". In: *Virology* 392.1 (2009). ISSN: 00426822. DOI: [10.1016/j.virol.2009.06.001](https://doi.org/10.1016/j.virol.2009.06.001).
- [2] Gábor Tamás Szabó, Azita Josefina Mahiny, and Irena Vlatkovic. "COVID-19 mRNA vaccines: Platforms and current developments". In: *Molecular Therapy* 30.5 (2022). ISSN: 15250024. DOI: [10.1016/j.ymthe.2022.02.016](https://doi.org/10.1016/j.ymthe.2022.02.016).
- [3] Nicholas M. Provine and Paul Klenerman. "Adenovirus vector and mRNA vaccines: Mechanisms regulating their immunogenicity". In: *European Journal of Immunology* 53.6 (2023). ISSN: 15214141. DOI: [10.1002/eji.202250022](https://doi.org/10.1002/eji.202250022).
- [4] Ken A. Dill and Justin L. MacCallum. "The protein-folding problem, 50 years on". In: *Science* 338.6110 (2012). ISSN: 10959203. DOI: [10.1126/science.1219021](https://doi.org/10.1126/science.1219021).
- [5] Henry Dieckhaus et al. "Transfer learning to leverage larger datasets for improved prediction of protein stability changes". In: *Proceedings of the National Academy of Sciences of the United States of America* 121.6 (2024). ISSN: 10916490. DOI: [10.1073/pnas.2314853121](https://doi.org/10.1073/pnas.2314853121).
- [6] Patrick H. Thibodeau et al. "The cystic fibrosis-causing mutation ΔF508 affects multiple steps in cystic fibrosis transmembrane conductance regulator biogenesis". In: *Journal of Biological Chemistry* 285.46 (2010). ISSN: 00219258. DOI: [10.1074/jbc.M110.131623](https://doi.org/10.1074/jbc.M110.131623).
- [7] André Berndt et al. "Bi-stable neural state switches". In: *Nature Neuroscience* 12.2 (2009). ISSN: 10976256. DOI: [10.1038/nn.2247](https://doi.org/10.1038/nn.2247).
- [8] Lisa A. Gunaydin et al. "Ultrafast optogenetic control". In: *Nature Neuroscience* 13.3 (2010). ISSN: 10976256. DOI: [10.1038/nn.2495](https://doi.org/10.1038/nn.2495).
- [9] John Y. Lin. "A user's guide to channelrhodopsin variants: Features, limitations and future developments". In: *Experimental Physiology* 96.1 (2011). ISSN: 1469445X. DOI: [10.1113/expphysiol.2009.051961](https://doi.org/10.1113/expphysiol.2009.051961).
- [10] Howard Gest. "The discovery of microorganisms by Robert Hooke and Antoni van Leeuwenhoek, fellows of the Royal Society". In: *Notes and Records of the Royal Society* 58.2 (2004). ISSN: 17430178. DOI: [10.1098/rsnr.2004.0055](https://doi.org/10.1098/rsnr.2004.0055).
- [11] Ernst H.K. Stelzer et al. "Light sheet fluorescence microscopy". In: *Nature Reviews Methods Primers* 1.1 (2021). ISSN: 26628449. DOI: [10.1038/s43586-021-00069-4](https://doi.org/10.1038/s43586-021-00069-4).
- [12] Kirti Prakash et al. "Super-resolution microscopy: A brief history and new avenues". In: *Philosophical Transactions of the Royal Society A: Mathematical, Physical and Engineering Sciences* 380.2220 (2022). ISSN: 1364503X. DOI: [10.1098/rsta.2021.0110](https://doi.org/10.1098/rsta.2021.0110).

- [13] Mickaël Lelek et al. "Single-molecule localization microscopy". In: *Nature Reviews Methods Primers* 1.1 (Dec. 2021). ISSN: 26628449. DOI: [10.1038/s43586-021-00038-x](https://doi.org/10.1038/s43586-021-00038-x).
- [14] Roman Schmidt et al. "MINFLUX nanometer-scale 3D imaging and microsecond-range tracking on a common fluorescence microscope". In: *Nature Communications* 12.1 (2021). ISSN: 20411723. DOI: [10.1038/s41467-021-21652-z](https://doi.org/10.1038/s41467-021-21652-z).
- [15] Michael Weber et al. "MINSTED fluorescence localization and nanoscopy". In: *Nature Photonics* 15.5 (2021). ISSN: 17494893. DOI: [10.1038/s41566-021-00774-2](https://doi.org/10.1038/s41566-021-00774-2).
- [16] Giada Graziana Genchi et al. "Remote Control of Cellular Functions: The Role of Smart Nanomaterials in the Medicine of the Future". In: *Advanced Healthcare Materials* 6.9 (2017). ISSN: 21922659. DOI: [10.1002/adhm.201700002](https://doi.org/10.1002/adhm.201700002).
- [17] Sarah A. Stanley et al. "Remote regulation of glucose homeostasis in mice using genetically encoded nanoparticles". In: *Nature Medicine* 21.1 (2015). ISSN: 1546170X. DOI: [10.1038/nm.3730](https://doi.org/10.1038/nm.3730).
- [18] Xin Meng et al. "Voltage Imaging with Engineered Proton-Pumping Rhodopsins: Insights from the Proton Transfer Pathway". In: *ACS Physical Chemistry Au* 3.4 (2023). ISSN: 26942445. DOI: [10.1021/acspyschemau.3c00003](https://doi.org/10.1021/acspyschemau.3c00003).
- [19] Alfons Penzkofer, Arita Silapetere, and Peter Hegemann. "Photocycle dynamics of the archaerhodopsin 3 based fluorescent voltage sensor QuasAr1". In: *International Journal of Molecular Sciences* 21.1 (2020). ISSN: 14220067. DOI: [10.3390/ijms21010160](https://doi.org/10.3390/ijms21010160).
- [20] Alfons Penzkofer, Arita Silapetere, and Peter Hegemann. "Photocycle dynamics of the Archaeerhodopsin 3 based fluorescent voltage sensor Archon2". In: *Journal of Photochemistry and Photobiology B: Biology* 225 (2021). ISSN: 18732682. DOI: [10.1016/j.jphotoobiol.2021.112331](https://doi.org/10.1016/j.jphotoobiol.2021.112331).
- [21] Alfons Penzkofer, Arita Silapetere, and Peter Hegemann. "Theoretical investigation of the photocycle dynamics of the Archaeerhodopsin 3 based fluorescent voltage sensor Archon2". In: *Journal of Photochemistry and Photobiology A: Chemistry* 437 (2023). ISSN: 10106030. DOI: [10.1016/j.jphotochem.2022.114366](https://doi.org/10.1016/j.jphotochem.2022.114366).
- [22] Willem J de Grip and Srividya Ganapathy. "Rhodopsins: An Excitingly Versatile Protein Species for Research, Development and Creative Engineering". In: *Frontiers in Chemistry* 10 (2022). ISSN: 2296-2646. DOI: [10.3389/fchem.2022.879609](https://doi.org/10.3389/fchem.2022.879609). URL: <https://www.frontiersin.org/articles/10.3389/fchem.2022.879609>.
- [23] Douglas Storace et al. "Toward Better Genetically Encoded Sensors of Membrane Potential". In: *Trends in Neurosciences* 39.5 (2016). ISSN: 1878108X. DOI: [10.1016/j.tins.2016.02.005](https://doi.org/10.1016/j.tins.2016.02.005).
- [24] Daniel R. Hochbaum et al. "All-optical electrophysiology in mammalian neurons using engineered microbial rhodopsins". In: *Nature Methods* 11.8 (2014). ISSN: 15487105. DOI: [10.1038/NMETH.3000](https://doi.org/10.1038/NMETH.3000).

- [25] Arita Silapetere et al. "QuasAr Odyssey: the origin of fluorescence and its voltage sensitivity in microbial rhodopsins". In: *Nature Communications* 13.1 (2022), p. 5501. ISSN: 2041-1723. DOI: [10.1038/s41467-022-33084-4](https://doi.org/10.1038/s41467-022-33084-4). URL: <https://doi.org/10.1038/s41467-022-33084-4>.
- [26] He Tian et al. "Video-based pooled screening yields improved far-red genetically encoded voltage indicators". In: *Nature Methods* (2023). ISSN: 1548-7105. DOI: [10.1038/s41592-022-01743-5](https://doi.org/10.1038/s41592-022-01743-5). URL: <https://doi.org/10.1038/s41592-022-01743-5>.
- [27] J. F. Nagle, L. A. Parodi, and R. H. Lozier. "Procedure for testing kinetic models of the photocycle of bacteriorhodopsin". In: *Biophysical Journal* 38.2 (1982). ISSN: 00063495. DOI: [10.1016/S0006-3495\(82\)84543-8](https://doi.org/10.1016/S0006-3495(82)84543-8).
- [28] J. F. Nagle. "Solving complex photocycle kinetics. Theory and direct method". In: *Biophysical Journal* 59.2 (1991). ISSN: 00063495. DOI: [10.1016/S0006-3495\(91\)82241-X](https://doi.org/10.1016/S0006-3495(91)82241-X).
- [29] Marco Locarno and Daan Brinks. "Analytical calculation of plasmonic resonances in metal nanoparticles: A simple guide". In: *American Journal of Physics* 91.7 (July 2023), p. 538. ISSN: 0002-9505. DOI: [10.1119/5.0094967](https://doi.org/10.1119/5.0094967). URL: <https://doi.org/10.1119/5.0094967>.
- [30] Chris D. Geddes and Joseph R. Lakowicz. "Metal-Enhanced Fluorescence". In: *Journal of Fluorescence*. Vol. 12. 2. 2002. DOI: [10.1023/A:1016875709579](https://doi.org/10.1023/A:1016875709579).
- [31] Anika Kinkhabwala et al. "Large single-molecule fluorescence enhancements produced by a bowtie nanoantenna". In: *Nature Photonics* 3.11 (2009). ISSN: 17494885. DOI: [10.1038/nphoton.2009.187](https://doi.org/10.1038/nphoton.2009.187).
- [32] Pascal Anger, Palash Bharadwaj, and Lukas Novotny. "Enhancement and quenching of single-molecule fluorescence". In: *Physical Review Letters* 96.11 (2006). ISSN: 00319007. DOI: [10.1103/PhysRevLett.96.113002](https://doi.org/10.1103/PhysRevLett.96.113002).
- [33] Sergei Kühn et al. "Enhancement of single-molecule fluorescence using a gold nanoparticle as an optical nanoantenna". In: *Physical Review Letters* 97.1 (2006). ISSN: 00319007. DOI: [10.1103/PhysRevLett.97.017402](https://doi.org/10.1103/PhysRevLett.97.017402).
- [34] Janina Kneipp et al. "In vivo molecular probing of cellular compartments with gold nanoparticles and nanoaggregates". In: *Nano Letters* 6.10 (2006). ISSN: 15306984. DOI: [10.1021/nl061517x](https://doi.org/10.1021/nl061517x).
- [35] Vincenzo Amendola et al. "Surface plasmon resonance in gold nanoparticles: A review". In: *Journal of Physics Condensed Matter* 29.20 (2017). ISSN: 1361648X. DOI: [10.1088/1361-648X/aa60f3](https://doi.org/10.1088/1361-648X/aa60f3).
- [36] Yirui Zhang et al. "From Genotype to Phenotype: Raman Spectroscopy and Machine Learning for Label-Free Single-Cell Analysis". In: *ACS Nano* 18.28 (2024), pp. 18101–18117. DOI: [10.1021/acsnano.4c04282](https://doi.org/10.1021/acsnano.4c04282). URL: <https://doi.org/10.1021/acsnano.4c04282>.
- [37] Alexander E. Krasnok et al. "An antenna model for the Purcell effect". In: *Scientific Reports* 5 (2015). ISSN: 20452322. DOI: [10.1038/srep12956](https://doi.org/10.1038/srep12956).

- [38] Yi Fu, Jian Zhang, and Joseph R. Lakowicz. “Plasmonic enhancement of single-molecule fluorescence near a silver nanoparticle”. In: *Journal of Fluorescence* 17.6 (2007). ISSN: 10530509. DOI: [10.1007/s10895-007-0259-0](https://doi.org/10.1007/s10895-007-0259-0).
- [39] Janina Kneipp, Harald Kneipp, and Katrin Kneipp. “SERS—a single-molecule and nanoscale tool for bioanalytics”. In: *Chemical Society Reviews* 37.5 (2008). ISSN: 14604744. DOI: [10.1039/b708459p](https://doi.org/10.1039/b708459p).
- [40] Jessica E. Donehue et al. “Plasmon-Enhanced brightness and photostability from single fluorescent proteins coupled to gold nanorods”. In: *Journal of Physical Chemistry C* 118.27 (2014). ISSN: 19327455. DOI: [10.1021/jp504186n](https://doi.org/10.1021/jp504186n).
- [41] Stephen A. Lee and Julie S. Biteen. “Interplay of Nanoparticle Resonance Frequency and Array Surface Coverage in Live-Cell Plasmon-Enhanced Single-Molecule Imaging”. In: *Journal of Physical Chemistry C* 122.10 (2018). ISSN: 19327455. DOI: [10.1021/acs.jpcc.8b01436](https://doi.org/10.1021/acs.jpcc.8b01436).
- [42] E. Prodan et al. “A Hybridization Model for the Plasmon Response of Complex Nanostructures”. In: *Science* 302.5644 (2003). ISSN: 00368075. DOI: [10.1126/science.1089171](https://doi.org/10.1126/science.1089171).
- [43] P. Nordlander et al. “Plasmon hybridization in nanoparticle dimers”. In: *Nano Letters* 4.5 (2004). ISSN: 15306984. DOI: [10.1021/nl049681c](https://doi.org/10.1021/nl049681c).
- [44] Hui Wang et al. “Plasmonic nanostructures: Artificial molecules”. In: *Accounts of Chemical Research* 40.1 (2007). ISSN: 00014842. DOI: [10.1021/ar0401045](https://doi.org/10.1021/ar0401045).
- [45] Brendan L. Darby et al. “Modified optical absorption of molecules on metallic nanoparticles at sub-monolayer coverage”. In: *Nature Photonics* 10.1 (2016). ISSN: 17494893. DOI: [10.1038/nphoton.2015.205](https://doi.org/10.1038/nphoton.2015.205).
- [46] Jiaqi Guo et al. “Diverse axial chiral assemblies of J-aggregates in plexcitonic nanoparticles”. In: *Nanoscale* 13.37 (2021). ISSN: 20403372. DOI: [10.1039/d1nr02634h](https://doi.org/10.1039/d1nr02634h).
- [47] Rohit Chikkaraddy et al. “Single-molecule strong coupling at room temperature in plasmonic nanocavities”. In: *Nature* 535.7610 (2016). ISSN: 14764687. DOI: [10.1038/nature17974](https://doi.org/10.1038/nature17974).
- [48] Lukas Novotny and Bert Hecht. “Optical antenna probes”. In: *Principles of Nano-Optics*. 2nd. 2009. Chap. 6.5, pp. 188–192. DOI: [10.1017/CBO9780511794193](https://doi.org/10.1017/CBO9780511794193).
- [49] Silvia Barbosa et al. “Tuning size and sensing properties in colloidal gold nanostars”. In: *Langmuir* 26.18 (2010). ISSN: 07437463. DOI: [10.1021/la102559e](https://doi.org/10.1021/la102559e).
- [50] Andrés Guerrero-Martínez et al. “Nanostars shine bright for you. Colloidal synthesis, properties and applications of branched metallic nanoparticles”. In: *Current Opinion in Colloid and Interface Science* 16.2 (2011). ISSN: 13590294. DOI: [10.1016/j.cocis.2010.12.007](https://doi.org/10.1016/j.cocis.2010.12.007).
- [51] Fritjof Helmchen and Winfried Denk. *Deep tissue two-photon microscopy*. 2005. DOI: [10.1038/nmeth818](https://doi.org/10.1038/nmeth818).
- [52] Richard K.P. Benninger and David W. Piston. “Two-photon excitation microscopy for the study of living cells and tissues”. In: *Current Protocols in Cell Biology* SUPPL.59 (2013). ISSN: 19342500. DOI: [10.1002/0471143030.cb0411s59](https://doi.org/10.1002/0471143030.cb0411s59).

- [53] F. Boitier et al. "Measuring photon bunching at ultrashort timescale by two-photon absorption in semiconductors". In: *Nature Physics* 5.4 (2009). ISSN: 17452481. DOI: [10.1038/nphys1218](https://doi.org/10.1038/nphys1218).
- [54] Norbert F. Scherer et al. "Fluorescence-detected wave packet interferometry: Time resolved molecular spectroscopy with sequences of femtosecond phase-locked pulses". In: *The Journal of Chemical Physics* 95.3 (1991). ISSN: 00219606. DOI: [10.1063/1.461064](https://doi.org/10.1063/1.461064).
- [55] Daan Brinks et al. "Ultrafast dynamics of single molecules". In: *Chemical Society Reviews* 43.8 (2014). ISSN: 14604744. DOI: [10.1039/c3cs60269a](https://doi.org/10.1039/c3cs60269a).
- [56] Robert R. Birge. "Two-Photon Spectroscopy of Protein-Bound Chromophores". In: *Accounts of Chemical Research* 19.5 (1986). ISSN: 15204898. DOI: [10.1021/ar00125a003](https://doi.org/10.1021/ar00125a003).
- [57] Christoph Schnedermann et al. "Vibronic Dynamics of the Ultrafast all-trans to 13-cis Photoisomerization of Retinal in Channelrhodopsin-1". In: *Journal of the American Chemical Society* 138.14 (2016). ISSN: 15205126. DOI: [10.1021/jacs.5b12251](https://doi.org/10.1021/jacs.5b12251).
- [58] Dougal MacLaurin et al. "Mechanism of voltage-sensitive fluorescence in a microbial rhodopsin". In: *Proceedings of the National Academy of Sciences of the United States of America* 110.15 (2013). ISSN: 00278424. DOI: [10.1073/pnas.1215595110](https://doi.org/10.1073/pnas.1215595110).
- [59] Valentyn I. Prokhorenko et al. "Coherent control of retinal isomerization in bacteriorhodopsin". In: *Science* 313.5791 (2006). ISSN: 00368075. DOI: [10.1126/science.1130747](https://doi.org/10.1126/science.1130747).
- [60] Kristina Meyer et al. "Noisy optical pulses enhance the temporal resolution of pump-probe spectroscopy". In: *Physical Review Letters* 108.9 (2012). ISSN: 00319007. DOI: [10.1103/PhysRevLett.108.098302](https://doi.org/10.1103/PhysRevLett.108.098302).
- [61] Teruhisa Hirai and Sriram Subramaniam. "Protein Conformational Changes in the Bacteriorhodopsin Photocycle: Comparison of Findings from Electron and X-Ray Crystallographic Analyses". In: *PLoS ONE* 4.6 (2009). ISSN: 19326203. DOI: [10.1371/journal.pone.0005769](https://doi.org/10.1371/journal.pone.0005769).
- [62] K. C. Hasson, Feng Gai, and Philip A. Anfinrud. "The photoisomerization of retinal in bacteriorhodopsin: Experimental evidence for a three-state model". In: *Proceedings of the National Academy of Sciences of the United States of America* 93.26 (1996). ISSN: 00278424. DOI: [10.1073/pnas.93.26.15124](https://doi.org/10.1073/pnas.93.26.15124).
- [63] Kazumasa Oda et al. "Time-resolved serial femtosecond crystallography reveals early structural changes in channelrhodopsin". In: *eLife* 10 (2021). ISSN: 2050084X. DOI: [10.7554/eLife.62389](https://doi.org/10.7554/eLife.62389).

2

ANALYTICAL CALCULATION OF PLASMONIC RESONANCES IN METAL NANOPARTICLES: A SIMPLE GUIDE

In this chapter, we develop a comprehensive analytical framework to describe plasmonic resonances in metal nanoparticles. By combining classical electromagnetism with the Drude model and an extended Clausius–Mossotti relation, we derive a unified model that links material properties, size and shape to the resonant behavior of nanoparticles. This approach provides intuitive guidelines for tuning the resonance by adjusting environmental parameters and geometric factors.

This analytical model forms the theoretical backbone of our strategy to manipulate protein function by physical means. By establishing how plasmonic resonances can be precisely controlled, we set the stage for creating the ideal near-field conditions that can modulate the function of fluorescent proteins.

This chapter has been published as: Marco Locarno, Daan Brinks. "Analytical calculation of plasmonic resonances in metal nanoparticles: A simple guide". *American Journal of Physics* (2023).
DOI: 10.1119/5.0094967

2.1. INTRODUCTION

Advances in nanotechnology and photonics go hand in hand, from super-resolution microscopy helping us visualize life at the nanoscale,¹ to extreme-UV lithography enabling the creation of nanoscale chips needed to analyze it.² At the intersection of photonics and nanotechnology lies the topic of plasmonics.³ Plasmonics involves the creation, study and manipulation of signals embedded in optical-frequency oscillations of surface electrons along metal-dielectric interfaces. Plasmonics confines optical-frequency signals to subwavelength-size volumes, thereby providing the interface between optical electromagnetic fields and nanoscopic devices and circuitry.

When an electromagnetic field interacts with a metal nanoparticle, it will lead to charge oscillations in the metal. These collective oscillations, known as plasmons, are excited when the frequency of the electromagnetic field matches the resonant frequency of the metal nanoparticle. The electrons are free to move within the boundaries of the particle but are ultimately confined to its surface. For these reasons, the effect is called Localized Surface Plasmon (LSP). Given that the oscillation is at the same frequency as the incoming field, the effect is interchangeably called plasmonic resonance.

Designing metal nanoparticles to answer questions in nanophysics, nanochemistry and nanobiology requires understanding the plasmonic resonance. Due to quantum mechanical effects, the properties of nanoscale objects often cannot be explained intuitively. Fortunately, the most prominent plasmonic effects can be explained within a classical framework. We will begin with a historical perspective. Then, to model the plasmonic resonance in metal nanoparticles, we will need a framework to describe three distinct features: the metallic character, the size (the "nano"), and the shape of the particle. We will introduce the Drude model, a reasonable description of electrons in metals. The Quasi-Static Approximation will then let us take into account the nanoscale size of the particles. Additionally, the generalization of the Clausius-Mossotti relation will let us consider a particle embedded in a dielectric medium and the effect of its shape. By combining these aspects, we are able to build a classical model for the plasmonic resonance in metal nanoparticles. We will then deal with some of the limitations of the Quasi-Static Approximation by introducing final corrections to the model, to extend its validity as far as possible. As our assumptions are all based on classical electromagnetism, the final model will be classical too.

2.2. BRIEF HISTORY OF PLASMONICS

While nanotechnology emerged as a field only a few decades ago, peculiar optical phenomena due to nanoparticles have intrigued humankind since ancient times. Witnessing and harnessing such "technologies" far preceded any possible scientific explanation: photonic crystals shape light, thus creating spectacular iridescent colors in butterflies,⁴ lead-based quantum dots have been involved in black hair dyes manufactured by ancient Greeks and Romans,⁵ and copper nanoparticles were employed in red opaque glass production in Egypt and Mesopotamia.⁶

One of the most impressive pieces of glasswork incorporating metal nanoparticles is the Lycurgus cup (Figs. 2.1.a and 2.1.b). Dated around the 4th century, this Roman cage cup is made up of dichroic glass, so that an observer sees it red if light passes through it,

but green if light is reflected to them. Recent analysis showed that the dichroism is due to the presence of colloidal gold and silver nanoparticles dispersed throughout the glass. The embedded particles have diameters around 70 nm, meaning that they are invisible to optical microscopy and require transmission electron microscopy (TEM) to be seen.⁷

2



Figure 2.1: (Color online) The Lycurgus cup changes color depending whether the light is a) reflected or b) transmitted.* c) Faraday's colloidal gold in a glass flask.[†]

Michael Faraday is credited with performing the first scientific experiments on the optical properties of nanoparticles, focusing on gold colloids in the 1850s. He was puzzled by the ruby red color of the solutions he synthesized (Fig. 2.1.c), far removed from the aureate color of bulk gold. A satisfying classical explanation of this phenomenon came only in 1904, when Maxwell Garnett combined the new Drude theory of metals with Lord Rayleigh's description of electromagnetic properties of small spheres.⁸ Then, in 1908 Gustav Mie developed the exact solution for light scattering by small spherical particles,⁹ accurately predicting size-dependent plasmonic resonances. Shortly after, in 1912, Richard Gans successfully extended the description of optical phenomena to oblate and prolate spheroids.¹⁰ However, these theories were all purely based on the optical properties of bulk metals, and it was not until 1970 that they were modified by Uwe Kreibig and Peter Zacharias to take their nanoscale size into account.¹¹ For the first time, they explained the electronic and optical response of silver and gold nanoparticles in terms of localized surface plasmon excitations. It became clear then that size, shape, arrangement, medium and temperature all have a crucial role in controlling the intensity and frequency of plasmonic resonances.

From the early 2000's on, the interest in plasmonics boomed, thanks to novel nanofabrication techniques, commercialization of simulation software and the plethora of biological and biomedical applications.^{12,13} To summarize fifty years of research and more than a century of theoretical modeling, we start by examining the object under study, the metal nanoparticle, and its defining features.

2.3. CLASSICAL DERIVATION OF PLASMONIC RESONANCE

2.3.1. DRUDE MODEL FOR METALS

The electric properties of materials are characterized by the dielectric constant ϵ , which relates the electric displacement \vec{D} to the electric field \vec{E} through the equation $\vec{D} = \epsilon_0 \vec{E} + \vec{P} = \epsilon_0 \epsilon \vec{E}$. When the applied field is sinusoidal, the dielectric constant is a complex number; the imaginary part represents the out-of-phase response of the material. Within the Drude model, the complex dielectric function of a metal is given by:

$$\epsilon_m(\omega) = 1 - \frac{\omega_p^2}{\omega^2 + \gamma^2} - i \frac{\omega_p^2 \gamma}{\omega^3 + \gamma^2 \omega}. \quad (2.1)$$

Two derivations of this well-known formula can be found in the Supplementary Material[#]. Here $\omega_p = \sqrt{\frac{Ne^2}{\epsilon_0 m}}$ is the plasma frequency and γ is the damping frequency, both dependent on the metal considered. The plasma frequency depends on the carrier density, N , the electron charge, e , and the effective mass of the electron, m . The damping frequency γ is given by Matthiessen's rule for different independent collision events, each possessing a time constant τ_j :

$$\gamma = \sum_j 1/\tau_j. \quad (2.2)$$

This equation provides the statistical rate at which the electron motion in the bulk material is disrupted due to collisions between electrons and nuclei, defects, impurities, or other electrons. Furthermore, an extension to the Drude model has been formulated to account for the positive background of ions in the constant term $\epsilon_{m,\infty}$, referred to as the core polarization:^{3,14}

$$\epsilon_m(\omega) = \epsilon_{m,\infty} - \frac{\omega_p^2}{\omega^2 + \gamma^2} - i \frac{\omega_p^2 \gamma}{\omega^3 + \gamma^2 \omega}. \quad (2.3)$$

In Table 2.1 we report the Drude parameters for common plasmonic metals, fitted from experimental data. **CRC2005** Note that the experimental and fitted data do not match completely, as the Drude model is an approximation of the actual complex dielectric function, which can include interband and intraband transitions. Throughout the paper, we will take gold as a typical metal for plasmonics.

	$\epsilon_{m,\infty}$	ω_p [rad/s]	γ [rad/s]
Au	7.926	$1.23 \cdot 10^{16}$	$3.8 \cdot 10^{13}$
Ag	5.303	$1.42 \cdot 10^{16}$	$1.0 \cdot 10^{14}$
Cu	6.087	$1.34 \cdot 10^{16}$	$1.5 \cdot 10^{14}$
Al	1	$1.93 \cdot 10^{16}$	$2.4 \cdot 10^{14}$

Table 2.1: Drude parameters for common (bulk) metals.

With these concepts in hand we can provide a simple yet rigorous derivation of plasmonic resonance in metal nanoparticles.

2.3.2. QUASI-STATIC APPROXIMATION

If a nanoparticle is much smaller than the wavelength (Fig. 2.2), then all the electrons inside the nanoparticle feel the same electric field and oscillate in phase. This approach is called the Quasi-Static Approximation. Let d be the size of the nanoparticle, λ the wavelength, \vec{k} the wave vector and ω the angular frequency of the incoming field \vec{E}^0 , \vec{r} the relative position of an arbitrary point with respect to the center of the nanoparticle, and t the time. If $d \ll \lambda$, then $\vec{k} \cdot \vec{r} \approx 0$ and mathematically we obtain:

$$\vec{E}^0(\vec{r}, t) = \vec{E}^0 e^{i(\omega t - \vec{k} \cdot \vec{r})} \approx \vec{E}^0 e^{i\omega t}. \quad (2.4)$$

Because of this, the polarization is uniform, and the effect of the Quasi-Static Approximation on the total dipole moment of the nanoparticle \vec{p}_{np} is very conveniently translated to:

$$\vec{p}_{np} = V \vec{P}, \quad (2.5)$$

where V is the volume of the nanoparticle and \vec{P} the polarization density. The Quasi-Static Approximation lets us drop the dependence on the position \vec{r} .

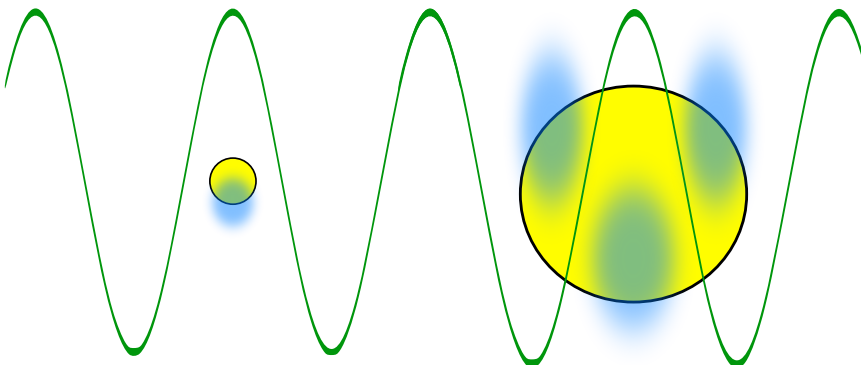


Figure 2.2: Dipolar (left) and multipolar (right) excitation of the free electrons in metal nanoparticles. The electron clouds are represented as light blue halos, while the metal cores as solid yellow.

The careful reader might point out that the wavelength inside the nanoparticle may not be the same as the one in the dielectric medium. The concept of wavelength itself may even be ill-defined if the field decays exponentially inside the metal. A relevant comparison would then be between the size of the nanoparticle and the skin depth δ of the metal. For common metals like gold, silver, copper and aluminum, the skin depth at optical frequencies is in the order of a few tens of nanometers. If $d \lesssim \delta$, then the field can penetrate the nanoparticle completely and the uniformity of the polarization can still be assumed. Refer to the Supplementary Material[#] for more details regarding skin depth.

It is important to note that particles larger than the wavelength produce a plethora of effects that cannot be explained as the simple radiation of a dipole, due to the occurrence of multipolar effects. Eventually, extremely large particles will exhibit the optical properties of bulk metal.

2.3.3. GENERALIZATION OF THE CLAUSIUS-MOSSOTTI RELATION FOR ELLOPSOIDS

Let us now consider an isolated ellipsoid having a complex dielectric function ϵ_m and semiaxes respectively a_x , a_y and a_z , immersed in a dielectric material (from this point on referred to as the "host") having a real and positive dielectric constant ϵ_h (Fig. 2.3.a).

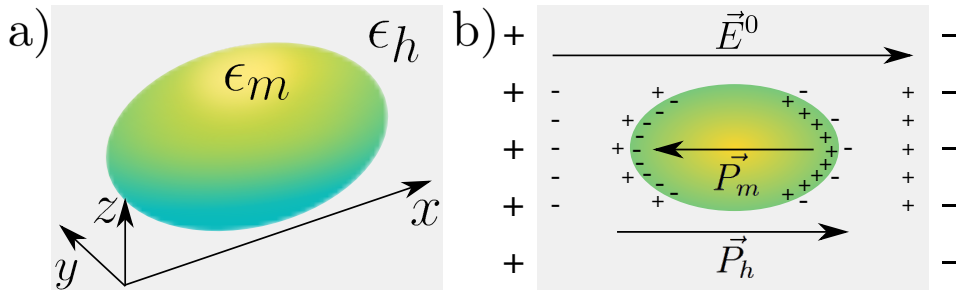


Figure 2.3: a) Ellipsoidal particle immersed in a dielectric medium with the chosen reference system. b) Snapshot of the incoming electric field and the induced polarization contributions of the metal and the host. This depiction is realistic only in the optical regime and under the Quasi-Static Approximation (QSA), for which the rearrangement of charge is collective and instantaneous.

The nanoparticle's dipole moment \vec{p}_{np} is a function of its polarizability tensor $\vec{\alpha}$ as well as of the local electric field \vec{E}_{loc} . The latter is different from the applied field \vec{E}^0 because of the polarization of the host, but if the dielectric medium is linear, homogeneous and isotropic, then the local field will be proportional to the applied field ($\vec{E}_{loc} = \epsilon_h \vec{E}^0$), and so:

$$\vec{p}_{np} = \epsilon_0 \vec{\alpha} \vec{E}_{loc} = \epsilon_0 \epsilon_h \vec{\alpha} \vec{E}^0. \quad (2.6)$$

To calculate the polarizability, we therefore need to find the relation between the dipole moment and the electric field.

First, we notice that the local electric field is the superposition of the applied field and the opposing field produced by the displacement of charges. Although it is a well-known fact that, in the static limit, the electric field in a conductor is zero, we have to consider that under the QSA the order of magnitude of the skin depth is comparable with the size of the nanoparticle. In this case, the local electric field \vec{E}_{loc} , defined at the boundary of the nanoparticle, creates a polarization in the metal \vec{P}_m ; hence electric charges appear at its surface (Fig. 2.3.b). As a consequence, the host dielectric also polarizes near the surface (\vec{P}_h). We can treat the boundary as an effective medium, encompassing both the charges in the metal and in the host. The effective polarization \vec{P} can be deduced from the difference between the two opposing polarizations. \vec{P} is in the opposite direction from that of the applied field, thus generating a restoring force. The local electric field, for every j -th axis ($j = x, y, z$), is then:^{15,16}

$$E_{loc,j} = E_j^0 - L_j \frac{P_j}{\epsilon_0 \epsilon_h}, \quad (2.7)$$

where L_j is the depolarization factor which accounts for the shape of the particle itself:

$$L_j = \frac{a_x a_y a_z}{2} \int_0^\infty \frac{dq}{(q + a_j^2) \sqrt{\prod_{\eta=x,y,z} (q + a_\eta^2)}}. \quad (2.8)$$

The depolarization factors arise from the solution of Laplace's equation in ellipsoidal coordinates. A full derivation can be found in Ref. [15].

The effective polarization \vec{P} is the difference of the polarizations of the metal \vec{P}_m and of the host \vec{P}_h .¹⁶

$$P_j = P_{m,j} - P_{h,j} = \epsilon_0 \epsilon_m E_{loc,j} - \epsilon_0 \epsilon_h E_{loc,j} = \epsilon_0 (\epsilon_m - \epsilon_h) E_{loc,j}. \quad (2.9)$$

Combining Eqs. (2.7) and (2.9), we write:

$$P_j = \epsilon_0 (\epsilon_m - \epsilon_h) \left(E_j^0 - L_j \frac{P_j}{\epsilon_0 \epsilon_h} \right). \quad (2.10)$$

Solving for P_j :

$$P_j = \frac{\epsilon_0 \epsilon_h (\epsilon_m - \epsilon_h)}{\epsilon_h + L_j (\epsilon_m - \epsilon_h)} E_j^0. \quad (2.11)$$

Then introducing the Quasi-Static Approximation in Eq. (2.5) we get:

$$p_{np,j} = \epsilon_0 \epsilon_h V \underbrace{\frac{\epsilon_m - \epsilon_h}{\epsilon_h + L_j (\epsilon_m - \epsilon_h)}}_{\alpha_j} E_j^0. \quad (2.12)$$

Finally, making the volume of the ellipsoid explicit, we obtain the polarizability:

$$\alpha_j = \frac{4\pi a_x a_y a_z}{3} \frac{\epsilon_m - \epsilon_h}{\epsilon_h + L_j (\epsilon_m - \epsilon_h)}. \quad (2.13)$$

It is important to note that $\vec{\alpha}$ is a diagonal matrix. In other words, if the incoming field is aligned with one of the axes of the ellipsoid, the polarization will be parallel to it. This considerably simplifies the calculations.

Normally, we would have to calculate the integral in Eq. (2.8), given an arbitrary set of semiaxes lengths. Such calculation is not trivial. Fortunately, an important property of the depolarization factors can drastically simplify the results for simple geometries. The sum of the three depolarization factors is:

$$\sum_{j=x,y,z} L_j = 1. \quad (2.14)$$

A simple, novel proof of this property can be found in the Supplementary Material[#].

Thanks to this normalization property, some easy geometries (see Table 2.2) can be treated without calculating the integrals explicitly. Anisotropy is then reflected by the matrix nature of $\vec{\alpha}$, eventually leading \vec{p}_{np} to not be parallel to \vec{E}^0 .

The Clausius-Mossotti relation, used to describe the polarizability of spherical particles in a vacuum:

$$\alpha_j = 3\nu \frac{\epsilon_m - 1}{\epsilon_m + 2}, \quad j = x, y, z, \quad (2.15)$$

in which ν is the volume of the spherical particle, coincides with Eq. (2.13) for $a_x = a_y = a_z$, and $\epsilon_h = 1$. For this reason, Eq. (2.13) is the generalization of the Clausius-Mossotti relation.

Particle Shape	Semiaxes	Depolarization factors
Sphere	$a_x = a_y = a_z$	$L_x = L_y = L_z = 1/3$
Long cylinder	$a_x \gg a_y, a_z$	$L_x = 0, L_y = L_z = 1/2$
Large disk	$a_x = a_y \gg a_z$	$L_x = L_y = 0, L_z = 1$

Table 2.2: Depolarization factors for some typical shapes.

2.3.4. PLASMONIC RESONANCE

We now have all the tools to calculate the plasmonic resonance. But what does it mean for a nanoparticle to have a plasmonic resonance? Why do we talk about a plasmonic peak? The simplest way to picture such an effect is by directly plugging the result of the Drude model (Eq. (2.3)) in the calculation of the polarizability (Eq. (2.13)). For a sphere with gold-like Drude parameters, put either in vacuum or water, we get the typical wavelength dependence of the polarizability shown in Fig. 2.4.

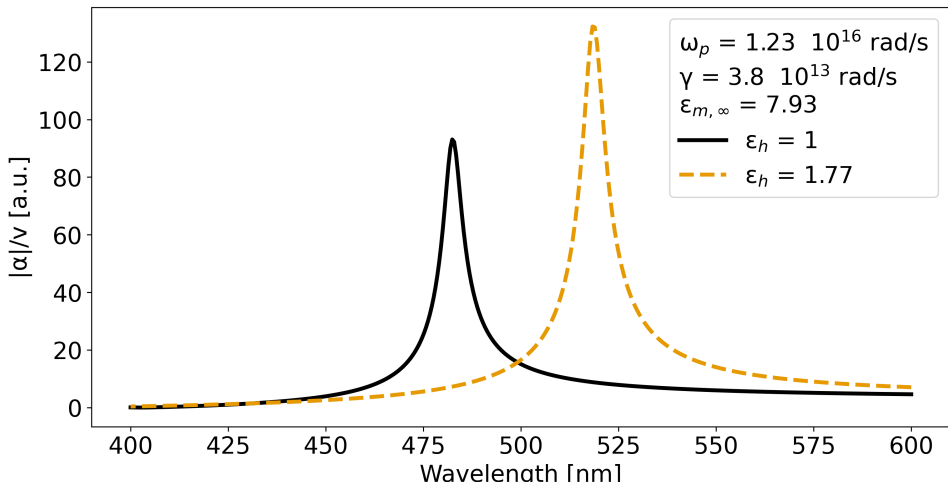


Figure 2.4: The volume polarizability of a nanosphere with gold-like parameters, calculated from Eqs. (2.3) and (2.13), immersed either in vacuum ($\epsilon_h = 1$) or in water ($\epsilon_h = 1.77$), exhibits a peak in wavelengths. ‡

The functional form for $|\alpha|$ is a sharp peak. At the angular frequency where the polarizability is maximal, the electrons oscillate with a higher amplitude. Given such a sharp feature in the frequency, we refer to the peak position as the resonance frequency.

To calculate the plasmonic resonance frequency, one can maximize $|\alpha|$. From Eq. (2.13), it is easy to see that if the denominator approaches zero, the polarizability intensity drastically increases, leading to a strong dipole moment at frequency ω_{res} . This resonance condition translates to the requirement that, in a given direction:

$$\operatorname{Re}[\epsilon_m(\omega_{res})] = -\frac{1-L_j}{L_j}\epsilon_h, \quad \operatorname{Im}[\epsilon_m(\omega_{res})] \approx 0. \quad (2.16)$$

We see that the resonance frequency depends on the geometrical features of the nanoparticle and on the dielectric medium in which it is immersed. The generalized formula for the resonance frequency ω_{res} for an arbitrary metal nanoparticle can be obtained by combining Eq. (2.16) with the result of the Drude model (Eq. (2.3)):

$$\omega_{res} = \sqrt{\frac{\omega_p^2}{\epsilon_{m,\infty} + \frac{1-L_j}{L_j}\epsilon_h} - \gamma^2} \approx \frac{\omega_p}{\sqrt{\epsilon_{m,\infty} + \frac{1-L_j}{L_j}\epsilon_h}}, \quad (2.17)$$

where the reasonable assumption of $\omega_p \gg \gamma$ has been introduced (refer to Table 2.1 for the realistic orders of magnitude). The shift due to changes in ϵ_h enables a multitude of sensing applications. In the host dielectric environment, variations due to chemical, physical or biological activity result in fact in shifts in plasmonic peaks.^{17,18,19}

In the case of a sphere ($L_j = 1/3, \forall j$) the above equations reduce to the Fröhlich condition:

$$\operatorname{Re}[\epsilon_m(\omega_{res})] = -2\epsilon_h, \quad \operatorname{Im}[\epsilon_m(\omega_{res})] \approx 0, \quad \omega_{res} \approx \frac{\omega_p}{\sqrt{\epsilon_{m,\infty} + 2\epsilon_h}}. \quad (2.18)$$

As expected, Eq. (2.18) predicts the correct positions²⁰ for the resonance peak for a nanosphere with gold-like Drude parameters: when in vacuum $\omega_{res} \approx 3.9 \cdot 10^{15}$ rad/s ($\lambda_{res} \approx 480$ nm), while when in water $\omega_{res} \approx 3.6 \cdot 10^{15}$ rad/s ($\lambda_{res} \approx 520$ nm). This surprisingly simple result is already sufficient to explain the color of Faraday's colloidal gold (Fig. 2.1.c). As the solution contains gold nanospheres, the resonance frequency ω_{res} will be in the cyan-green part of the spectrum, so it appears ruby red when illuminated by white light.

Unfortunately, only a few materials satisfy Eq. (2.18) in the optical range. For the resonance to exist, the imaginary part of the dielectric function must be sufficiently low. For this reason, the most significant plasmonic materials are also the most conductive: silver, gold, copper and aluminum. Other less commonly used metals are palladium, platinum and nickel.²¹ An invaluable contribution to the investigation of plasmonic candidates was given by Eadon and Creighton, in their review of the ultraviolet/visible spectrum of 52 different metal nanospheres, in vacuum and in water.²² Nowadays, the search for novel plasmonic candidates focuses on metallic alloys, (doped) semiconductors and metamaterials.²³

Measurable effects due to the plasmonic resonance include absorption and scattering, which are quantifiable by their cross sections. In the dipolar regime ($d \ll \lambda$), the Rayleigh formula for cross sections can be applied:¹⁵

$$\sigma_{abs} = -k\operatorname{Im}[\alpha], \quad \sigma_{sca} = \frac{k^4}{6\pi}|\alpha|^2, \quad (2.19)$$

where k is the wave number. It is important to note the cross sections' dependence on α and, as a consequence, on the volume: since the absorption cross section σ_{abs} scales linearly with V while the scattering one σ_{sca} scales quadratically with it, it is reasonable to assume that smaller particles mainly absorb light while larger particles mainly scatter it.

2

However, the most prominent effect of plasmonic resonances is that of field enhancement. Outside the particle, the total field is a superposition of the incoming field \vec{E}^0 and of the dipolar field generated by the particle itself. For a continuous wave, the local field outside the nanoparticle takes the shape of a classical dipole field:²⁴

$$\vec{E}(\vec{r}) = \vec{E}^0 + \frac{1}{4\pi\epsilon_0\epsilon_h} \frac{3(\vec{r} \cdot \vec{p}_{np})\vec{r} - r^2\vec{p}_{np}}{r^5}, \quad (2.20)$$

where r is the distance from the center of the particle. As can be intuited, resonances in α will reflect on \vec{p}_{np} and subsequently on $\vec{E}(\vec{r})$. Field enhancement is typically quantified by $|E|^2/|E^0|^2$ (as in Fig. 2.5). This factor can make the local electric field tens or hundreds of times higher than the incoming field. The shape of the particle can be engineered to create radiation enhancements that are wavelength-, polarization- and direction-dependent, just like in classical antennas.^{25,26}

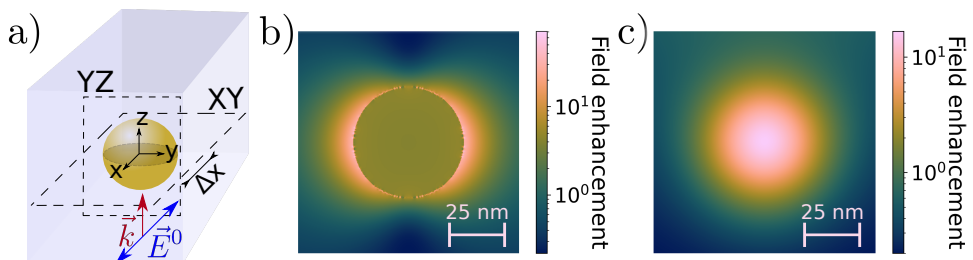


Figure 2.5: Finite-Difference Time-Domain (FDTD) simulation of the field enhancement at $\lambda = 540$ nm near a spherical gold nanoparticle of radius 25 nm in water. a) Sketch of the simulated object, b) field enhancement in the XY plane [$z = 0$] and c) field enhancement in the YZ plane [$\Delta x = 4$ nm away from the surface of the nanoparticle]. §

One interesting effect can be noted in Fig. 2.5: along the direction orthogonal to the oscillation, the radiated field causes destructive interference with the incoming field, leading to areas where the field is quenched ($|E|^2/|E^0|^2 < 1$) instead of enhanced. This is possible because, in Eq. (2.20), for some \vec{r} and at a certain frequency, $\vec{r} \cdot \vec{p}_{np} = 0$ and $|1 - \frac{\alpha}{4\pi r^3}|^2 < 1$.

The Finite-Difference Time-Domain simulations in Fig. 2.5 solve Maxwell's equations in discretized space and time, characterizing each portion of space with the complex dielectric function ϵ and complex magnetic permeability μ . These simulations introduce minimal approximations and accurately compute the electromagnetic fields, presenting a case very close to reality. Using this simulation, the plasmonic resonance occurs at 540 nm, instead of 520 nm, as shown previously in Fig. 2.4. This shift is mainly an effect of radiation damping,²⁷ which shows that the Quasi-Static Approximation does not always provide accurate answers. This is why we need to look beyond it.

2.4. BEYOND THE QUASI-STATIC APPROXIMATION

The Quasi-Static Approximation describes nanoscale processes fairly well, such as the absorption of certain colors or the local field enhancement in the proximity of metal nanoparticles. However, it fails to predict other effects related to particle size: in the Quasi-Static Approximation, particle size is irrelevant, as long as it is smaller than the incoming wavelength. Can we extend this theory to include the particle's size and shape?

The first correction we will introduce takes into account the collisions of the electrons with the nanoparticle boundaries, which have implicitly been neglected until now. Then, the second correction will take us closer to the multipolar regime by involving retardation effects. Considering the classical nature of this extended model, it is impressive how well it fits experiments for such nanoscopic objects, as we will see.

2.4.1. SURFACE DAMPING

Up to now, we have implicitly considered the damping frequency γ to be dominated by the collisions of electrons with other electrons, lattice nuclei or phonons. At a very small scale, however, electrons will also impact the particle boundary. This is notably the case when the dimensions of the particle are smaller than the mean free path, that is the average distance traveled by the electron between two consecutive collisions. In other words, if the particle is small enough, the electrons will impact the boundary much more often than they collide with other objects.¹⁵ The empirical model developed hereafter aims at taking this effect into account, and well matches experimental data. In the end, it is very similar to the exact one obtained via semiclassical calculations.^{28,29}

As the free electrons move at the Fermi velocity v_F , the characteristic time between two consecutive collisions with the boundary will be:

$$\tau_{\text{boundary}} = \frac{\lambda_{\text{boundary}}}{v_F}, \quad (2.21)$$

where $\lambda_{\text{boundary}}$ is the characteristic length of the process. By applying Matthiessen's rule (Eq. (2.2)), the damping frequency will become:

$$\gamma = \gamma_{\text{bulk}} + \frac{1}{\tau_{\text{boundary}}} = \frac{v_F}{\lambda_{\text{MFP}}} + \frac{v_F}{\lambda_{\text{boundary}}}, \quad (2.22)$$

where γ_{bulk} is the bulk metal damping frequency and λ_{MFP} the mean free path.

For a sphere of radius r , Kreibig¹¹ used the linear relation $\lambda_{\text{boundary}} = \frac{4}{3}r$, but coefficients between 1 and 4 have been used by other authors.^{30,31,32,33,34} A simple and intuitive motivation for a coefficient of $\frac{4}{3}$ is provided hereafter, based solely on geometrical considerations.

Consider a spherical nanoparticle of radius r inside which electrons can travel only in straight trajectories. Let $O(x, y, z)$ be the initial point on the surface where an electron has just collided with the boundary, and let $O'(x', y', z')$ be a generic final point on the sphere surface where the electron will impact after traveling a distance $d[O, O']$. Then:

$$x^2 + y^2 + z^2 = r^2, \quad x'^2 + y'^2 + z'^2 = r^2. \quad (2.23)$$

Since the scattering is assumed to be isotropic inside the sphere, all the points O' belonging to the surface have the same probability of being hit.

Without loss of generality, consider a reference system such that the initial point is $O(0, 0, r)$.

$$d[O, O'] = \sqrt{x'^2 + y'^2 + (z' - r)^2} = \sqrt{2}r\sqrt{1 - \frac{z'}{r}}. \quad (2.24)$$

2

The characteristic length of the process $\lambda_{boundary}$ can be defined as the average distance $d[O, O']$:

$$\lambda_{boundary} = \frac{\int_0^{2\pi} \int_{-r}^r d[O, O'] dz' d\theta}{\int_0^{2\pi} \int_{-r}^r dz' d\theta} = \frac{\sqrt{2} \int_{-r}^r \sqrt{1 - \frac{z'}{r}} dz'}{2}. \quad (2.25)$$

By changing the integration variable:

$$a = 1 - \frac{z'}{r} \Rightarrow dz' = -rda, \quad (2.26)$$

the integral can be rewritten and solved as follows:

$$\lambda_{boundary} = \frac{\sqrt{2}r}{2} \int_0^2 \sqrt{a} da = \frac{4}{3}r. \quad (2.27)$$

Now let us examine the consequences of surface damping. Around the plasma frequency, it is almost always true that $\omega \gg \gamma$ (refer to Table 2.1 for the realistic orders of magnitude), so in first approximation, the Drude model in Eq. (2.3) becomes:

$$\epsilon_1 \approx \epsilon_{m,\infty} - \frac{\omega_p^2}{\omega^2}, \quad \epsilon_2 \approx \frac{\omega_p^2 \gamma}{\omega^3}. \quad (2.28)$$

While the real part is almost unchanged when introducing the damping correction, near the resonance frequency (as defined by the Fröhlich condition in Eq. (2.18)) the imaginary part can be rewritten as:

$$\epsilon_2 \approx \frac{\omega_p^2}{\omega_{res}^3} \left(\gamma_{bulk} + \frac{3\nu_F}{4r} \right) = \epsilon_{2,bulk} + A \frac{\nu_F}{r}, \quad (2.29)$$

where we have employed the Kreibig relation for spherical nanoparticles, and $A = \frac{3}{4} \frac{\omega_p^2}{\omega_{res}^3}$. For very small particles this implies that, at ω_{res} , the condition of small ϵ_2 is not true anymore, therefore drastically diminishing the resonance peak in α . A calculated example for a nanoparticle with gold-like parameters in water is provided in Fig. 2.6.a for various particle sizes.

2.4.2. MODIFIED LONG-WAVELENGTH APPROXIMATION

The dipolar approximation is valid as long as the dimensions of the metal nanoparticle are such that $d \ll \lambda$. Otherwise, variations in the incoming field will not be negligible and multipolar modes will eventually be excited. Between this dipolar treatment and the brute-force computational solution of Maxwell's equations lies the so-called Modified Long-Wavelength Approximation (MLWA), a correction to the polarizability obtained in the Quasi-Static Approximation (QSA) that includes retardation effects.¹⁷

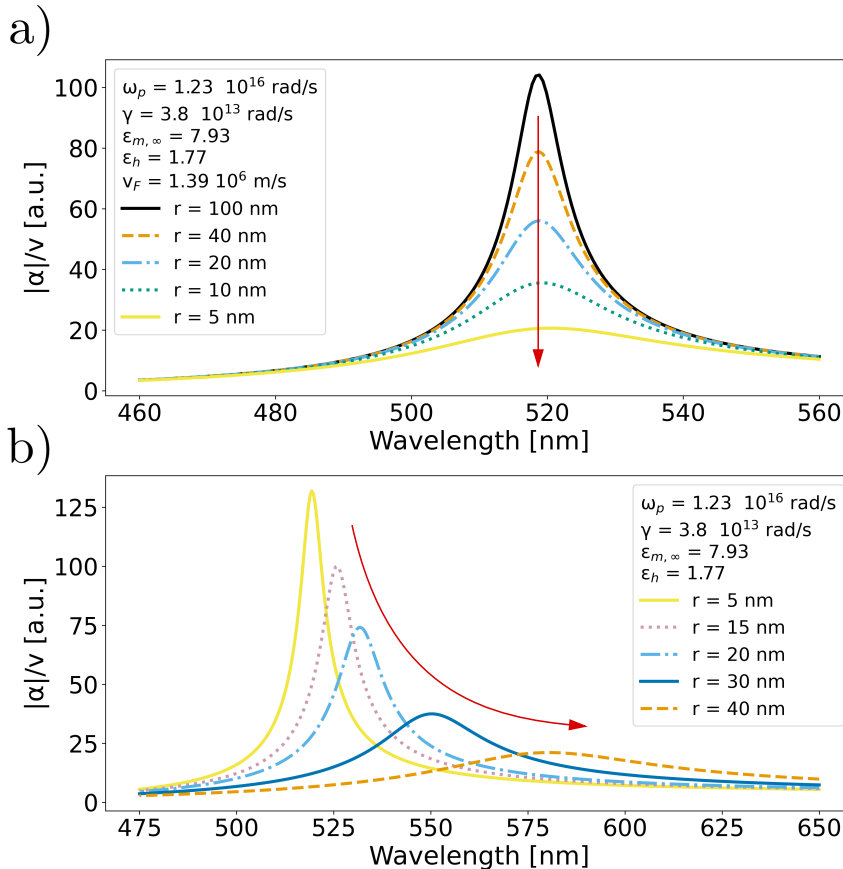


Figure 2.6: Corrections to the Quasi-Static Approximation: a) Surface damping effect calculated from Eq. (2.29), b) Modified Long-Wavelength Approximation (MLWA) calculated from Eq. (2.38). The red arrows indicate the effects of either correction on peak positions and intensities, as a function of decreasing, respectively increasing, particle radius. ‡

The MLWA treats each atom in the nanoparticle as a dipole emitter and takes into account that its electric field propagates at the speed of light c (and not instantly), causing a retarded dipolar field. While in the QSA we imposed $\vec{k} \cdot \vec{r} = 0$ (Eq. (2.4)), in the following derivation of the MLWA equations, the dipole radiation is expanded in a Taylor series up to the third order (kr)³. The infinitesimal electric field is integrated over the volume of the particle, and finally a corrected polarizability α_{MLWA} is defined.

Using the complex notation, an oscillating dipole moment p can be expressed as:

$$p = p_0 e^{i\omega t} e^{-ikr}, \quad \dot{p} = i\omega p, \quad \ddot{p} = -\omega^2 p. \quad (2.30)$$

For a point emitter, the radial and tangential fields in spherical coordinates are.³⁵

$$E_R = \frac{2 \cos \theta}{4\pi\epsilon_0\epsilon_h} \left(\frac{p}{r^3} + \frac{\dot{p}}{cr^2} \right), \quad E_\theta = \frac{\sin \theta}{4\pi\epsilon_0\epsilon_h} \left(\frac{p}{r^3} + \frac{\dot{p}}{cr^2} + \frac{\ddot{p}}{c^2 r} \right). \quad (2.31)$$

Since the component of the electric field orthogonal to the applied field cancels out on integration over the nanosphere (as shown in the Supplementary Material[#]), we only need to quantify the parallel one. For a point emitter:

$$2 \quad E_{II} = E_R \cos \theta - E_\theta \sin \theta = \frac{p_0 e^{i\omega t} e^{-ikr}}{4\pi\epsilon_0\epsilon_h} \left[2\cos^2 \theta \left(\frac{1}{r^3} + \frac{i\omega}{cr^2} \right) - \sin^2 \theta \left(\frac{1}{r^3} + \frac{i\omega}{cr^2} - \frac{\omega^2}{c^2 r} \right) \right]. \quad (2.32)$$

Expanding e^{-ikr} to the third order, rewriting $\sin^2 \theta = 1 - \cos^2 \theta$ and making $\omega = kc$ explicit:

$$E_{II} = \frac{p_0 e^{i\omega t}}{4\pi\epsilon_0\epsilon_h} \left[\cos^2 \theta \left(\frac{3}{r^3} + \frac{k^2}{2r} \right) - \left(\frac{1}{r^3} - \frac{k^2}{2r} + \frac{i2k^3}{3} \right) \right] \\ = \frac{p_0 e^{i\omega t}}{4\pi\epsilon_0\epsilon_h} \left[\frac{1}{r^3} (3\cos^2 \theta - 1) + \frac{k^2}{2r} (\cos^2 \theta + 1) - \frac{i2k^3}{3} \right]. \quad (2.33)$$

As an extension of the QSA, we can treat the nanoparticle as a single emitter with a radiated field E_{MLWA} being the superposition of all the dipole fields with respect to its center. A convenient reference system takes $\vec{r} \rightarrow -\vec{r}$ ($r \rightarrow r, \theta \rightarrow -\theta, \phi \rightarrow \phi$), meaning that every vector starts from a point emitter in the sphere and points to its center. This coordinates change does not influence the signs in the equation because of the symmetry in θ . Therefore, for every volume element $dV = r^2 \sin \theta dr d\theta d\phi$ inside the sphere we will have a radiated field:

$$dE_{MLWA} = \frac{1}{4\pi\epsilon_0\epsilon_h} \left[\frac{1}{r^3} (3\cos^2 \theta - 1) + \frac{k^2}{2r} (\cos^2 \theta + 1) - \frac{i2k^3}{3} \right] dp \\ = \frac{1}{4\pi\epsilon_0\epsilon_h} \left[\frac{1}{r^3} (3\cos^2 \theta - 1) + \frac{k^2}{2r} (\cos^2 \theta + 1) - \frac{i2k^3}{3} \right] Pr^2 \sin \theta dr d\theta d\phi. \quad (2.34)$$

We finally integrate dE_{MLWA} over the volume of the sphere of radius R and factor the volume out to obtain the total MLWA correction:

$$E_{MLWA} = \frac{1}{4\pi\epsilon_0\epsilon_h} \frac{4\pi}{3} \left(k^2 R^2 - i \frac{2}{3} k^3 R^3 \right) P = \frac{1}{4\pi\epsilon_0\epsilon_h} \left(\frac{k^2}{R} - i \frac{2}{3} k^3 \right) p_{np}. \quad (2.35)$$

This formula can be generalized for ellipsoidal nanoparticles of semiaxes $a_j, j = x, y, z$:¹⁷

$$E_{MLWA,j} = \frac{1}{4\pi\epsilon_0\epsilon_h} \left(\frac{k^2}{a_j} - i \frac{2}{3} k^3 \right) p_{np,j}. \quad (2.36)$$

At this point we only need to rewrite \vec{p}_{np} :

$$\vec{p}_{np} = \epsilon_0 \epsilon_h \overleftrightarrow{\alpha} (\vec{E}^0 + \vec{E}_{MLWA}) = \epsilon_0 \epsilon_h \overleftrightarrow{\alpha}_{MLWA} \vec{E}^0, \quad (2.37)$$

from which:

$$\alpha_{MLWA,j} = \frac{\alpha_j}{1 - \frac{\alpha_j}{4\pi} \left(\frac{k^2}{a_j} - i \frac{2}{3} k^3 \right)}. \quad (2.38)$$

For sufficiently small nanoparticles we retrieve the QSA ($\alpha_{MLWA,j} \approx \alpha_j$), as expected. For relatively small yet finite volumes, the imaginary term proportional to k^3 can be neglected ($\alpha_{MLWA,j} \approx \frac{4\pi\alpha_j}{4\pi-\alpha_j k^2/a_j}$). For larger volumes, the imaginary term dominates the denominator.

The term $\alpha_j \frac{k^2}{a_j}$ in Eq. (2.38) is called dynamic depolarization because it is obtained in a dynamic calculation ($k > 0$), and its coefficient is real, corresponding to a change in the effective particle depolarization factor. Let us recall that α_j is proportional to particle volume ($\alpha_j \propto a_x a_y a_z$). As $\frac{a_x a_y a_z}{a_j} k^2$ increases, a more negative value of ϵ_1 is necessary to meet the resonance condition. At small but finite particle volumes, this effect enhances the plasmonic resonance; at larger volumes, it is responsible for the shift of the resonance peak.

The term $-i\alpha_j \frac{2}{3} k^3$ in Eq. (2.38) is called radiative damping because it arises from the spontaneous emission of radiation by the induced dipole. The term grows rapidly with particle volume. Being imaginary, it contributes heavily to ϵ_2 and therefore to the resonance damping. For relatively large particle volumes, it accounts for the damping by radiative losses and results in a broadening and a strong decrease of the plasmonic resonance (also counterbalancing the enhancement due to dynamic depolarization just mentioned).

According to this approximation, an increase in particle size (a_j) will result in a red-shifted, broadened and less intense plasmonic resonance. This is indeed what we notice in Fig. 2.6.b in the calculated peaks for a nanoparticle with gold-like parameters immersed in water. The MLWA usually works well for nanoparticles of dimensions up to ≈ 200 nm,³⁶ above which multipolar resonances cannot be neglected, and computational methods are required.

The complete analytical model combines the corrected Drude model, the generalized Clausius-Mossotti formula for polarizability, the surface damping effect and the MLWA. In Fig. 2.7, an example for a gold elongated ellipsoid having $a_x/a_y = a_x/a_z = 2$ is presented against a gold sphere of $r = 25$ nm, of the same volume. The cross sections are calculated in the dipolar limit using Eq. (2.19). The agreement between the Finite-Difference Time-Domain (FDTD) simulation and the model is remarkable, both in the peak positions and the ratio of cross section components. Experimental evidence also corroborates this result.³⁷

2.5. FINAL REMARKS

Starting from a general model for metals and from the polarization of a particle immersed in a dielectric host, we explored the effects of several features on the final resonance peak induced by an external oscillating electric field.

The analytical approach took us far into the understanding of the plasmonic resonance. However, as already hinted at the end of Section IV, the corrections to the Quasi-Static Approximation have their own limitations. In fact, neglecting key features in the shape of the particle like spikes, neat edges, flat sides or amorphous protrusions will result in incorrect predictions. But where the analytical approach fails, numerical simulations can be used. The most common numerical techniques include generalized Mie theory, Finite-Difference Time-Domain (FDTD), Discrete Dipole Approximation (DDA),

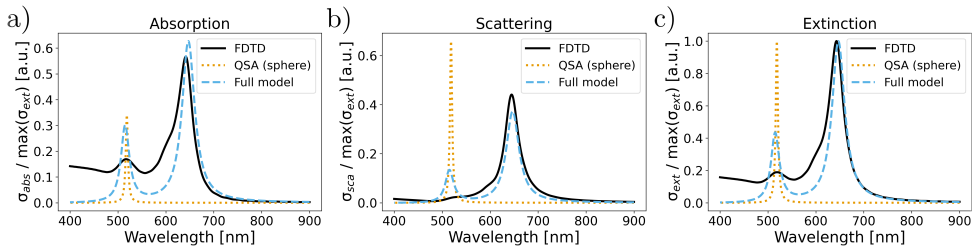


Figure 2.7: a) Absorption, b) scattering and c) extinction cross sections for a gold ellipsoid immersed in water, having an aspect ratio $a_x/a_y = a_x/a_z = 2$ and a volume $v = \frac{4}{3}\pi(25 \text{ nm})^3 = 6.54 \cdot 10^4 \text{ nm}^3$. Comparison between a FDTD simulation, the Quasi-Static Approximation of a gold-like sphere of the same volume, and the full analytical model for an ellipsoid. To account for both the longitudinal and transverse modes, cross sections have been calculated separately and averaged. The cross sections are each normalized to their own maximum extinction cross section, respectively. ‡

Finite-Element Method (FEM) and Boundary Element Method (BEM).^{38,39} Each simulation technique has its own advantages and drawbacks.

Should this material be used as didactic reference, the authors strongly suggest the incorporation of at least some examples of applications from state-of-the-art research. These examples should be tailored depending on the interest of the course, and can be directed towards optics, biophysics or condensed matter physics. To learn more about light-matter interaction or expand knowledge about state-of-the-art plasmonics and emerging applications, the authors recommend Fox's⁴⁰ and Maier's³ books, which provide valuable insights of the field and are very accessible for lecturers and students alike.

The properties of plasmonic resonances depend on material shape and intrinsic properties. The analytical approach supplied here is limited to ellipsoidal geometries, but already takes into account virtually all relevant material properties (in a classical approximation). However, while only simulations will provide reliable descriptions of the plasmonic effects in realistic nanoparticles, the outlined fundamental approach, no matter its flaws, provides an understanding of why and how plasmonic resonances emerge in nanoparticles, and thus gives an intuitive basis and plausibility check for numerical design.

BIBLIOGRAPHY

- [1] Bo Huang, Mark Bates, and Xiaowei Zhuang. "Super-resolution fluorescence microscopy". In: *Annual Review of Biochemistry* 78 (2009). ISSN: 00664154. DOI: [10.1146/annurev.biochem.77.061906.092014](https://doi.org/10.1146/annurev.biochem.77.061906.092014).
- [2] Banqiu Wu and Ajay Kumar. "Extreme ultraviolet lithography: A review". In: *Journal of Vacuum Science & Technology B: Microelectronics and Nanometer Structures* 25.6 (2007). ISSN: 10711023. DOI: [10.1116/1.2794048](https://doi.org/10.1116/1.2794048).
- [3] Stefan A. Maier. *Plasmonics: Fundamentals and applications*. 1st. Springer, 2007. DOI: [10.1007/0-387-37825-1](https://doi.org/10.1007/0-387-37825-1).
- [4] Robert W. Corkery and Eric C. Tyrode. "On the colour of wing scales in butterflies: Iridescence and preferred orientation of single gyroid photonic crystals". In: *Interface Focus* 7.4 (2017). ISSN: 20428901. DOI: [10.1098/rsfs.2016.0154](https://doi.org/10.1098/rsfs.2016.0154).
- [5] Philippe Walter et al. "Early use of PbS nanotechnology for an ancient hair dyeing formula". In: *Nano Letters* 6.10 (2006). ISSN: 15306984. DOI: [10.1021/nl061493u](https://doi.org/10.1021/nl061493u).
- [6] Robert H. Brill and Nicholas D. Cahill. "A Red Opaque Glass from Sardis and Some Thoughts on Red Opaque in General". In: *Journal of Glass Studies* 30 (1988). DOI: [10.1364/AO.46.003811](https://doi.org/10.1364/AO.46.003811).
- [7] David J. Barber and Ian C. Freestone. "An investigation of the origin of the colour of the Lycurgus cup by analytical Transmission Electron Microscopy". In: *Archaeometry* 32.1 (1990). ISSN: 14754754. DOI: [10.1111/j.1475-4754.1990.tb01079.x](https://doi.org/10.1111/j.1475-4754.1990.tb01079.x).
- [8] Mark L. Brongersma. "Introductory lecture: Nanoplasmonics". In: *Faraday Discussions* 178 (2015). ISSN: 13645498. DOI: [10.1039/c5fd90020d](https://doi.org/10.1039/c5fd90020d).
- [9] Gustav Mie. "Beiträge zur Optik trüber Medien, speziell kolloidaler Metallösungen". In: *Annalen der Physik* 330.3 (1908). ISSN: 15213889. DOI: [10.1002/andp.19083300302](https://doi.org/10.1002/andp.19083300302).
- [10] Richard Gans. "Über die Form ultramikroskopischer Goldteilchen". In: *Annalen der Physik* 342.5 (1912). ISSN: 15213889. DOI: [10.1002/andp.19123420503](https://doi.org/10.1002/andp.19123420503).
- [11] Uwe Kreibig. "Electronic properties of small silver particles: The optical constants and their temperature dependence". In: *Journal of Physics F: Metal Physics* 4.7 (1974). ISSN: 03054608. DOI: [10.1088/0305-4608/4/7/007](https://doi.org/10.1088/0305-4608/4/7/007).
- [12] Vincenzo Amendola et al. "Surface plasmon resonance in gold nanoparticles: A review". In: *Journal of Physics Condensed Matter* 29.20 (2017). ISSN: 1361648X. DOI: [10.1088/1361-648X/aa60f3](https://doi.org/10.1088/1361-648X/aa60f3).
- [13] Andrés Guerrero-Martínez et al. "Nanostars shine bright for you. Colloidal synthesis, properties and applications of branched metallic nanoparticles". In: *Current Opinion in Colloid and Interface Science* 16.2 (2011). ISSN: 13590294. DOI: [10.1016/j.cocis.2010.12.007](https://doi.org/10.1016/j.cocis.2010.12.007).

- 2
- [14] Suk Joo Youn et al. "Extended Drude model analysis of noble metals". In: *Physica Status Solidi (B) Basic Research*. Vol. 244. 4. 2007. DOI: [10.1002/pssb.200642097](https://doi.org/10.1002/pssb.200642097).
 - [15] Craig F. Bohren and Donald R. Huffman. *Absorption and Scattering of Light by Small Particles*. John Wiley & Sons, 1998. ISBN: 9783527618156. DOI: [10.1002/9783527618156](https://doi.org/10.1002/9783527618156).
 - [16] William L. Barnes. "Particle plasmons: Why shape matters". In: *American Journal of Physics* 84.8 (2016). ISSN: 0002-9505. DOI: [10.1119/1.4948402](https://doi.org/10.1119/1.4948402).
 - [17] Lance K. Kelly et al. "The optical properties of metal nanoparticles: The influence of size, shape, and dielectric environment". In: *Journal of Physical Chemistry B* 107.3 (2003). ISSN: 10895647. DOI: [10.1021/jp026731y](https://doi.org/10.1021/jp026731y).
 - [18] Ming Li, Scott K. Cushing, and Nianqiang Wu. "Plasmon-enhanced optical sensors: A review". In: *Analyst* 140.2 (2015). ISSN: 13645528. DOI: [10.1039/c4an01079e](https://doi.org/10.1039/c4an01079e).
 - [19] Marek Piliarik et al. "Local refractive index sensitivity of plasmonic nanoparticles". In: *Optics Express* 19.10 (2011). ISSN: 10944087. DOI: [10.1364/oe.19.009213](https://doi.org/10.1364/oe.19.009213).
 - [20] Stephan Link and Mostafa A. El-Sayed. "Spectral Properties and Relaxation Dynamics of Surface Plasmon Electronic Oscillations in Gold and Silver Nanodots and Nanorods". In: *Journal of Physical Chemistry B* 103.40 (1999). ISSN: 15206106. DOI: [10.1021/jp9917648](https://doi.org/10.1021/jp9917648).
 - [21] Paul R. West et al. "Searching for better plasmonic materials". In: *Laser and Photonics Reviews* 4.6 (2010). ISSN: 18638880. DOI: [10.1002/lpor.200900055](https://doi.org/10.1002/lpor.200900055).
 - [22] J. Alan Creighton and Desmond G. Eadon. "Ultraviolet-visible absorption spectra of the colloidal metallic elements". In: *Journal of the Chemical Society, Faraday Transactions* 87.24 (1991). ISSN: 09565000. DOI: [10.1039/FT9918703881](https://doi.org/10.1039/FT9918703881).
 - [23] Alexandra Boltasseva and Harry A. Atwater. "Low-loss plasmonic metamaterials". In: *Science* 331.6015 (2011). ISSN: 00368075. DOI: [10.1126/science.1198258](https://doi.org/10.1126/science.1198258).
 - [24] David J. Griffiths. *Introduction to Electrodynamics*. Cambridge University Press, 2017. DOI: [10.1017/9781108333511](https://doi.org/10.1017/9781108333511).
 - [25] Alberto G. Curto et al. "Unidirectional emission of a quantum dot coupled to a nanoantenna". In: *Science* 329.5994 (2010). ISSN: 00368075. DOI: [10.1126/science.1191922](https://doi.org/10.1126/science.1191922).
 - [26] Marta Castro-Lopez, Daan Brinks, and Niek F. van Hulst. "Non-Reciprocal Optical Antennas". In: *arXiv* (Dec. 2014). DOI: <https://doi.org/10.48550/arXiv.1412.4797>. URL: <https://arxiv.org/abs/1412.4797>.
 - [27] Benjamin M. Ross, Savas Tasoglu, and Luke P. Lee. "Plasmon resonance differences between the near- and far-field and implications for molecular detection". In: *Plasmonics: Metallic Nanostructures and Their Optical Properties VII*. Vol. 7394. 2009. DOI: [10.1117/12.826804](https://doi.org/10.1117/12.826804).
 - [28] Niels Asger Mortensen et al. "A generalized non-local optical response theory for plasmonic nanostructures". In: *Nature Communications* 5 (2014). ISSN: 20411723. DOI: [10.1038/ncomms4809](https://doi.org/10.1038/ncomms4809).

- [29] Somayeh Karimi et al. "Surface Plasmon Resonance in Small Gold Nanoparticles: Introducing a Size-Dependent Plasma Frequency for Nanoparticles in Quantum Regime". In: *Plasmonics* 14.4 (2019). ISSN: 15571963. DOI: [10.1007/s11468-018-0866-4](https://doi.org/10.1007/s11468-018-0866-4).
- [30] Asef Kheirandish, Nasser Sepehri Javan, and Hosein Mohammadzadeh. "Modified Drude model for small gold nanoparticles surface plasmon resonance based on the role of classical confinement". In: *Scientific Reports* 10.1 (2020). ISSN: 20452322. DOI: [10.1038/s41598-020-63066-9](https://doi.org/10.1038/s41598-020-63066-9).
- [31] Cecilia Noguez. "Surface plasmons on metal nanoparticles: The influence of shape and physical environment". In: *Journal of Physical Chemistry C* 111.10 (2007). ISSN: 19327447. DOI: [10.1021/jp066539m](https://doi.org/10.1021/jp066539m).
- [32] Kin Hung Fung and Che Ting Chan. "A computational study of the optical response of strongly coupled metal nanoparticle chains". In: *Optics Communications* 281.4 (2008). ISSN: 00304018. DOI: [10.1016/j.optcom.2007.10.019](https://doi.org/10.1016/j.optcom.2007.10.019).
- [33] Eduardo A. Coronado and George C. Schatz. "Surface plasmon broadening for arbitrary shape nanoparticles: A geometrical probability approach". In: *Journal of Chemical Physics* 119.7 (2003). ISSN: 00219606. DOI: [10.1063/1.1587686](https://doi.org/10.1063/1.1587686).
- [34] Stéphane Berciaud et al. "Observation of intrinsic size effects in the optical response of individual gold nanoparticles". In: *Nano Letters* 5.3 (2005). ISSN: 15306984. DOI: [10.1021/nl050062t](https://doi.org/10.1021/nl050062t).
- [35] Max Born and Emil Wolf. *Principles of Optics: 60th Anniversary Edition*. 7th. Cambridge University Press, 2019. ISBN: 9781108769914. DOI: [10.1017/9781108769914](https://doi.org/10.1017/9781108769914).
- [36] Ellen J. Zeman and George C. Schatz. "An accurate electromagnetic theory study of surface enhancement factors for Ag, Au, Cu, Li, Na, Al, Ga, In, Zn, and Cd". In: *Journal of Physical Chemistry* 91.3 (1987). ISSN: 00223654. DOI: [10.1021/j100287a028](https://doi.org/10.1021/j100287a028).
- [37] Ming Zhang Wei et al. "Seed-Mediated Synthesis of Gold Nanorods at Low Concentrations of CTAB". In: *ACS Omega* 6.13 (2021). ISSN: 24701343. DOI: [10.1021/acsomega.1c00510](https://doi.org/10.1021/acsomega.1c00510).
- [38] James Parsons et al. "A comparison of techniques used to simulate the scattering of electromagnetic radiation by metallic nanostructures". In: *Journal of Modern Optics* 57.5 (2010). ISSN: 09500340. DOI: [10.1080/09500341003628702](https://doi.org/10.1080/09500341003628702).
- [39] Manuel R. Gonçalves. "Plasmonic nanoparticles: Fabrication, simulation and experiments". In: *Journal of Physics D: Applied Physics* 47.21 (2014). ISSN: 13616463. DOI: [10.1088/0022-3727/47/21/213001](https://doi.org/10.1088/0022-3727/47/21/213001).
- [40] Mark Fox. *Optical Properties of Solids*. 2nd. Oxford University Press, 2010. ISBN: 9780199573370.
- [41] Bang Wong. "Points of view: Color blindness". In: *Nature Methods* 8.6 (2011). ISSN: 1548-7091. DOI: [10.1038/nmeth.1618](https://doi.org/10.1038/nmeth.1618).
- [42] Fabio Cramer, Grace E. Shephard, and Philip J. Heron. "The misuse of colour in science communication". In: *Nature Communications* 11.1 (2020). ISSN: 20411723. DOI: [10.1038/s41467-020-19160-7](https://doi.org/10.1038/s41467-020-19160-7).

* Credits: © The Trustees of the British Museum.

† Credits: © Paul Wilkinson.

‡ Plot colors have been selected according to the color-vision deficiency friendly color cycle proposed by Okabe and Ito and made popular by Wong.⁴¹

§ The code for simulation in Lumerical's FDTD Solutions can be found in the Supporting Information and on GitHub (<https://github.com/Brinkslab/LSP>). The results were plotted in Spyder, using the color-vision deficiency friendly and perceptually uniform color map 'batlow'.⁴²

Supplementary Material is available at <https://www.scitation.org/doi/suppl/10.1119/5.0094967>.

3

FINITE-DIFFERENCE TIME-DOMAIN PLASMONIC SIMULATIONS

The previous chapter primarily focused on spheres and ellipsoids, using analytical treatments to explore their plasmonic properties. However, with recent advancements in nanochemistry and nanofabrication, the possibilities for nanoparticle shapes have become virtually limitless. Structures with spikes, sharp edges and amorphous protrusions exhibit unique features that cannot be accurately predicted by analytical models based on previous cases. To obtain precise and reliable results, numerical methods that effectively solve Maxwell's equations become essential. Among these methods, the Finite-Difference Time-Domain (FDTD) technique stands out for its robust capabilities and minimal reliance on approximations.

This chapter employs FDTD simulations to predict plasmonic responses in nanoparticles with nontrivial geometries. By comparing nanospheres, nanorods and spiky nanostars, the simulations illustrate how variations in shape and orientation significantly affect local electromagnetic field enhancements. The numerical results provide practical insights into the behavior of nanoparticles under realistic conditions.

The insights gained from these simulations are essential for guiding the design of plasmonic structures that interact optimally with fluorescent protein. In particular, understanding the spatial distribution and intensity of the enhanced fields enables us to select nanoparticle designs that would best facilitate the modulation of the protein photocycle. This simulation-based refinement bridges our theoretical models with the experimental applications detailed in the next chapter.

3.1. ON THE METHOD

The invention of the FDTD method is credited to Kane S. Yee, who articulated his findings in a 1966 paper.¹ Yee's approach tackled the approximate solution of Maxwell's equations through the discretization of both space and time, along with the employment of central difference approximations for the curl equations. Yee's method introduced a groundbreaking advancement by achieving second-order accuracy in the obtained results. However, for nearly a decade, this technique remained purely theoretical due to the absence of sufficiently powerful computers capable of executing three-dimensional calculations. Only in the late 1970s did computers with adequate computational capabilities become available, enabling the practical application of FDTD in numerical simulations.

3.1.1. MAXWELL'S EQUATIONS IN MATTER

Undoubtedly, the cornerstone of classical electromagnetism in macroscopic materials lies in the four Maxwell's equations, which comprehensively depict the behaviour of electric and magnetic fields within matter:²

$$\vec{\nabla} \cdot \vec{D} = \rho_f \quad (3.1)$$

where \vec{D} represents the electric displacement, and ρ_f denotes the free charge density;

$$\vec{\nabla} \cdot \vec{B} = 0 \quad (3.2)$$

where \vec{B} is the magnetic field;

$$\vec{\nabla} \times \vec{E} = -\frac{\partial \vec{B}}{\partial t} \quad (3.3)$$

where \vec{E} represents the electric field, and $\frac{\partial \vec{B}}{\partial t}$ represents the rate of change of the magnetic field \vec{B} with respect to time;

$$\vec{\nabla} \times \vec{H} = \vec{J}_f + \frac{\partial \vec{D}}{\partial t} \quad (3.4)$$

where \vec{H} represents the magnetic field intensity, \vec{J}_f denotes the free current density, and $\frac{\partial \vec{D}}{\partial t}$ represents the rate of change of the electric displacement field \vec{D} with respect to time.

Equations (3.1) and (3.2) are the divergence equations, while Eqs. (3.3) and (3.4) are the curl equations. To these, we must add the constitutive relations that describe the material:

$$\vec{D} = \epsilon_0 \epsilon \vec{E} \quad (3.5)$$

where ϵ_0 is the vacuum permittivity, and ϵ denotes the complex dielectric function.

$$\vec{H} = \frac{1}{\mu_0 \mu} \vec{B} \quad (3.6)$$

where μ_0 is the vacuum permeability and μ denotes the relative permeability.

In the absence of free charges and free currents:

$$\rho_f = 0, \quad \vec{J}_f = 0 \quad (3.7)$$

Combining all the previous equations together, the curl equations simplify to:

$$\vec{\nabla} \times \vec{E} = -\mu_0 \mu \frac{\partial \vec{H}}{\partial t} \quad (3.8)$$

$$\vec{\nabla} \times \vec{H} = \epsilon_0 \epsilon \frac{\partial \vec{E}}{\partial t} \quad (3.9)$$

3

Once the equations are discretized, they can be solved iteratively to obtain the values of \vec{E} and \vec{H} . It is often useful to examine the projections of these equations onto the three main cartesian axes:

$$\mu_0 \mu \frac{\partial H_x}{\partial t} = \frac{\partial E_y}{\partial z} - \frac{\partial E_z}{\partial y} \quad (3.10)$$

$$\mu_0 \mu \frac{\partial H_y}{\partial t} = \frac{\partial E_z}{\partial x} - \frac{\partial E_x}{\partial z} \quad (3.11)$$

$$\mu_0 \mu \frac{\partial H_z}{\partial t} = \frac{\partial E_x}{\partial y} - \frac{\partial E_y}{\partial x} \quad (3.12)$$

$$\epsilon_0 \epsilon \frac{\partial E_x}{\partial t} = \frac{\partial H_z}{\partial y} - \frac{\partial H_y}{\partial z} \quad (3.13)$$

$$\epsilon_0 \epsilon \frac{\partial E_y}{\partial t} = \frac{\partial H_x}{\partial z} - \frac{\partial H_z}{\partial x} \quad (3.14)$$

$$\epsilon_0 \epsilon \frac{\partial E_z}{\partial t} = \frac{\partial H_y}{\partial x} - \frac{\partial H_x}{\partial y} \quad (3.15)$$

3.1.2. CENTRAL DIFFERENCE APPROXIMATION

For a function f that is continuously differentiable to all orders (C^∞ -continuous), the Taylor series expansions around the points $x + \Delta x/2$ and $x - \Delta x/2$, where Δx is arbitrarily small, can be expressed as:

$$f\left(x + \frac{\Delta x}{2}\right) = f(x) + \frac{\partial f}{\partial x} \frac{\Delta x}{2} + \frac{1}{2} \frac{\partial^2 f}{\partial x^2} \left(\frac{\Delta x}{2}\right)^2 + \frac{1}{3!} \frac{\partial^3 f}{\partial x^3} \left(\frac{\Delta x}{2}\right)^3 + \dots \quad (3.16)$$

$$f\left(x - \frac{\Delta x}{2}\right) = f(x) - \frac{\partial f}{\partial x} \frac{\Delta x}{2} + \frac{1}{2} \frac{\partial^2 f}{\partial x^2} \left(\frac{\Delta x}{2}\right)^2 - \frac{1}{3!} \frac{\partial^3 f}{\partial x^3} \left(\frac{\Delta x}{2}\right)^3 + \dots \quad (3.17)$$

Then:

$$\frac{f(x + \frac{\Delta x}{2}) - f(x - \frac{\Delta x}{2})}{\Delta x} = \frac{\partial f}{\partial x} + \frac{\Delta x^2}{24} \frac{\partial^3 f}{\partial x^3} + \dots \quad (3.18)$$

Rearranging the terms:

$$\frac{\partial f}{\partial x} \approx \frac{f(x + \frac{\Delta x}{2}) - f(x - \frac{\Delta x}{2})}{\Delta x} + O(\Delta x^2) \quad (3.19)$$

As the value of Δx decreases, the leading order error decreases quadratically, resulting in an approximation that exhibits second-order accuracy. Therefore, a smaller value of Δx leads to improved precision in this approximation.

3.1.3. DISCRETIZATION OF MAXWELL'S EQUATIONS

Let us consider a three-dimensional uniform rectangular grid where each cell, known as a Yee cell, has dimensions $\Delta x, \Delta y, \Delta z$ along each cartesian axis. Time is also discretized in steps of duration Δt . The coordinates of a node in the grid at a specific time (x, y, z, t) can be expressed in terms of $(i\Delta x, j\Delta y, k\Delta z, n\Delta t)$, where i, j, k, n are integers.

3

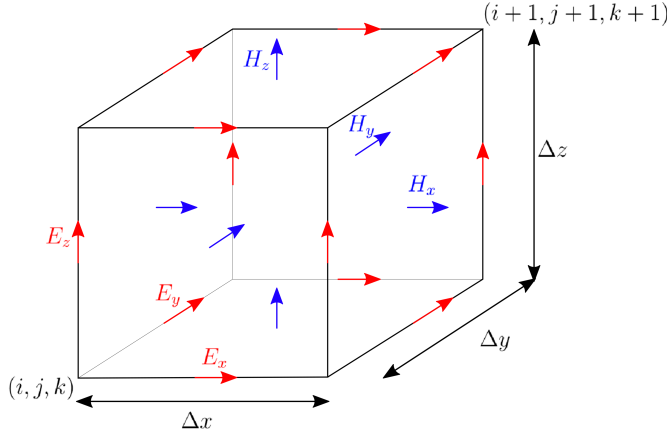


Figure 3.1: Definition of a Yee cell. Electric components are indicated by red arrows, while magnetic intensity components by blue arrows.

A more concise notation to represent any arbitrary function in the discretized space is:

$$f(x, y, z, t) = f(i\Delta x, j\Delta y, k\Delta z, n\Delta t) = f_{i,j,k}^n \quad (3.20)$$

To maintain consistency with central difference approximations, the most suitable way to sample the projections of the fields is as follows: for a Yee cell, the electric fields \vec{E} are sampled at the center of grid edges, while the magnetic fields \vec{H} are sampled at the center of grid faces.

Their discrete forms can be derived by applying Eq. (3.19) to the partial derivatives in the curl equations. For instance, Eqs. (3.10) and (3.13) become:

$$\mu_0 \mu \left(\frac{H_x^{n+1}_{i,j+\frac{1}{2},k+\frac{1}{2}} - H_x^n_{i,j+\frac{1}{2},k+\frac{1}{2}}}{\Delta t} \right) = \frac{E_y^{n+\frac{1}{2}}_{i,j+\frac{1}{2},k+1} - E_y^{n+\frac{1}{2}}_{i,j+\frac{1}{2},k}}{\Delta z} - \frac{E_z^{n+\frac{1}{2}}_{i,j+1,k+\frac{1}{2}} - E_z^{n+\frac{1}{2}}_{i,j,k+\frac{1}{2}}}{\Delta y} \quad (3.21)$$

$$\epsilon_0 \epsilon \left(\frac{E_x^{n+\frac{1}{2}}_{i+\frac{1}{2},j,k} - E_x^{n-\frac{1}{2}}_{i+\frac{1}{2},j,k}}{\Delta t} \right) = \frac{H_z^n_{i+\frac{1}{2},j+\frac{1}{2},k} - H_z^n_{i+\frac{1}{2},j-\frac{1}{2},k}}{\Delta y} - \frac{H_y^n_{i+\frac{1}{2},j,k+\frac{1}{2}} - H_y^n_{i+\frac{1}{2},j,k-\frac{1}{2}}}{\Delta z} \quad (3.22)$$

These discretized equations can be rearranged to calculate the fields at subsequent time steps explicitly. This approach is known as the leapfrog method of solving Maxwell's equations, where \vec{E} and \vec{H} are not known simultaneously or at the same position. The progression is as follows:

$$\vec{E}^{-\frac{1}{2}} \rightarrow \vec{H}^0 \rightarrow \vec{E}^{\frac{1}{2}} \rightarrow \vec{H}^1 \rightarrow \vec{E}^{\frac{3}{2}} \rightarrow \vec{H}^2 \rightarrow \dots \quad (3.23)$$

The initial conditions are typically set to zero, except for the sources, which are regions where the fields are forced to assume specific values in both time and space. It is true in principle that a finer mesh (i.e., smaller $\Delta x, \Delta y, \Delta z$) yields higher precision. However, interfaces that are not properly meshed can introduce unphysical artefacts. The time step is automatically chosen to minimize the error and is calculated as:

$$\Delta t = \frac{1}{c_{\max}} \frac{CFLN}{\sqrt{\frac{1}{\Delta x^2} + \frac{1}{\Delta y^2} + \frac{1}{\Delta z^2}}} \quad (3.24)$$

Here, c_{\max} represents the maximum wave speed in the problem domain, and $CFLN$ denotes the Courant-Friedrichs-Lowy number. To ensure the stability of the algorithm, $CFLN$ must be less than 1, so it is typically chosen to be close to 1 (e.g., $CFLN = 0.99$).

All complex dielectric functions have been fitted on experimental data in Ref. [CRC2005].

3.2. SPHERICAL GOLD NANOPARTICLES

Numerical simulations of gold nanospheres were conducted using the script for Lumerical's FDTD Solutions, which is publicly accessible in the GitHub repository.³

The code performs simulations by varying the radius R of a sphere submerged in water. It identifies the maximum field enhancement $|E|^2/|E^0|^2$, averaged within a small volume ($\Delta x = R/2, \Delta y = R/2, \Delta z = R/2$) located 4 nm away from the surface. The resonance wavelength and the corresponding average field enhancement are then recorded in a text file. This computational "screening" process continues within a specified range, with steps of 2 nm, ranging from $R_{\min} = 6$ nm to $R_{\max} = 76$ nm.

Figure 3.2 illustrates the relationship between the sphere's radius and the peak wavelength in the average field enhancement. The simulation results align well with the theoretical model of the Modified Long-Wavelength Approximation (MLWA),⁴ indicating the limited tunability of the plasmonic resonance for this simple morphology. This red-shift can be attributed to dynamic depolarization of the nanoparticle.⁴

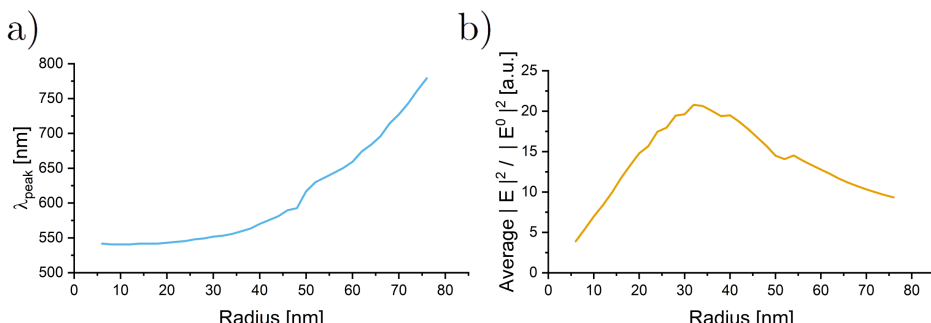


Figure 3.2: a) Peak position and b) intensity of the average field enhancement of gold nanospheres in water, measured in a volume 4 nm away from the surface of the particle, as a function of radius. Larger radii correspond to stronger peak's redshift and lower field enhancement.

The dampening and broadening of the field enhancement for particles with radii larger than ~ 30 nm can be attributed to the radiative damping arising from the spontaneous emission of radiation by the induced dipole.⁴ Despite having already predicted such behaviour theoretically in the previous chapter, these simulations are valuable for verifying the reliability of the employed method and directly computing the local electric field instead of relying on indirect estimates. The same conclusions can be drawn from Fig. 3.3.

3

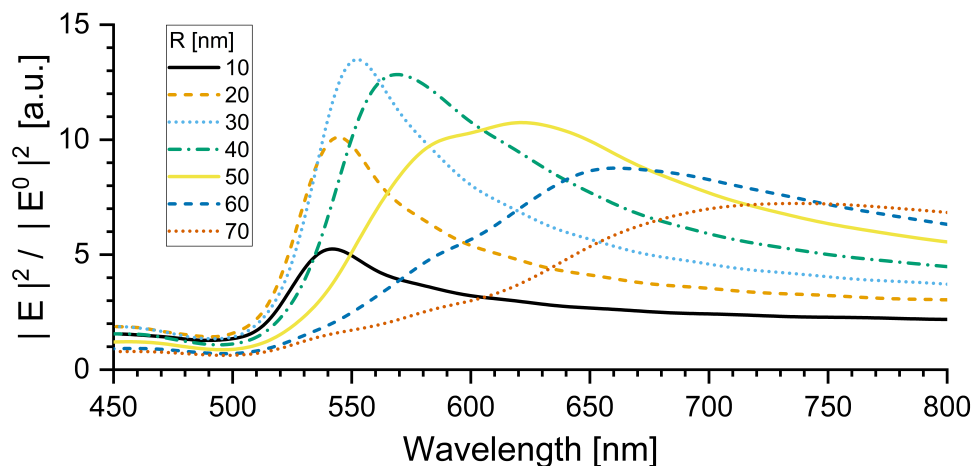


Figure 3.3: Spectra of gold nanospheres immersed in water for different radii. The smaller nanoparticles (10-40 nm) have a resonance peak around 550 nm. The resonance peaks are redshifted for the larger particles, with some even going into the IR region. For particles larger than ~ 30 nm, the width of the peak is significantly broadened.

The initial findings have brought to light the importance of finding a shape that offers a more tunable and intense plasmonic resonance. This realization has led us to explore the potential of utilizing the peak splitting observed in ellipsoids. The idea is then to identify a shape similar to the ellipsoid, but also practical and straightforward to fabricate with techniques like electron beam lithography.

3.3. SMOOTH GOLD NANORODS

In this section, we focus on realistic nanorods that do not have very sharp edges. In a sense, they are similar to ellipsoids, but present flatter surfaces and have overall larger volumes. These nanorods are particularly interesting due to their unique plasmonic properties and tunability, and could be nanofabricated in regular patterns.

Numerical simulations of gold smoothed nanorods were performed using the script for Lumerical's FDTD Solutions, which is publicly available in the GitHub repository.³

In brief, the code varies the three main parameters (namely length l , width w and height H) of the smoothed rod immersed in water and computes the maximum average field enhancement $|E|^2 / |E^0|^2$ in a small volume ($\Delta x = w/2, \Delta y = w/2, \Delta z = H$) 4 nm away from the surface. Then, the resonance wavelength and the corresponding average

field enhancement are saved in a text file. This computational screening continues in a defined range by steps of 5 nm:

- $20 \text{ nm} \leq l \leq 100 \text{ nm}$;
- $20 \text{ nm} \leq w \leq 50 \text{ nm}$;
- $20 \text{ nm} \leq H \leq 50 \text{ nm}$;

To save computational time, the script skips tests with higher l if the resonant wavelength is longer than 780 nm (outside the region of interest).

3

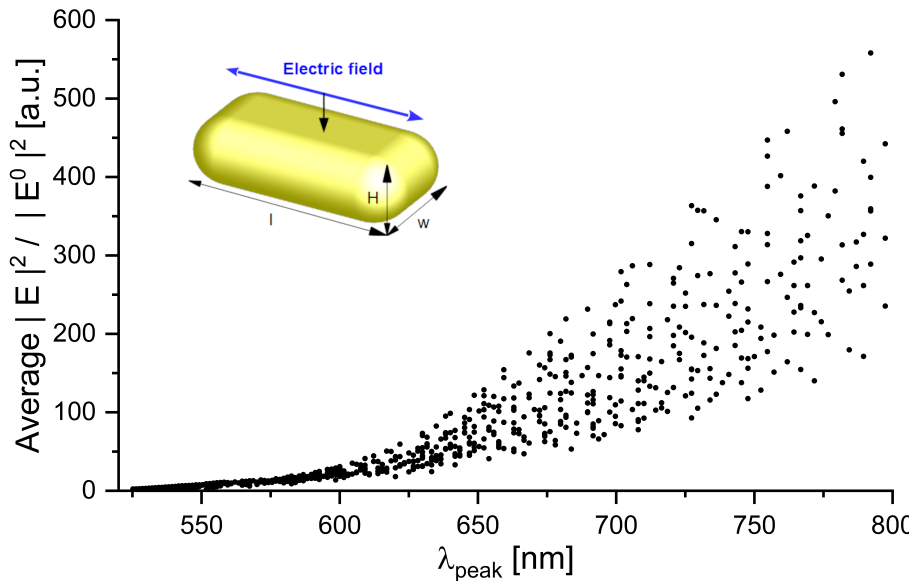


Figure 3.4: Results of the computational screening of gold nanorods, where each spot corresponds to a set (l, w, H) .

In Figure 3.4, each data point corresponds to the field enhancement of an individual nanorod with a fixed combination of dimensions (l, w, H) . The ranges chosen for the simulations focused solely on the longitudinal resonance, resulting in the absence of the transverse resonance in the graph. As anticipated by the theory of elongated particles⁴ and consistent with previous nanorod experiments,⁵ the field enhancement becomes stronger as the resonance is red-shifted. This behaviour is directly related to the aspect ratio of the nanoparticle.

Notably, these simulations deviate from other studies by taking into account various values for the height H rather than treating it as negligible. The effect of height is qualitatively similar to that of changing the width, contributing to multiple combinations of parameters yielding similar resonance wavelengths.

Based on the graph, it is evident that significantly higher field enhancements can be achieved at longer wavelengths. Moreover, an empirical formula for the resonance wavelength λ_{peak} has been derived from a multi-parameter fit of the data:

$$\text{For } \frac{l^2}{wH} > 1, \quad \lambda_{\text{peak}} = \left[432 + 111.4 \sqrt{\frac{l^2}{wH}} \right] \text{ nm}, \quad \epsilon \lesssim 5\% \quad (3.25)$$

where ϵ is the percentage relative error.

This fit function considers the dependence of the plasmonic resonance on the aspect ratios l/w and l/H ⁵. While adding these two terms individually did not yield satisfactory results, considering their product resulted in data points aligning closely with a square root function. Applying the square root to the product of l/w and l/H demonstrated a linear dependency for wavelengths greater than 540 nm, as illustrated in Figure 3.5.

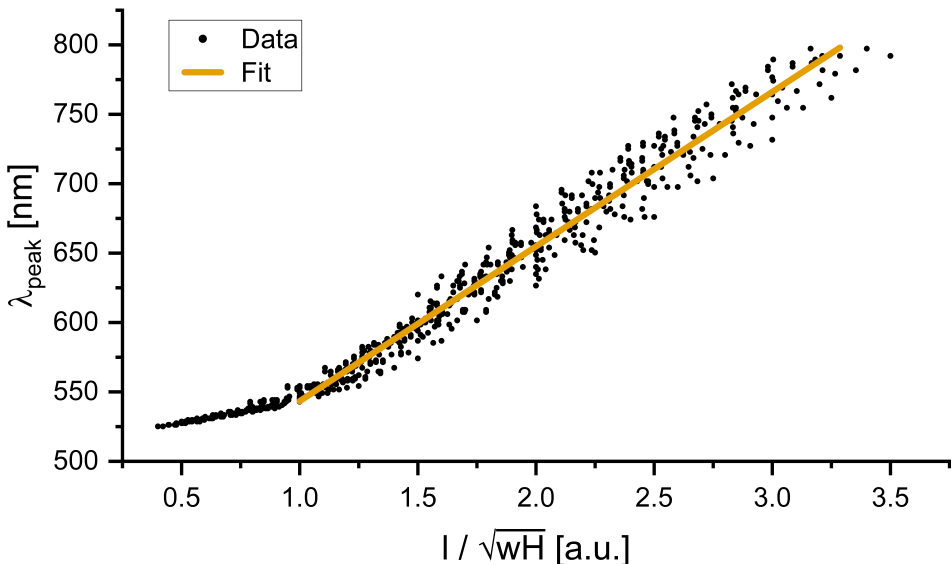


Figure 3.5: Empirical relation between wavelength peak position and aspect ratios.

It is essential to clarify that this fit function should not be regarded as an explanatory or descriptive model of the system. Instead, it provides a rapid approximation of the peak location based on a given set of parameters. It is applicable only to smoothed gold nanorods immersed in water.

While the smooth gold nanorods exhibit tunability within a desirable range (near-IR), two main challenges arise with this morphology. First, when these nanorods are nanofabricated on a substrate, the field enhancement remains confined to that plane. Given that biological applications occur in complex three-dimensional environments, this limitation poses a significant obstacle. On the other hand, if the nanorods are synthesized in a colloidal solution, achieving precise control over their orientation becomes difficult. Consequently, there is a risk of exciting the blue-shifted transverse mode instead of the more intense longitudinal mode.

To address these limitations and build upon the concept of elongated features, we look to spiked nanoparticles as the next logical step. By combining the elongated aspect

with the rotational symmetry of spheres, spiked nanoparticles offer promising possibilities. These structures hold the potential to overcome the challenges faced by smooth nanorods and provide enhanced control over plasmonic resonances in three-dimensional environments.

3.4. OCTAHEDRAL SILVER NANOPARTICLES

Having established a solid understanding of plasmonic resonance in smooth nanoparticles, we can now explore the realm of nanostars, which offer even more significant local enhancement thanks to their sharp tips. An octahedral nanostar structure was employed to address the issue of rotational dependence in the enhancement. This particle exhibits rotational symmetry in multiple directions, simplifying the simulation process. Instead of varying multiple rotation angles, only one angle needed to be adjusted to capture the complete 360-degree behaviour of the enhancement.

For this section, the material of the nanoparticles was arbitrarily chosen as silver instead of gold, thanks to the input from the supervised student who contributed to this research. Since our focus is primarily on the impact of shape, the choice of material should have minimal influence on our analysis and treatment.

Numerical simulations of silver octahedral nanostars were performed using the script for Lumerical's FDTD Solutions, which is publicly available in the GitHub repository.³ The conical base was set to have a conical angle of either 25 degrees or 40 degrees. To create the rounded tips, the truncated cone was connected to a semisphere, with the semisphere's radius set to 0.05 times the particle's radius ($0.05R$). Additionally, the length of the spikes was determined to be 1.5 times the particle's radius ($1.5R$). This conical structure more realistically represents a physical nanostar compared to a cone with an infinitely sharp tip.

In order to assess the bandwidth of the enhancement, simulations were conducted by rotating the particle between 0 and 45 degrees. Further rotations beyond this range were deemed redundant due to the 4-fold symmetry of the particle. Throughout the simulations, the monitor remained fixed to maintain consistency. This comparative analysis aimed to provide insights into the distinctive properties and performance of the nanostar structure as a function of rotation.

As visible in Fig. 3.6.a, there is a strong dependence of the field enhancement intensity on the rotation of the particle. However, the wavelength at which the plasmonic resonance occurs is very stable. Here, the center spherical particle had a radius of 20 nm, and the spikes had a length of 30 nm; therefore, the characteristic length of the nanostar is $2 \cdot (20 + 30) = 100$ nm. Therefore, we compare it to a spherical nanoparticle with a diameter of 100 nm to get a rough comparison for the practicality of the nanostar. We want the average enhancement of the nanostar to be higher than the spherical silver nanoparticle.

By calculating the average enhancement per degree over the entire range of rotation, we find an average enhancement of 12 per degree. Since the enhancement of the spherical particle does not change under rotation, the average enhancement is simply the maximum enhancement, so 13.5 per degree. We observe that, on average, the enhancement of the nanostar is less high than the spherical particle in the visible spectrum. In an effort to increase this bandwidth, we tested a different conical base angle of the spikes

3

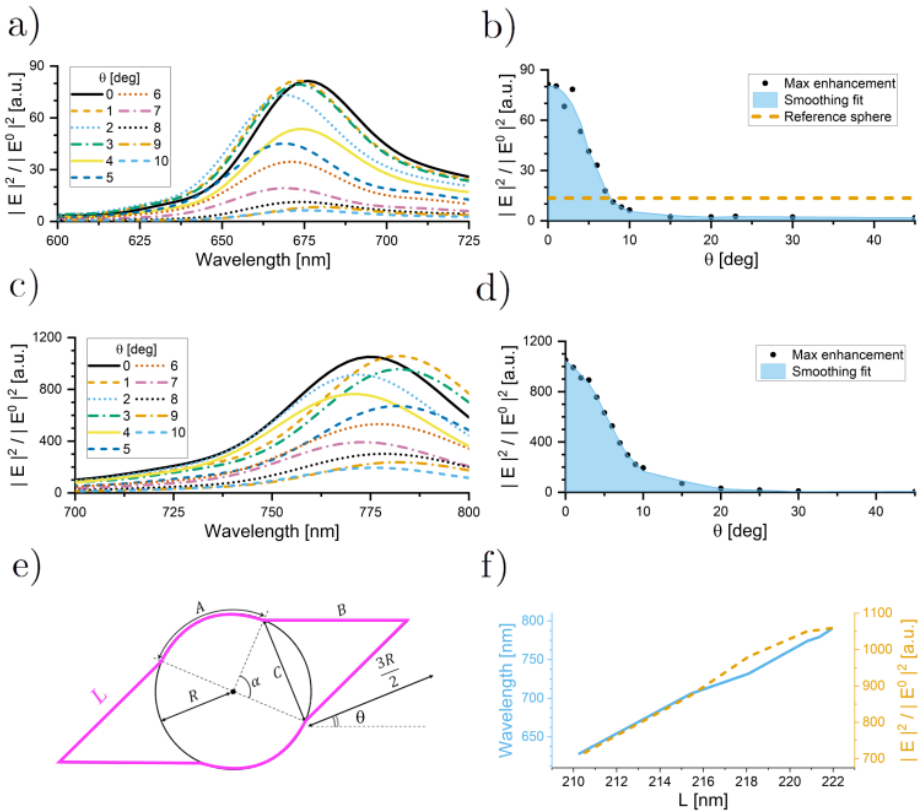


Figure 3.6: Rotation angles (θ) don't significantly change the peak position of the plasmonic resonance, but they affect the local on-axis field. Larger base angles (α) result in red-shifted and more intense plasmonic peaks. Both peak position and field enhancement are linearly dependent on the perimeter L of the section in the observed plane (in magenta).

while keeping the radius and spike length the same (Fig. 3.6.c).

The results reveal a remarkable enhancement peak in the nanostar structure, surpassing previous simulation findings by over an order of magnitude. Additionally, similar to the earlier observations, the wavelength corresponding to this higher enhancement peak remains relatively stable even when the particle is rotated. Regrettably, the spectrum bandwidth remains essentially unchanged compared to the previous simulations. However, the significant increase in enhancement values leads to a noteworthy rise in average enhancement per degree, reaching an impressive value of 167 per degree. Compared to its spherical counterpart with a similar characteristic length (as discussed earlier), the nanostar exhibits a substantially higher average enhancement.

The characteristic length so calculated is independent of the conical aperture of the spikes, therefore not explaining the different behaviours in Figs. 3.6.a and 3.6.c. A different way to evaluate the characteristic length is calculated according to the definitions in 3.6.e as the perimeter (in the section plane) of the particle. The perpendicular spikes are

neglected as they do not affect the plasmonic enhancement (transverse mode).

The formula used to calculate the characteristic length, with α in radians, is:

$$L = 2R \left[\pi - \alpha + 2\sqrt{\sin^2\left(\frac{\alpha}{2}\right) + \frac{9}{4}} \right] \quad (3.26)$$

We considered conical base angles ranging from 38 to 60 degrees, as these angles correspond to peaks within the visible spectrum. Using Eq. (3.26), we calculate the perimeter lengths and plot them against both the resonance wavelength and the maximum enhancement in Fig. 3.6.f. Both the maximum enhancement and the peak resonance wavelength exhibit a linear relationship with the perimeter length.

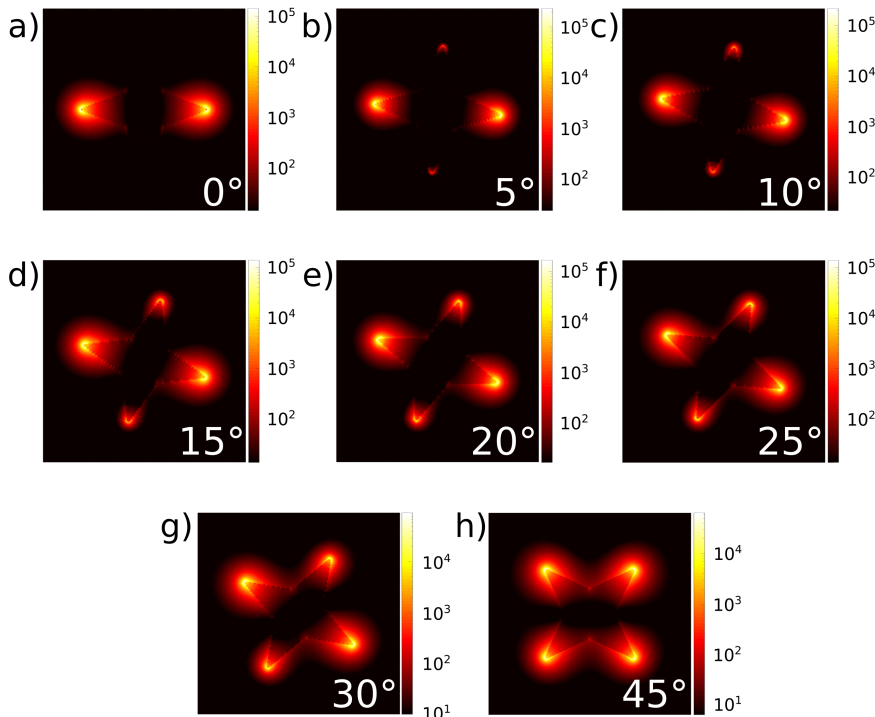


Figure 3.7: Field enhancement maps for a silver octahedral nanostar with 40 degrees of conical angle, for different rotations, at the resonance wavelength (774 nm). The maximum enhancement close to the tip is roughly the same order of magnitude, but this localization results in a lower field enhancement on the x-axis for some rotation angles.

Figure 3.7 clearly demonstrates the persistence of an intense plasmonic effect in the spiked nanoparticle; however, the localization of this effect at the tip implies that the measured field within a fixed window will significantly decrease as the nanoparticle undergoes rotation.

Given the orientation-dependent nature of octahedral nanoparticles, we contemplated the idea of utilizing a spiked nanoparticle with a high density of tips as a potential solution to overcome this challenge. The abundant spikes in such a structure could offer

advantages in terms of orientation insensitivity, allowing us to explore plasmonic properties more effectively.

3.5. HIGHLY SPIKED GOLD NANOSTARS

Numerical simulations of highly spiked gold nanostars were conducted using the script for Lumerical's FDTD Solutions, which is publicly available in the GitHub repository.³

In brief, the code performs simulations by varying the core radius R of the nanostar immersed in water, keeping the tip length fixed at 10 nm. The primary goal is to compute the average field enhancement $|E|^2/|E^0|^2$ within a small volume ($\Delta x = R_{\text{core}}, \Delta y = R_{\text{core}}, \Delta z = R_{\text{core}}$) positioned 4 nm away from the surface. Subsequently, the resonance wavelength and the corresponding average field enhancement values are recorded in a text file. Additionally, the code saves the absorption and scattering cross-sections as functions of the wavelength. The simulations cover a defined range, incrementing the core radius by 5 nm, spanning from a minimum core radius of $R_{\text{core,min}} = 20$ nm to a maximum core radius of $R_{\text{core,max}} = 50$ nm.

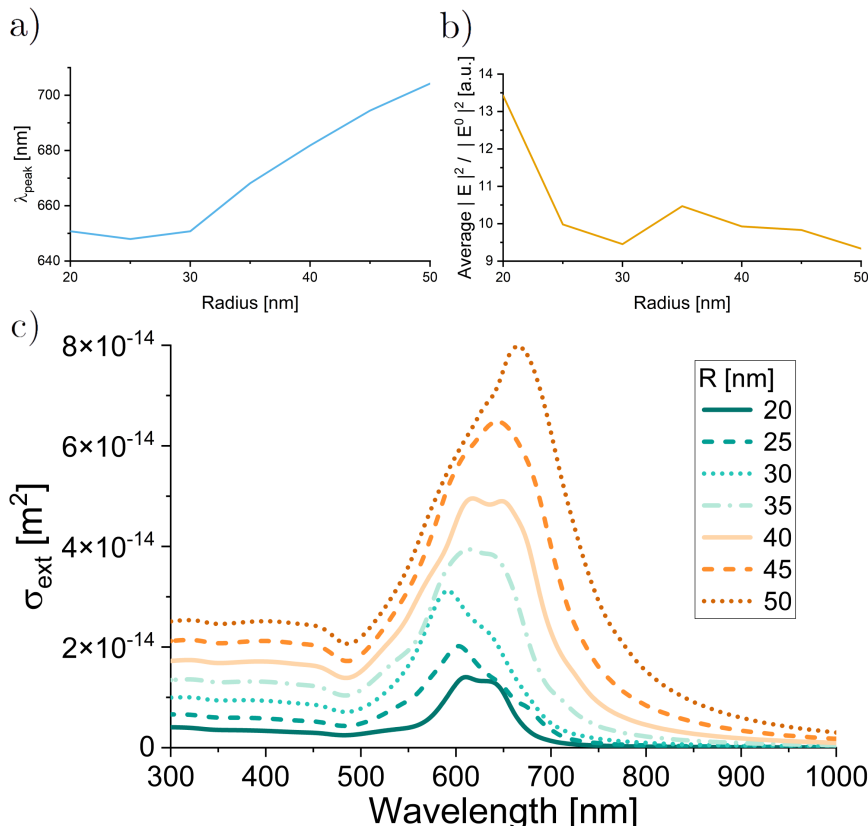


Figure 3.8: Screening of gold nanostars (high spike density) in water; larger radii correspond to stronger peak's redshift. Field enhancement is not significantly dependent on core size.

The presence of the tips in the nanostars, as anticipated from the theory,⁶ leads to an immediate red shift of approximately 100 nm compared to the plasmonic resonance observed in gold spherical particles of the same size. Unlike nanospheres, nanostars exhibit a more limited shift in resonance wavelength when the core size is altered, allowing for finer tunability of the peak. The initial blue shift is attributed to the competing effects of absorption and scattering, as illustrated in Fig. 3.8.

Interestingly, due to the presence of the spikes, the absorption peak consistently appears blueshifted relative to the scattering peak. Consequently, this results in a general blue shift when larger particles are grown, followed by a subsequent red shift. Fig. 3.8 offers a comprehensive comparison, outlining the primary effects of growing larger nanostars. The most notable effect is the significant broadening of the peak, resulting from non-dipolar effects, which leads to a less selective plasmonic resonance.

The simulation work focusing on highly spiked nanostars, characterized by a high density of tips around the spherical core, primarily remained theoretical. Nevertheless, these simulations already indicated the potential of such a morphology in achieving a favourable combination of resonance control, field enhancement engineering, and insensitivity to rotations. To make the study more relevant and applicable to real-world scenarios, it became essential to identify an existing synthesis protocol capable of producing gold nanostars with the plasmonic peak positioned in the red region of the visible range. Thus, to bridge the gap between theory and practicality, we adapted and applied these simulations to realistic gold nanostars.

3.6. REALISTIC GOLD NANOSTARS

Up until now, our simulations have relied on literature-based and expected effects, providing valuable theoretical insights. However, for the forthcoming biological application in the next chapter, it is crucial to assess the realistic field enhancement rather than relying solely on ideal theoretical values. This pragmatic approach prevents biased expectations in experiments and enables a more effective explanation of observed effects. Consequently, our focus shifts towards modeling ideal nanoparticles based on the scanning electron microscopy (SEM) characterization of real, synthesized nanoparticles produced via colloidal synthesis.⁷

To generate a diverse array of nanostars, we employed the versatile free software Blender, which facilitates the creation of complex meshes using Python scripts. The script, publicly available in the GitHub repository,³ initiates the process by generating an icosahedron, consisting of 20 equilateral triangles and 12 vertices. This choice of a sphere-like shape ensures that the vertices have a more regular distribution, mirroring the tip arrangement on realistic gold nanostars. The script then skillfully "opens" each vertex and extends it outward to form the desired tip structure. However, to attain a smoother-looking star, we apply a Subdivision Surface Modifier (SubSurf) to split the faces into smaller ones on the final mesh. This approach also eliminates the presence of infinitely sharp tips, preventing any artefacts in the field enhancement. Nevertheless, it's worth noting that this smoothness comes at the cost of increased memory size in the final .stl file.

For these simulations, we found that a mesh size of 35 Meshes Per Radius (MPR) provides acceptable results and ensures that the simulated plasmonic peak aligns with

the actual wavelength. Therefore, this value has been consistently employed for all our simulations.

Inspired by the realistic shape of gold nanostars synthesized via colloidal synthesis,⁷ we define our model nanostar with a core radius of $R = 25$ nm and a tip length of $L_{\text{tip}} = 10$ nm. This model nanostar serves as the benchmark for our simulations and allows us to assess the behaviour of realistic nanostars in comparison to the theoretical model.

3

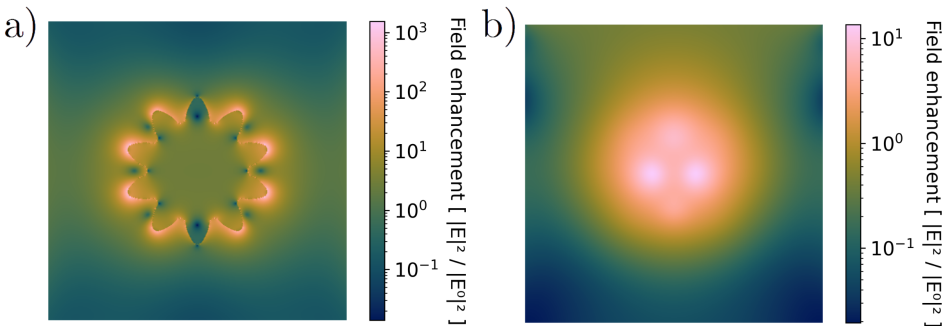


Figure 3.9: Field enhancement map for the model nanostar at the resonance wavelength of 650 nm, a) in the XY plane ($z = 0$ nm), and b) in the YZ plane ($x = 4$ nm).

Figure 3.9 illustrates that, similar to octahedral nanostars, the highest field enhancement occurs at the tips of the star. However, the nanostars in this figure present an intriguing intermediate scenario between high tip density nanostars and octahedral nanoparticles. Specifically, at the resonance frequency, the regions between the tips exhibit a significant field enhancement. The reduced orientation dependency observed in these nanostars is a highly advantageous feature, especially for their biological applications. In fact, these nanostars offer more predictable and consistent interactions with target fluorescent proteins.

Considering that these realistic nanoparticles possess the desired properties and exhibit a sufficiently intense field enhancement (approximately 10^1 or higher), it became crucial to explore the impact of defects and imperfections, such as missing tips or deviations from the ideal model, on the plasmonic resonance. Addressing this question was of paramount importance, especially since colloidal synthesis often results in nanoparticles with diverse shapes that cannot be fully controlled. Understanding whether minor defects could completely disrupt the plasmonic resonance at the desired frequency was necessary to assess the applicability of these nanoparticles in naturally disordered biological environments. Clearly, the symmetry boundaries in the simulation had to be disabled.

To investigate this, the first step involved removing a fraction of tips from random positions in the nanoparticle and then randomly rotating the nanoparticle while keeping the monitoring position fixed. Each tip density was subjected to 25 simulations. The model nanostar used in this study featured 42 spikes, and for partially covered nanostars, the number of spikes was approximated to the nearest integer.

The results of these simulations are presented in Fig. 3.10. From them, we can infer

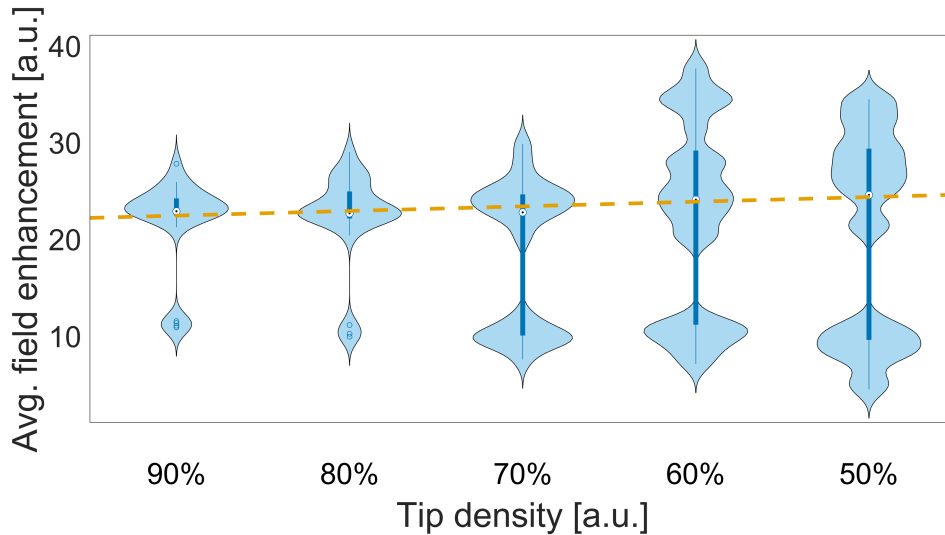


Figure 3.10: FDTD simulations of gold nanostars with a core radius of 30nm and a tip length of 10nm , with different tip densities. For each simulation, the position of the missing tips was randomized, as well as the orientation of the nanostar. Note: the same plot is reproduced in Chapter 4, as part of a published manuscript.

three essential effects. Firstly, we observe a noticeable bi-modal splitting in the enhancement curves. The primary mode remains the strongest, but the second mode becomes more significant at lower tip densities. This effect can be attributed to the alignment of the power monitor with the missing tip: in the direction of oscillation, the characteristic length can significantly impact the peak position. Additionally, the field may be weaker because it is relatively farther from the surface of the rotated or missing tip.

The second effect is the emergence of higher field enhancements at the resonant frequency compared to the ideal case. This can be explained by a similar reason as before: missing tips in the transverse direction can partially enhance the longitudinal resonance. This case would be beneficial to our application.

The third and most relevant effect we observe is that the median field enhancement is hardly affected by the tip density. This implies that in the case of a sufficiently dense population of nanostars under the sample, we should still be able to detect a similarly enhanced fluorescence signal. Overall, we can confidently conclude that missing tips do not significantly diminish the plasmonic effect we are pursuing. Therefore, the synthesis protocol does not necessarily have to yield perfectly identical nanostars to remain suitable for the intended biological application.

A second series of simulations was conducted to address random variations in the nanostars resulting from tip growth, which may not align perfectly in the ideal direction or attain the exact ideal length. This study accounted for the inherent unpredictability of the local growth process of tip formation during nanostar synthesis. To quantitatively assess this somewhat qualitative effect, we employed the "randomness factor" as defined in the software Blender, which was utilized to create the nanoparticles. This factor, ranging from 0 to 1, allowed for the random displacement of the node position corre-

sponding to the tip. A value of 0 corresponds to the model nanostar (no variation), while a value of 1 means that each tip node is randomly displaced anywhere within a sphere with a radius equal to its length. As before, 25 simulations were conducted for each case to ensure statistical robustness, and each configuration was randomly oriented.

3

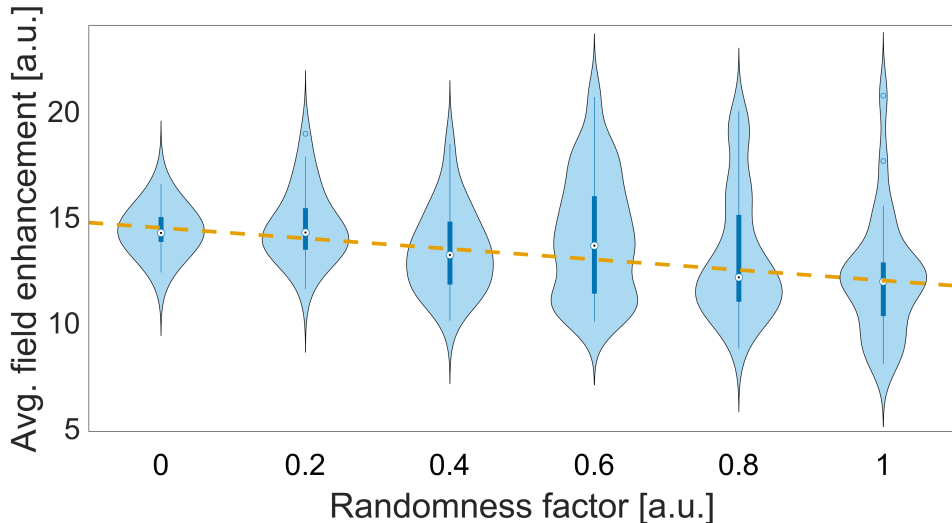


Figure 3.11: FDTD simulations of randomized gold nanostars, from an initial ideal particle with a core radius of 30 nm and a tip length of 10 nm . For each simulation, the tip vertices position was randomized, as well as the orientation of the nanostar. Note: the same plot is reproduced in Chapter 4, as part of a published manuscript.

Unlike the previous case, Fig. 3.11 does not exhibit bi-modal splitting, but rather shows a relatively significant broadening of the distributions. Overall, it appears that in the presence of higher randomness, there are more combinations that have a detrimental effect on the field enhancement compared to favorable ones. Although there is a slight decrease in the median field enhancement at higher levels of randomness, this difference is not substantial enough to render imperfect nanostars unusable, as a majority of the time, the enhancement factor remains at 10 or higher.

The careful reader may observe that the field enhancements in Fig. 3.11 for high tip density are lower than those in Fig. 3.10 with no randomness. This is attributed to an adaptation we introduced to the sharpness of the tip, as at high random factors, the tips tended to stretch in unphysical ways, resulting in overly sharp edges. Despite this discrepancy, the comparison remains relevant because our primary interest lies in identifying trends rather than precisely quantifying the field enhancement numerically.

The analysis of a realistic nanostar highlights the robustness of the field enhancement effect in the presence of imperfections and random variations. Nanostars synthesized through colloidal growth are well-suited for enhancing the overall plasmonic effect in a disordered environment, such as a biological one.

3.7. DISCUSSION AND CONCLUSIONS

In this chapter, we explored the plasmonic properties of various nanoparticle shapes using numerical simulations with the Finite-Difference Time-Domain (FDTD) method. The main goal was to engineer the plasmonic resonance to achieve the best coupling to the emission of fluorescent proteins of interest, peaking in the red region (around 700 nm) and having the tail in the near-IR.

We began by investigating the plasmonic properties of gold nanospheres in water. The simulations showed that the resonance wavelength red-shifts for larger nanospheres due to dynamic depolarization. The simulation results agreed well with the theoretical model of the Modified Long-Wavelength Approximation (MLWA). However, the limited tunability of the plasmonic resonance in spherical nanoparticles constrained their potential applications.

To overcome the limitations of nanospheres, we explored smooth gold nanorods as an alternative. The simulations demonstrated that the resonance wavelength could be tuned by adjusting the aspect ratios of the nanorods. We derived an empirical formula to approximate the resonance wavelength based on the aspect ratios. Although smooth nanorods showed tunability within the desired range, they were limited to the plane of their substrate and lacked precise control over their orientation.

In an effort to overcome the limitations of smooth nanorods, we investigated octahedral silver nanostars. These nanostars exhibited strong field enhancement at the tip, resulting in a significant increase in the average enhancement per degree compared to smooth nanoparticles. However, the enhancement was highly localized at the tip and significantly decreased as the nanostar underwent rotation.

To address the rotational sensitivity of octahedral nanostars, we proposed highly spiked gold nanostars. The simulations showed that these nanostars exhibited red shifted resonance wavelengths compared to spherical nanoparticles of similar size. The presence of spikes resulted in a significant increase in field enhancement, and the peak resonance wavelength was less dependent on the core size. However, such nanostars were still theoretical models, not based on any experimental evidence.

In the pursuit of practical applications, we sought to bridge the gap between theory and experimental realization. We adapted the simulations to realistic gold nanostars by identifying a suitable synthesis protocol that achieved the desired plasmonic peak in the red region of the visible range. These realistic nanostars showed promise in achieving a favourable combination of resonance control, field enhancement engineering, and insensitivity to rotations, making them a promising candidate for biological applications.

The exploration of these shape effects has significantly enriched our understanding of plasmonics and offered insights that were otherwise unattainable through analytical modelling alone in the previous chapter. Although the optimal field enhancements for realistic gold nanostars hover around a factor of 10, it is crucial to note that this value represents an average calculated over a considerable volume in close proximity to the nanoparticle, rather than the maximum achievable enhancement. Hence, these results can be confidently considered realistic and attainable, even under uncontrollable sub-optimal parameters. Armed with these findings, we can confidently proceed to the next chapter, where we will build upon the solid hypothesis that such realistic nanostars are well-suited for plasmonic enhancement in biological applications.

BIBLIOGRAPHY

- [1] Kane Shee-Gong Yee. "Numerical Solution of Initial Boundary Value Problems Involving Maxwell's Equations in Isotropic Media". In: *IEEE Transactions on Antennas and Propagation* 14.3 (1966). ISSN: 15582221. DOI: [10.1109/TAP.1966.1138693](https://doi.org/10.1109/TAP.1966.1138693).
- [2] David J. Griffiths. *Introduction to Electrodynamics*. Cambridge University Press, 2017. DOI: [10.1017/9781108333511](https://doi.org/10.1017/9781108333511).
- [3] *GitHub repository*. URL: <https://github.com/Brinkslab/FDTD-Plasmonics/>.
- [4] Marco Locarno and Daan Brinks. "Analytical calculation of plasmonic resonances in metal nanoparticles: A simple guide". In: *American Journal of Physics* 91.7 (July 2023), p. 538. ISSN: 0002-9505. DOI: [10.1119/5.0094967](https://doi.org/10.1119/5.0094967). URL: <https://doi.org/10.1119/5.0094967>.
- [5] Stephan Link and Mostafa A. El-Sayed. "Spectral Properties and Relaxation Dynamics of Surface Plasmon Electronic Oscillations in Gold and Silver Nanodots and Nanorods". In: *Journal of Physical Chemistry B* 103.40 (1999). ISSN: 15206106. DOI: [10.1021/jp9917648](https://doi.org/10.1021/jp9917648).
- [6] Lukas Novotny and Bert Hecht. "Optical antenna probes". In: *Principles of Nano-Optics*. 2nd. 2009. Chap. 6.5, pp. 188–192. DOI: [10.1017/CBO9780511794193](https://doi.org/10.1017/CBO9780511794193).
- [7] Silvia Barbosa et al. "Tuning size and sensing properties in colloidal gold nanostars". In: *Langmuir* 26.18 (2010). ISSN: 07437463. DOI: [10.1021/la102559e](https://doi.org/10.1021/la102559e).

4

PLASMONIC ENHANCEMENT OF QUASAR6A IN LIVING CELLS USING GOLD NANOSTARS

This chapter translates our theoretical and computational insights into a practical application by demonstrating plasmonic enhancement in living cells. We show that gold nanostars, with their tailored sharp-tip geometry, can be precisely engineered to couple with the fluorescent protein QuasAr6a at the plasma membrane. By carefully controlling nanoparticle spacing and orientation, we achieve a robust increase in fluorescence intensity as well as an acceleration in voltage-response kinetics. Our experimental findings confirm that manipulating the local electromagnetic environment through plasmonic nanoparticles offers a powerful means to alter the protein photocycle without genetic modifications.

4.1. INTRODUCTION

Plasmonic nanoparticles are key components in nanophotonics^{1,4,5,6,7,8,9,10,11,2,3} and have applications in molecular detection and diagnostic platforms.^{12,13,14} Coupling of dipoles to plasmonic antennas has allowed engineering of qualitatively altered behavior in isolated quantum systems,^{10,15} but this promise has not been fulfilled in living systems, where the use of plasmonics is limited to tissue level applications of plasmonic particles as contrast agents¹⁶ or heat sources.¹⁷ Here we show that coupling to designed plasmonic nanoparticles can control the electrophysiological function of proteins in living cells. We designed nanostar geometries and achieved robust near-field coupling of these optimized nanoparticles to plasma membrane-localized Archaeorhodopsin proteins. We enhanced the fluorescence of the coupled rhodopsins and increased their response speed to membrane voltage. We incorporated this plasmonic enhancement into a Markov chain photocycle model of the Archaeorhodopsin mutant QuasAr6a, showing an increased fluorescence emission rate and manipulation of the protein photocycle dynamics through a combination of transition rate enhancements. These results represent the first scalable near-field coupling between plasmonic particles and fluorescent proteins in living cells. They show enhancement of protein function beyond what has been achievable through genetic engineering. This opens up a range of possibilities for engineering biological functionality through plasmonics.

The striking signal enhancements⁹ and altered quantum behavior¹⁰ that can be achieved by employing plasmonic nanoparticles in single-molecule fluorescence and SERS experiments⁶ depend on the exquisite near-field coupling between a plasmonic antenna and a molecular dipole of interest. These effects have been challenging to achieve in functional biological systems due to difficulties in the detection of small molecular signals over in vivo cellular backgrounds,^{18,19} accurate placement and orientation of nanoparticles for the required coupling,²⁰ and robust creation of finely tuned nanoparticles.²¹ Nevertheless, if those issues can be overcome, plasmonics is a promising tool to achieve enhanced signals, increased resolution, and top-down control in the optical detection and manipulation of biological systems.¹⁹

Coupling to plasmonic particles can influence dipoles in two main ways,²² both strongly distance-dependent.²⁰ First, the plasmonic particle can localize an excitation field through resonance or lightning rod effect⁷, leading locally to an enhanced electric field \vec{E} compared to a prior \vec{E}_0 , where the enhancement factor $|\vec{E}|^2 / |\vec{E}_0|^2$ leads to a higher photon absorption per unit time. Second, the radiative decay rate of a dipole is given by Fermi's golden rule⁴ and can be manipulated by altering the Local Density of Optical States (LDOS) through careful positioning of dielectric or metallic elements in the presence of the dipole.²² This effect can change the quantum yield of radiative transitions:

$$Y = \frac{\Gamma}{\Gamma + \Gamma_{nr}} \quad (4.1)$$

where Y is the radiative quantum yield of the transition, Γ is the radiative decay rate and Γ_{nr} is the non-radiative decay rate. Eq. (4.1) indicates that this can enhance low quantum yield processes (i.e. $Y \ll 1$): in this case, $\Gamma \ll \Gamma_{nr}$. Plasmonic enhancement can increase Γ , leading theoretically to a Y approaching 1 if the effect is strong enough.²²

Our interest in this technology was fueled by two realizations regarding light-sensitive

proteins: they often have a low fluorescence quantum yield,^{23,24} since they have typically evolved to use absorbed photons for performing a light-induced mechanical action;²⁵ and this action typically incorporate a large number of transitions with excitable dipoles (the photocycle)^{25,26} which suggests not only fluorescence, but also protein dynamics, and with it, function, could be influenced through plasmonics.

We reasoned that judicious design and application of plasmonic particle geometry and spacing might allow us to achieve these effects in living biological systems. We found sparse reference to attempts at plasmonic enhancement of fluorescence of proteins^{27,28}, one reference attempting fluorescence enhancement of fixed cells labeled with fluorescent dyes,¹⁸ and one in polymer and bacterial environments.²⁹ However, we did not find attempts at this in electrophysiologically relevant conditions, let alone while incorporating influence on protein dynamics, and set out to test the feasibility of our idea.

4.2. RESULTS

4.2.1. PARTICLE DESIGN

For enhancement of transition rates, in a first-order approximation, the resonance spectrum of the plasmonic particles should have maximum overlap with the action spectrum (absorption/emission) of the dipole of interest.²² For biocompatibility, it is particularly interesting if this spectrum is red shifted, ensuring lower phototoxicity and easier light penetration, and tunable to the dipole of interest.¹⁸ To achieve the best field enhancement, we first investigated the optimal particle geometry and material through Finite-Difference Time-Domain (FDTD) simulations of a series of nanospheres, nanorods and various types of spiked nanoparticles in biocompatible gold and silver. As expected from plasmonic theory³⁰ gold spheres exhibit a suboptimal, broad peak in the range of interest (520 nm in water, **Figs. 4.1a, 3.2-3.3**). Gold nanorods are highly tunable, but the emergence of two resonant modes imposes the need for highly accurate orientation (**Fig. 3.4**), as it does for nanostars with a few sharp tips (**Figs. 3.6-3.7**). However, highly spiked stars are tunable to the optimal wavelength in our range of interest (**Fig. 4.1a**) and their resonance is robust to rotation (**Fig. 3.8**). Furthermore, the localization of the field around nanospheres spans the entire surface of the sphere and reaches a squared field enhancement of the order of tens at best (**Fig. 4.1b**). In contrast, the local intensity of the electric fields around the sharp tips can be enhanced hundreds- or even thousands-fold (**Fig. 4.1c**).

The diffusive motion of nanoparticles in living biological samples might lead to changes in coupling distance and relative orientation to molecular dipoles, hampering plasmonic enhancement.²⁰ Nanostars might also suffer from irregularities in their makeup, influencing their maximal enhancement.³¹ We quantified both effects and found that the enhancement by nanostars was robust against these sources of noise (**Figs. 4.1d,e**, individual simulations in **Figs. 4.S1-4.S2**).

4.2.2. COLLOIDAL GROWTH OF NANOSTARS

Gold is a common metal for plasmonic applications, characterized by superior biocompatibility and low cytotoxicity,³² and was, therefore, the material of choice utilized throughout this study. To synthesize the gold nanostars, we adapted a colloidal, seed-mediated

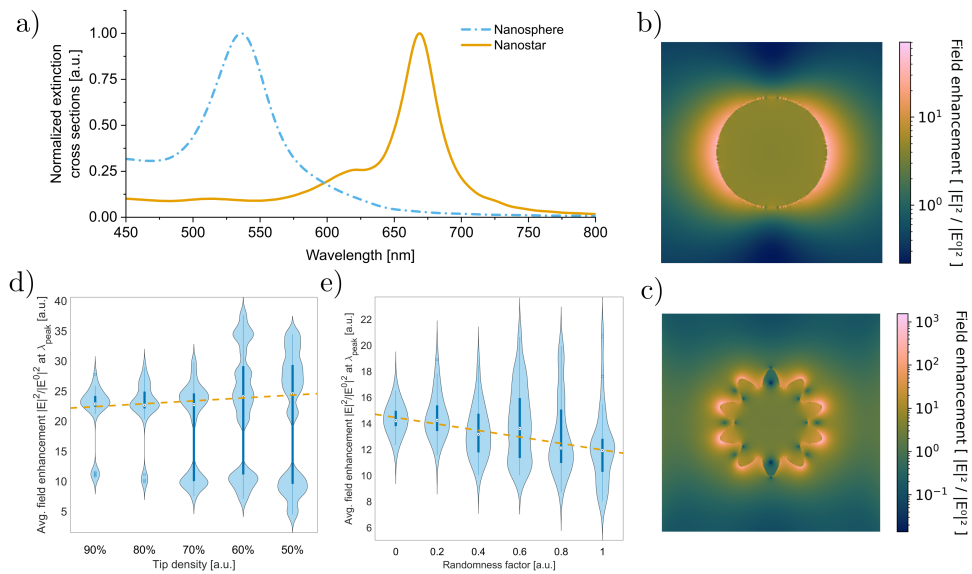
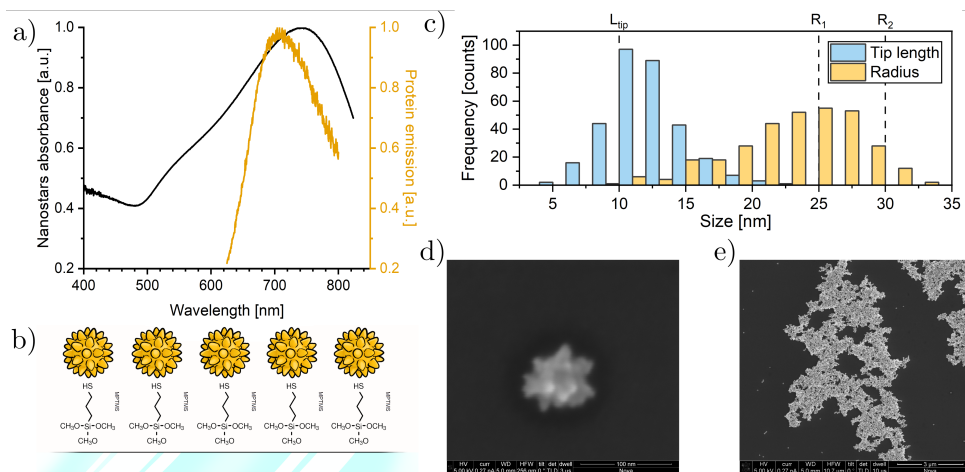


Figure 4.1: Gold nanostars are optimal candidates for in vivo plasmonic enhancement. **a**, FDTD simulated extinction cross sections of, respectively, a gold nanosphere and a gold nanostar in a watery environment. The simulated nanosphere has a radius of 25nm . The simulated nanostar has a core radius of 25nm and a tip length of 10nm . **b**, FDTD simulation of the field enhancement around a gold nanosphere in water at $\lambda = 540\text{nm}$. **c**, FDTD simulation of the field enhancement around a gold nanostar in water at $\lambda = 650\text{nm}$. The field is confined to a few nanometers around the nanostar spikes. **d**, FDTD simulations of gold nanostars with a core radius of 30nm and a tip length of 10nm , with different tip densities. For each simulation, the positions of the missing tips and the orientation of the nanostar were randomized. The individual results are shown in the Supplementary Information (Fig. 4.S1). **e**, FDTD simulations of randomized gold nanostars from an initial ideal particle with a core radius of 30nm and a tip length of 10nm . The tip vertex position and nanostar orientation were randomized for each simulation. The individual results can be found in the Supplementary Information (Fig. 4.S2).

growth protocol³¹ that allowed high control and tunability of the geometry. We synthesized a series of nanostars under varying seed and growth conditions (**Methods section**). We characterized the synthesized colloids through Energy Dispersive X-ray Spectroscopy (EDX, Fig. 4.S3) and Ultraviolet-Visible light (UV-Vis) spectroscopy. The optimal sample ($R = 30$) was selected based on the alignment of the absorbance peak to the emission peak of Archon1³³ (Fig. 4.2a); we attribute a minor mismatch to a red shift induced by polyvinylpyrrolidone (PVP) as a capping agent (Eq. (S.3)).

We performed quality control by immobilizing the gold nanostars on a silicon substrate with 3-mercaptopropyl trimethoxysilane (MPTMS) (Fig. 4.2b), following a custom protocol (**Methods section**), to examine them under a scanning electron microscope (SEM). The monodisperse nanostars had an average core radius of $r = 23 \pm 5\text{ nm}$ (mean \pm SD, Fig. 4.2c) and an average tip length $l = 12 \pm 3\text{ nm}$, (mean \pm SD, Fig. 4.2c) in agreement with the simulations. They were generally well separated (Fig. 4.2d), though occasional clustering in micrometer-sized aggregates was visible (Fig. 4.2e), possibly affecting the

measured plasmonic resonance.¹²



4

Figure 4.2: Colloidal gold nanostars are designed to enhance the fluorescence of QuasArs. **a**, Spectral alignment between the normalized absorbance of the gold nanostars colloid and the fluorescence emission of Arachon1.³³ **b**, Illustration of the gold nanostars bound to glass via MPTMS. Not in scale. **c**, SEM micrograph of an isolated gold nanostar. **d**, The physical features of the nanoparticles in SEM images match the ones used for the simulations in **Fig. 1**. $L_{tip} = 10$ nm is the tip length used in the simulation, and $R_1 = 25$ nm and $R_2 = 30$ nm are the two radii used in different simulations. **e**, SEM micrograph of a large, complex cluster of gold nanostars.

4.2.3. CALIBRATION USING CYANINE-5

We next optimized a protocol to localize plasmonic particles to fluorescent dipoles in wet lab conditions. We chose Cyanine-5 (Cy5) as a model molecule to enhance the fluorescence because of its emission peak position and moderate quantum yield (~30%).^{34,35}

We hypothesized that Biotin-Streptavidin binding would provide a suitable way to link nanostars to fluorescent emitters under physiological conditions, and compared the fluorescence readout of Streptavidin-Cy5 (Strep-Cy5), a mixture of Strep-Cy5 and citrate-capped nanostars, and Strep-Cy5 bound to biotin-coated nanostars (**Fig. 4.3a**). However, we found that the presence of nanostars reduced the fluorescence signal by up to $-68 \pm 16\%$ (mean \pm error, propagated from SD, **Fig. 4.3b**). We attribute this to a combination of the increased optical density in nanostar-containing samples,³⁶ and fluorescence quenching caused by non-radiative energy transfer from the fluorophore to the nanostar.¹ Streptavidin, the largest molecule in the binding complex, is around 5 nm,³⁷ keeping the fluorophore within the quenching range of the nanostar.¹

This experiment provided a baseline distance measurement, and we set out to increase the distance between the nanostars and the emitters. Using MPTMS, we immobilized gold nanostars functionalized with biotinylated Bovine Serum Albumin (bBSA), then added Strep-Cy5 (**Fig. 4.3c**). BSA can bind to gold primarily via strong electrostatic interactions, and secondarily via steric and hydrophobic interactions.³⁸ Fluorescence spectroscopy showed a net $42 \pm 6\%$ increase in the fluorescence intensity of Cy5 (peak value \pm error, propagated from noise SD, **Fig. 4.3d**), in agreement with the theoretical

value (Eq. (S.6)) considering the combined lengths of streptavidin (5 nm)³⁷ and BSA (8 nm)³⁹ as a spacer larger than the quenching range,¹ the already significant quantum yield of Cy5^{34,35}, and the estimated average field enhancement of a factor 1.78 from simulations (Fig. 4.S4).

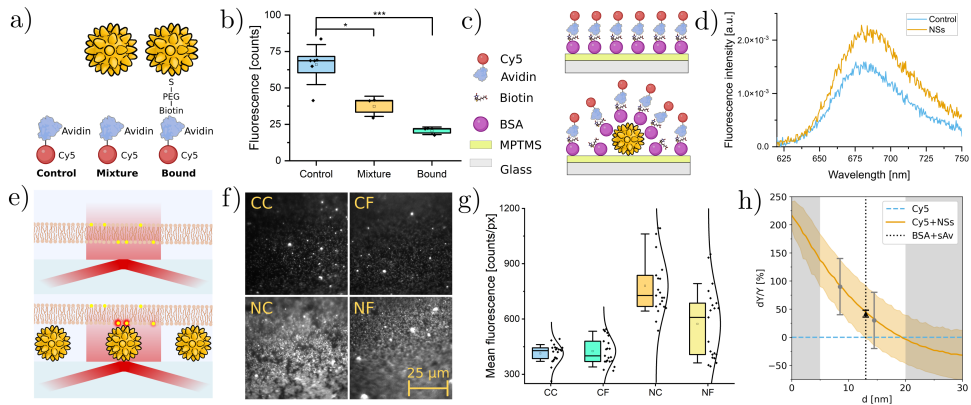


Figure 4.3: Control over nanostar-fluorophore coupling allows tunable plasmonic enhancement **a**, Illustration of fluorescence assays in solution. control: Cy5 labelled with streptavidin; mixture: control sample mixed with citrate-capped commercial nanostars; bound: Strep-Cy5 bound to biotin PEGylated gold nanostars. Biotin and streptavidin bind, ensuring a fixed distance between the nanostar and the fluorophore. Not to scale. **b**, Results from fluorescence spectroscopy at peak wavelength (666 nm). Boxes represent the standard errors, whiskers the SD, squares the means and mid-lines the medians. **c**, Illustration of fluorescence assay on glass substrate. **d**, Results from fluorescence spectroscopy in glass dishes. **e**, Illustration of TIRF microscopy of a fluorescently-labelled artificial membrane without (top) and with nanostars (bottom). Not to scale. **f**, Median TIRF images of the artificial membranes. Represented with the same brightness and contrast. **g**, Cross comparison of the fluorescence in DOPC lipid bilayers labelled with Cy5 dye, without Fibronectin or Nanostars (CC, 410 ± 50 counts/px), with Fibronectin (CF, 430 ± 70 counts/px), with Nanostars (NC, 780 ± 160 counts/px) or with Nanostars and Fibronectin (NF, 570 ± 190 counts/px). Boxes represent the 25-75% range, whiskers the 10-90% range, squares the means and mid-lines the medians. **h**, Predicted mean enhancement of Cy5 (orange, solid line) within the range of uncertainty (orange band, propagated from SD), based on simulation, compared to the natural Y of Cy5 (light blue, dashed line). Data points represent the measured enhancement in panel d (mean as the black triangle, error bar propagated from noise SD) and in panel g (means as the gray dots, error bars propagated from SD). Distances for measurements from g are determined by using the curve as a plasmonic ruler.

To apply plasmonic enhancement in living cells, this effect needs to be compatible with cell culturing conditions.¹⁸ For ease of coupling nanoparticles, we focus for now on proteins that are embedded in the lipid bilayer of the cell membrane.²⁵ Cells are typically attached to glass substrates using an extracellular matrix protein, like fibronectin.⁴⁰ Given the sensitivity of the enhancement to the dielectric environment, we wondered whether the lipid bilayer or fibronectin would influence the enhancement. We immobilized nanostars on glass and used Total Internal Reflection Fluorescence (TIRF) microscopy to investigate the effect of an artificial lipid bilayer and a standard fibronectin layer (Methods section, Fig. 4.3e). In this in vitro experiment, we positioned lipid bilayers labelled with Cy5 on the sample and imaged the fluorescence with and without nanostars, and with and without fibronectin (Fig. 4.3f). We measured a fluorescence enhancement of $90 \pm 50\%$ (mean \pm error, propagated from SD) associated with the di-

rect coupling between Cy5 and nanostars, while the presence of the fibronectin layer reduced the effect to $30 \pm 50\%$ enhancement (mean \pm error, propagated from SD), probably by acting as a spacer (Fig. 4.3g).¹ In combination with the Strep-Cy5 results (Fig. 4.3d), we estimate the distance between the Cy5 molecules and the nanostars to be 14.5 nm, respectively 8.5 nm with and without fibronectin (Fig. 4.3h), for an effective 6 nm thickness of the fibronectin layer.

4.2.4. PLASMONIC ENHANCEMENT IN LIVING CELLS

To test our system in living cells, we chose Archaerhodopsin as a model light-sensitive protein. Several mutations of this protein exist (Quasar1-6a,b;^{24,41,42} Archon1,2;⁴³ NovArch⁴⁴), which are all known for low quantum yield of fluorescence. Their emission spectrum, which was measured to be between 640 and 800 nm,^{23,33} is in an interesting range for bioimaging applications. Moreover, Archaerhodopsin3 is a voltage-sensitive proton pump,^{23,45,24,42} and all of its mutants have a photocycle and fluorescence that depend on the voltage across the cell membrane in which the protein is embedded, making it an interesting proof of principle model for manipulation of protein function using plasmonics.

Having shown that cell membrane embedding and fibronectin application do not hinder plasmonic enhancement of fluorophores, we performed a simple addition of colloidal nanostars to HEK293T cells expressing either QuasAr1 (Fig. 4.4a) or QuasAr6a (Fig. 4.4b).

We noticed an enhancement in the fluorescence of individual cells over time (Fig. 4.4c). We quantified the change in fluorescence of the cell population over time after the addition of the nanostars and noticed an increase of fluorescence to a factor $140 \pm 80\%$ (QuasAr1, mean \pm error, propagated from SE, Fig. 4.4a) and $28 \pm 12\%$ (QuasAr6a, mean \pm error, propagated from the SE, Fig. 4.4b) respectively.

We tested the difference between this simple application of nanostars and embedding them in the fibronectin layer. We immobilized gold nanostars on glass, coated the surface with fibronectin, and plated HEK293T cells expressing QuasAr6a (Fig. 4.4d). We screened the fluorescence at the bottom surface of the cell population (Fig. 4.4e) and achieved a fluorescence enhancement of $69 \pm 19\%$ (median \pm error, propagated from the SE), confirmed by the fluorescence brightness of the median cell in a control, respectively enhanced sample (Fig. 4.4f). The difference in enhancement of fluorescence between the nanostars applied to the top surface ($28 \pm 12\%$, Fig. 4.4b) to those embedded in the fibronectin adhesion layer ($69 \pm 19\%$, Fig. 4.4e) indicates that the glycocalyx^{46,47} surrounding the cells acts effectively as a spacer between the fluorophores and the nanoparticles applied to the top surface of the cells. The glycocalyx is thinner at the bottom of the cells because the formation of integrin-fibronectin bonds induces mechanical strain.⁴⁸ We estimated an effective distance from QuasAr6a of 13.5 nm for the nanostars embedded in the fibronectin layer and 16 nm for the nanostars deposited above the cells; we estimate the glycocalyx to cause an average of 8.5 nm spacing difference (Eq. (S.14)).

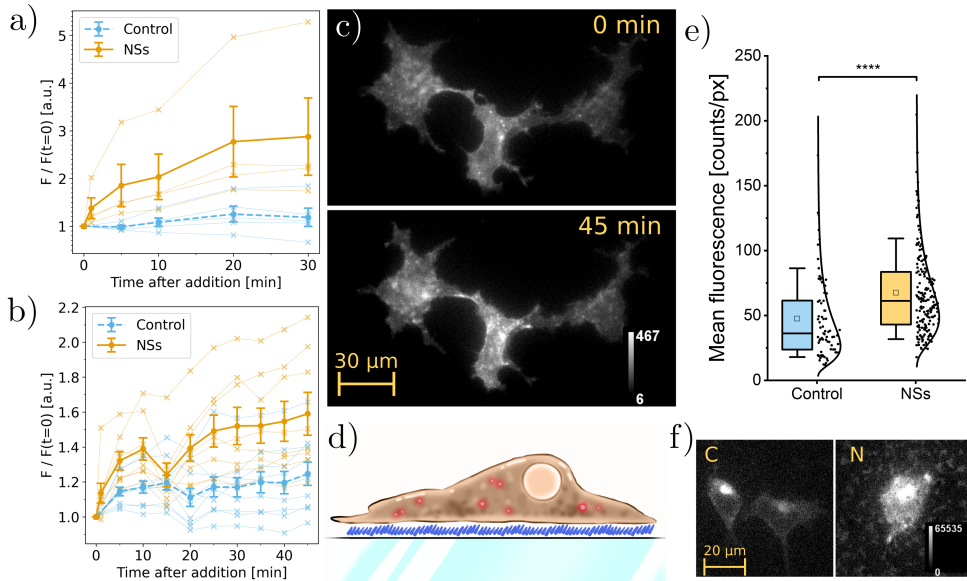


Figure 4.4: Gold nanostars enable plasmonic enhancement of QuasAr fluorescence in living cells. **a**, Mean fluorescence of cells expressing QuasAr1, normalized to the first frame, after the addition 400 μ l of nanostars solution (NSs), compared to no addition (control). Error bars correspond to the standard error. Over time, the nanostars gradually diffuse and sediment on the cells, enhancing the fluorescence. Crosses indicate individual measurements, filled circles averages across all trials. **b**, Mean fluorescence of cells expressing QuasAr6a, normalized to the first frame, after the addition 400 μ l of nanostars solution (NSs), compared to no addition (control). Error bars correspond to the standard error. Crosses indicate individual measurements, and filled circles averages across all trials. **c**, Example of fluorescent cells in the QuasAr6a test sample before and after the addition of nanostars. **d**, Illustration of a fluorescent HEK293T cell plated on fibronectin, layered above a glass dish covered in nanostars (in blue). **e**, Screening results show a statistical difference between a sample without (control) and with nanostars (NSs). Boxes represent the 25–75% range, whiskers the 10–90% range, squares the means and mid-lines the medians. Uncertainty propagated from the standard error. **f**, Comparison of the median cell in the control screening (left) and in the nanostars sample (right). Individual nanostars responsible for enhancement are too small to be distinguished but nanostar aggregates are visible either as dim autofluorescence outside the cell, or spot-like shadows under the cell.

4.2.5. PLASMONIC ENHANCEMENT OF PROTEIN FUNCTION

Fluorescence enhancement of dim genetically encoded voltage indicators like QuasArs is one possible application of coupling plasmonic antennas to proteins in living cell environments. Given that the kinetics of GEVIs are determined by a photocycle with potential absorption and emission events at multiple stages,^{45,49,25} we were interested in whether coupling to plasmonic antennas might also be used to enhance the protein function. We performed a voltage clamp experiment on HEK293T cells expressing QuasAr6a plated on fibronectin over immobilized gold nanostars to test this. We varied the voltage across the cell membrane in steps from -70 to +30 mV and recorded the fluorescence response without (Fig. 4.5a) and with nanostars in the fibronectin layer (Fig. 4.5b). We noticed a decrease in voltage sensitivity from a DF/F of 0.38 ± 0.07 to 0.11 ± 0.04 (mean \pm SD, Fig. 4.5c), mostly caused by the increase in baseline fluorescence,

rather than a change in the absolute response to voltage. However, we noticed a strong increase in response speed from $k_{up} = 170 \pm 90 \text{ s}^{-1}$ to $k'_{up} = 1300 \pm 400 \text{ s}^{-1}$ and $k_{down} = 220 \pm 110 \text{ s}^{-1}$ to $k'_{down} = 930 \pm 100 \text{ s}^{-1}$ (mean \pm SD, Fig. 4.5d)

Following the template photocycle for Arch,⁴⁵ we modeled a phenomenological photocycle for QuasAr6a as a continuous-time finite-state Markov chain (Fig. 4.5e).⁵⁰ Here, the M \rightarrow N transition is voltage sensitive, the N \rightarrow Q transition is photosensitive, and Q is the excitable fluorescent state. We modeled fluorescence as proportional to the Q-state population multiplied by field enhancement and fitted our data to models with varying transition rates and field enhancement. We found the best fit to the data, including enhanced brightness, decreased voltage sensitivity, and faster kinetics, for a model incorporating $k_3 = 437 \text{ s}^{-1}$ without plasmonic enhancement and $k_3 = 1133 \text{ s}^{-1}$ and $|\vec{E}|^2 / |\vec{E}^0|^2 = 1.30$ with plasmonic coupling (Fig. 4.5f, Fig. 4.S5, complete parameters and results available in Tables 4.S1-4.S2). Enhancement of only the quantum yield evidently does not explain the change in kinetics (Fig. 4.S5a), and enhancement of only k_3 leads to a worse fit of the data (Fig. 4.S5b). Based on this model, we interpret the increased fluorescence and response speed to voltage as caused by differential enhancement of absorption of the photon promoting the N \rightarrow Q transition and quantum yield of the Q-state fluorescence, tunable by the resonance spectrum of the plasmonic antenna.

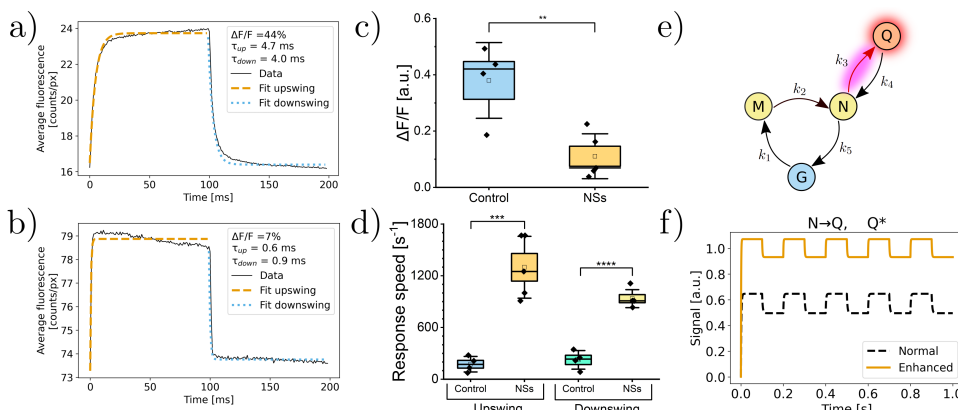


Figure 4.5: Plasmonic enhancement by gold nanostars manipulates the photocycle of QuasAr6a and causes enhanced brightness, diminished voltage sensitivity, and faster kinetics. **a,** Average trace of the median control cell under the influence of a square wave in membrane potential (-70 mV to $+30 \text{ mV}$). **b,** Like a, but in the presence of nanostars. **c,** Voltage sensitivity of QuasAr6a without (control) and with nanostars (NSs). Boxes represent the standard errors, whiskers the standard deviation, squares the means and mid-lines the medians. The mean sensitivity of the control is compatible with the value reported in the literature 0.43 ± 0.04 .⁴² The mean sensitivity decreases by 71% compared to the control. **d,** Response speed of QuasAr6a without (control) and with nanostars (NSs). Boxes represent the standard errors, whiskers the standard deviation, squares the means and mid-lines the medians. Both the upswing and the downswing transition become faster when the fluorophores are coupled with the nanostars. **e,** Proposed photocycle for QuasAr6a; fluorescence is thought to come from the Q-state, k_2 is voltage-dependent and k_3 is photoactivated. **f,** Numerically simulated traces for the apparent occupancy of the Q-state of QuasAr6a under the influence of a square wave in membrane potential (-70 mV to $+30 \text{ mV}$). Plasmonic enhancement is assumed to enhance k_3 and the quantum yield of the Q-state.

4.3. DISCUSSION

This study demonstrates the use of plasmonic enhancement to engineer the function of proteins in living cells, which has important implications for biosensing and functional bioimaging applications. We enhanced the fluorescence and voltage response speed of membrane-localized Archaeorhodopsin proteins. The emergence of these noticeable effects, even without precise control over the coupling distance, suggests a robust effect that could potentially be applied in animal models. Moreover, because plasmonic enhancement is a fast physical phenomenon lasting tens of femtoseconds,¹¹ it would be compatible with multiphoton excitation or other nonlinear imaging methods.

Archaerhodopsins are natural proton pumps;⁵¹ the QuasAr and Archon mutants have been created to break the proton pumping function so that these proteins can be used as GEVIs.^{23,24} These proteins have gone through years of protein engineering efforts to increase their functionality.^{23,45,24,44,33,42} Despite this, none of the evolved versions have succeeded in creating a sensor that responds to membrane voltage faster than the original Archaeorhodopsin3. The coupling to a plasmonic nanoantenna created a hybrid construct that enhanced the core function of the protein, its response to membrane voltage, to levels never achieved before by genetic manipulation, showing the promise of top-down control of protein function using plasmonics. Protein evolution of GEVIs often leads to increases in brightness at the expense of decreases in the speed of response to voltage changes.²⁶ Plasmonic enhancement shows a way to achieve both effects simultaneously. We hypothesize that a controlled trade-off between the enhancement of absorption (k_3) and emission (Y) can be used to fine-tune voltage sensitivity, speed, and brightness of GEVIs.

The applicability of this concept is enhanced by well-established methods to link (gold) nanoparticles to biomolecules,¹⁷ which would allow for even more precise control of distance and orientation of particles. The dense-star geometry shown in this work is also, in this combination, the critical shape for a plasmonic antenna, due to the robustness of its coupling against positional and orientational noise.

In conclusion, we showed the design and creation of gold nanostars for use as plasmonic antennas in live cell environments and achieved enhancement of protein function of mutated Archaeorhodopsin proteins. We enhanced fluorescence and response speed to voltage of QuasAr6a by tunable coupling to plasmonic nanostars in live cells. This work paves the way for applications of nanoantennas in bioengineering, particularly in engineering protein functionality, from light harvesting to sensing and top-down influencing of signaling cascades.

4.4. METHODS

4.4.1. FDTD SIMULATIONS

Finite-difference time-domain (FDTD) numerical simulations were conducted using Lumerical's FDTD Solutions, with scripts available on GitHub.⁵² Simulations of gold nanospheres involved varying the radius R of a gold sphere submerged in water, with a focus on assessing the maximum field enhancement $|E|^2/|E^0|^2$ within a small cubic volume ($\Delta x = \Delta y = \Delta z = R/2$) located 4 nm from the surface. Simulations covered a range of radii ($R_{\min} = 6$ nm to $R_{\max} = 76$ nm) with 2 nm steps.

Gold nanostar models were crafted based on SEM micrographs of synthesized nanoparticles. To generate these models, Blender software was employed to create complex meshes. The starting point for this modelling was an icosahedron shape, with its vertices extended to mimic the tip arrangement found on real nanostars. To ensure smoother surfaces, a Subdivision Surface Modifier was applied. During these simulations, a mesh size of 35 Meshes Per Radius (MPR) was consistently used. For benchmarking, a model nanostar with a core radius R of 25 nm and a tip length L_{tip} of 10 nm was adopted. For the simulations shown in **Figs. 4.1d** and **4.1e**, a core radius of 30 nm was used. Simulations explored variations in tip density and randomness to understand their implications for field enhancement. These variations included the random omission of tips and the random displacement of tip vertices, quantified using a "randomness factor" in Blender ranging from 0 to 1. Since the sharp tips simulated in **Figs. 4.1a**, **4.1c**, and **4.1d** generated unphysical fields when randomized in Blender, we introduced an adaptation to their sharpness to prevent unrealistic stretching and overly sharp edges. All scripts for Lumerical and Blender can be found on GitHub.⁵²

4

4.4.2. COLLOIDAL SYNTHESIS

In the presence of a high concentration of polyvinylpyrrolidone (PVP) dissolved in dimethyl-formamide (DMF), highly branched nanostars can be obtained efficiently at room temperature by optimizing the molar ratio $R=[\text{HAuCl}_4]/[\text{seeds}]$.²¹ Gold tips can grow on pre-formed gold seeds thanks to the reducing power of DMF and the excess of PVP. The protocol for making PVP-coated gold nanostars was adapted from the seed-mediated synthesis proposed by Barbosa et al.³¹ For each trial, 15 mL of 10 mM PVP (Sigma-Aldrich, PVP10) solubilized in DMF (Sigma-Aldrich, D4551) were transferred into a 25 mL conical flask under continuous magnetic stirring. Then, 82 μL of 50 mM HAuCl_4 aqueous solution were added. Within 30 s, a predetermined volume of gold spherical seeds (in-house synthesis based on Barbosa et al.,³¹ estimated concentration 0.5 mM, 15 nm in diameter) was added. The volume of pre-formed seeds was determined based on the formula $V_{\text{seed}} = \frac{[\text{HAuCl}_4] \cdot V_{\text{HAuCl}_4}}{[\text{seeds}] \cdot R} = \frac{8.2\text{mL}}{R}$, where R is the desired molar ratio. After 15 minutes under continuous stirring, the samples were spun at 4000 rpm for 90 minutes and the supernatant was removed to prevent the undesired formation of suboptimal nanoparticles. The nanostars were re-dispersed in MilliQ water and vortexed for a couple of seconds. This last purification step was carried out twice to minimize the cytotoxic effect of DMF and to reduce the amount of PVP in the solution. The optimal sample used throughout the manuscript corresponds to a molar ratio of 30 (273 μL of seeds).

4.4.3. UV/VISIBLE SPECTROSCOPY OF GOLD NANOSTARS COLLOID

The absorbance spectra were measured using a compact Visible-NIR light source (eco-VIS by Ocean Optics) together with a compact STS spectrometer (STS-VIS Microspectrometer, 350 – 800 nm, by Ocean Insight). Absorbance was measured using an integration time of 5.1 ms after background subtraction and intensity calibration, and averaged 1000 times.

4.4.4. MPTMS SURFACE COATING AND NANOPARTICLE IMMOBILIZATION

For the preparation of the MPTMS-coated dishes, a 10% MPTMS solution was prepared as follows: MPTMS (2.50 mL, Sigma-Aldrich, 175617) was combined with MilliQ water (2.50 mL), acetic acid (1.67 mL, Sigma-Aldrich, ARK2183), and pure ethanol (18.3 mL, Sigma-Aldrich, EMSURE 1.00983.1000). Prior to use, glass bottom dishes (Cellvis, D35-14-1.5-N) and fragments of silicon wafers were cleaned using oxygen plasma for 1 to 2 minutes, and all subsequent reactions were completed within a 30-minute timeframe. To prepare the substrates for cellular imaging, approximately 150 μ L of the MPTMS solution was gently dispensed into the recessed wells of the imaging dishes. These dishes were then carefully transferred to a large glass beaker and purged with nitrogen for 30 minutes (or until dry). Any residual MPTMS was aspirated. The dishes were subsequently subjected to a series of rinsing steps, including one wash with 150 μ L of pure ethanol in the recessed well, one wash with 2 mL of pure ethanol across the entire dish, and a final rinse with 2 mL of MilliQ water across the entire dish. To ensure dryness, the dishes were placed in a vacuum oven at 65°C for 2 hours. 200 μ L of gold nanostars were uniformly added to cover each recessed well. The dishes were then incubated overnight in a 37°C incubator, ensuring their cleanliness and contamination-free environment. Subsequently, the nanostar-coated substrates were aspirated, subjected to two 2 mL MilliQ water washes, and dried to near dryness. They were stored in the incubator until their intended use. For silicon substrates, the protocol remained unchanged, with volumes adjusted proportionally to the chip's surface area.

4.4.5. SEM/EDX CHARACTERIZATION

SEM imaging was performed in a Thermo Fisher Scientific (TFS) Nova 600i Nano Lab dual-beam system with a primary beam energy of 5 kV and nominal current of 0.27 nA using the SE-TLD detector. All imaging was performed at 5mm working distance and in immersion mode. Horizontal field of view and dwell time were varied and are specified on each reported image. EDX measurements were performed in the same Nova Nanolab dual-beam SEM using an Oxford Instruments X-MAX 80 EDX detector. The working distance was kept at 5 mm to have the optimum EDX signal. Spectra were analyzed using the Oxford Instruments AZtec software. The reported map EDX was obtained with a primary beam energy of 5 kV. Si and Au are mapped and reported in weight percentage (Wt%).

4.4.6. SEM IMAGE ANALYSIS

We aimed to isolate individual nanoparticles in SEM images to characterize them based on their core radius and tip length. Therefore, an algorithm was created using Python and OpenCV, available on GitHub.⁵² Firstly, the algorithm segmented the nanoparticles from the background using an Otsu adaptative threshold for bi-multimodal histograms. Secondly, an erosion was executed on the binary mask with 5 iterations and a 3×3 kernel to separate close nanoparticles. This way, we isolated the center of mass of the nanoparticles to iterate over the individual contours and generate individual masks for each nanoparticle; on the individual mask, we performed a symmetric dilatation to revert the previous erosion. Next, from the mask of the individual nanoparticles, we calculated the inner maximum radius to find the core size and the minimum enclosing circle to get the

total radius and the tip length. Finally, we extracted the pixel/meters conversion factor using the images' metadata for further analysis.

Aggregates that were still detected as single nanoparticles have been filtered post-analysis by applying the 2σ criterion on both radius and tip length.

4.4.7. FLUORESCENCE ASSAYS IN SOLUTION

Experiments in **Figs. 2, 3.f, 3.g, 4** and **5** were performed with nanostars grown in-house; experiments in **Figs. 3.b** and **3.d** were performed with commercially available nanostars.

Commercial gold nanostars (100 nm) as well as biotin-functionalized gold nanostars (100 nm), were obtained from Cytodiagnostics (Catalog number: GU-100-100). Notably, their absorption maxima are closely aligned with our in-house synthesized nanostars. The experiments were conducted using standard 96-well plates. 10 nM nanostars or biotin-functionalized nanostars, Streptavidin-Cy5 (10 μ M, ThermoFisher Scientific) were introduced into the respective sample groups. Each group was prepared with three replicates to ensure statistical robustness.

The 96-well plates, housing the nanostars and Streptavidin-Cy5 samples, were incubated at 37 °C for one hour to ensure complete binding between the components. Following this incubation, the fluorescence emissions were quantified and recorded with a Cary Eclipse Fluorescence Spectrophotometer (Agilent Technologies).

4.4.8. FLUORESCENCE SPECTROSCOPY ASSAYS ON SUBSTRATES

Glass coverslips underwent the MPTMS surface coating and nanoparticle immobilization, as indicated above. Approximately 60 μ L of this MPTMS solution was applied to the glass coverslips. The uniform layer of gold nanostars (AuNS) was deposited onto the substrates by adding 1 mL of AuNS solution to each recessed well.

The containers housing the glass slides were then sealed and placed on an orbital shaker (100 rpm) in a dark environment for an incubation period of 18 hours. On the following day, the AuNS-coated glass slides underwent three rinses with Milli-Q water, followed by gentle drying under a stream of nitrogen gas. To form monolayers of biotinylated bovine serum albumin (bBSA) on the substrates, 200 μ L of a 100 μ g/mL bBSA solution in PBS was applied to the substrate surfaces and allowed to incubate for 1 hour in a 37°C incubator. 40 μ L of a 10 μ M Streptavidin-Cy5 solution was added to the substrate surfaces and incubated for 2 hours in a 37 °C incubator. Following the incubation, the substrates were rinsed 3 times with PBS to eliminate any unbound fluorophores and gently dried using a nitrogen gas stream.

Fluorescence emission spectra of Streptavidin-Cy5 were measured using a photomultiplier tube (R7600U-20, Hamamatsu) coupled to a monochromator (SP2300, Princeton Instruments). Excitation light was provided by a xenon lamp connected to a monochromator (Gemini 180, HORIBA).

4.4.9. SUPPORTED LIPID BILAYER FORMATION

A glass slide covered by a silicone gasket with four 100 μ l wells was prepared with different MPTMS-immobilized nanostars and fibronectin conditions prior to the bilayer formation. The two Avanti Polar lipids (Birmingham, AL) used were 1,2-dioleoyl-sn-glycero-3-phosphocholine (DOPC) and 1,2-dioleoyl-sn-glycero-3-phosphocholine-N-(Cyanine

5) (DOPC-Cy5). Lipids in chloroform were mixed in a molar ratio of 99.5:0.5 DOPC:DOPC-Cy5 in a glass vial. The chloroform was evaporated with nitrogen and dried in a vacuum desiccator overnight. The dried lipid film was resuspended in PBS. The glass vial with the solution was then vortexed in bursts of 30 seconds with 1-minute intervals to resuspend all lipids and to stimulate the self-assembly of multilamellar vesicles. The solution was then sonicated in a high-capacity bath sonicator (10% amplitude, 10 s on, 10 s off, for one hour) to get a uniform size distribution of liposomes. 100 μ L of liposome solution was then deposited in each of the wells of the silicone gasket. The glass slides with liposomes were incubated for 30 min at room temperature to allow for supported lipid bilayer formation. All wells were washed four times with 200 μ L PBS after incubation.

4.4.10. TIRF MICROSCOPY

4

For the TIRF microscopy, an inverted microscope (Nikon Ti2-E, motorized) equipped with a 100 \times oil immersion objective (Nikon Apo TIRF 1.49 NA) and an Andor iXon Ultra 897 camera was used. The microscope was upgraded with an azimuthal TIRF/FRAP illumination module (GATACA systems iLAS 2). Samples were exited at 642 nm at 10% laser power (GATACA CW laser, 642 nm/110 mW). The emission was filtered with a 706/90 filter. Samples were exited for 200 ms for each frame, and a multiplication gain 50 was used. The penetration depth automatically estimated by the system is 106 nm.

4.4.11. HEK293T CULTURE

HEK293T cells (Catalog number ATCC® CRL-3216™) with passage number <30 were cultured in Dulbecco's Modified Eagle Medium (DMEM) supplemented with 10% Fetal Bovine Serum (VWR Seradigm Premium Grade), 50 units/mL Penicillin (Life Technologies), 50 μ g/mL Streptomycin (Life Technologies), and 1% GlutaMAX (Life Technologies) at 37 °C under 10% CO₂.

4.4.12. LENTIVIRUS PREPARATION AND TRANSDUCTION

For lentivirus production, HEK293T cells were seeded at 4·10⁶ cells per 100 mm polystyrene dish (Sarstedt) 1 day before transfection in order to achieve 80% confluence at the moment of transfection. Cells were co-transfected with 1.5 μ g transfer plasmid carrying either QuasAr1 or QuasAr6a, 5 μ g of pMDLg/RRE (Addgene plasmid #12251), 5 μ g of pRSV/Rev (Addgene plasmid #12253), and 3.5 μ g of pMD2.G (Addgene plasmid #12259) mixed in 400 μ L pre-warmed opti-MEM with 60 μ L polyethylenimine solution (1 μ g/ μ L in PBS). 8 hours post-transfection, medium was replaced with fresh cell culture medium including 25 mM HEPES. Lentivirus-containing supernatant was collected 48 and 72 hours post-transfection. Supernatant collected 48 hours post-transfection was stored overnight at 4 °C before pooling it with lentivirus collected 72 hours post-transfection. Supernatant was filtered through 0.22 μ m PVDF filters. Lentivirus was concentrated 15-fold using LentiX concentrator reagent (Takara), resuspended in PBS, and stored at -80 °C in 100 μ L aliquots. μ

For lentiviral transduction, 2.5·10⁵ cells were seeded per 35 mm polystyrene dish (Sarstedt) 1 day before transduction in order to achieve 50% confluence at the moment of transduction. Lentiviral aliquots were rapidly thawed in a 37 °C water bath. 100 μ L of concentrated virus was added per dish. Cells were incubated with lentivirus for 24 hours,

after which the media was replaced with fresh cell culture medium.

4.4.13. WIDEFIELD FLUORESCENCE MICROSCOPY

A custom-built⁵³ widefield microscope was employed to investigate the fluorescence of the QuasArs expressed in cells. Two continuous wave laser sources (MLL-FN-639 CNI and OBIS 488 LX, by Coherent) were made uniform in polarization and beam diameter through zero-order half-wave plates (WPH05M-488 and WPH05M-633 by Thorlabs), polarizers (CCM5-PBS201/M by Thorlabs) and individual collimators (AC254 mounted achromatic doublets by Thorlabs). The beams were then combined using a dichroic mirror (DMLP505 by Thorlabs) and led through an acousto-optic tunable filter (AOTFnC-VI S by AA Optoelectronics) with a modulation rate of 22 kHz. With the exception of the patch clamp voltage imaging experiments, the beam diameter was expanded with a telescope (AC254 mounted achromatic doublets by Thorlabs) using flip mounts (TRF90/M by Thorlabs). The light was reflected from a Digital Micromirror Device (DMD, Vialux V7001 by Texas Instruments) into a tube lens (TTL200 by Thorlabs) and projected by the objective (Olympus XLPLN25XWMP2, NA 1.05, working distance 2 mm) onto the sample. The emitted fluorescence was reflected by a dichroic mirror (Di03-R405/488/532/635-t3-32 × 44 by Semrock), collected using a tube lens (TTL200 by Thorlabs) and filtered further depending on the emission range (FF01560/94-25, FF01-582/64-25, LP02-664RU-25 and FF01-790/SP-25 by Semrock), before reaching the sCMOS camera (ORCA Flash4.0 V3, 2048 × 2048 pixels, 6.5 μ m pixel size by Hamamatsu) where the image was captured in a low-noise configuration with a total magnification of 27.8.

The maximum powers after the objective in the telescope configuration are 40 mW for the 639 nm laser and 2 mW for the 488 nm laser; without the telescope, the powers are 122 mW for the 639 nm laser and 5.2 mW for the 488 nm laser.

4.4.14. WHOLE-CELL PATCH-CLAMP RECORDINGS

Patch-clamp and imaging were performed 72 hours after lentiviral transduction. Transduced cells were seeded in the 14mm glass well of fibronectin-coated glass bottom dishes (Cellvis) at a density of 1.5·10⁴ cells per well 24 hours before the patch-clamp experiment. Before patch-clamp procedure, cells were washed gently three times with 2 mL of pre-warmed extracellular buffer (EC buffer). Cells were immersed in 2 mL of EC buffer throughout the patch clamp procedure. Constitution of EC buffer is 125 mM NaCl, 2.5 mM KCl, 3 mM CaCl₂, 1 mM MgCl₂, 15 mM HEPES, and 30 mM glucose.⁵⁴ pH of EC buffer is adjusted to 7.3 with NaOH. Osmolarity of EC buffer is adjusted to 300 mOsm with sucrose.

Borosilicate glass micropipettes were pulled from capillaries (Sutter Instrument) and filled with 10 μ L of intracellular medium (IC medium). Constitution of IC medium is 125 mM K-gluconate, 8 mM NaCl, 0.6 mM MgCl₂, 0.1 mM CaCl₂, 1 mM EGTA, 10 mM HEPES, 4 mM Mg-ATP and 0.4 mM Na-GTP, with pH adjusted to 7.3 with KOH.⁵⁵ Osmolarity of IC medium is adjusted to 295 mOsm with sucrose. Tip resistance was verified to be between 5 and 10 M Ω . Cellular responses were evoked through voltage steps ranging from -70 mV to +30 mV at a frequency of 5 Hz, while the fluorescence of QuasAr1 and QuasAr6a was excited at 639 nm. The camera frame rate in this setting is 1000 fps.

4.4.15. PHOTOCYCLE MODELLING AND SIMULATION

The photocycle of QuasAr6a has been modelled as a 4-state continuous-time Markov chain, where the putative biological macrostates corresponded directly to the mathematical states. Transitions were considered unidirectional. The Markov chain was expressed as a system of linear ODEs and solved numerically in Python using the LSODA solver (Livermore Solver for Ordinary Differential equations with Automatic method switching for stiff and non-stiff problems). The features of simulated traces (brightness enhancement, voltage sensitivities, response speeds) are compared to those of the measured traces and improved following a differential evolution algorithm. The software outputs the best parameters after a maximum of 1000 iterations, unless a plateau is reached earlier. To quantify the goodness of the fit in different conditions, we employed a Huber loss calculated on the fitted features compared to the one from the simulations. A lower loss indicates a better agreement between the simulations and the data. The fitted values for the models can be consulted in the Supplementary Information, while the code can be accessed on GitHub.⁵²

4.5. SUPPLEMENTARY INFORMATION

4.5.1. INDIVIDUAL SIMULATIONS REALISTIC NANOSTARS

Here reported are the individual simulation results, which were then aggregated in **Fig. 4.1d** and **4.1e**.

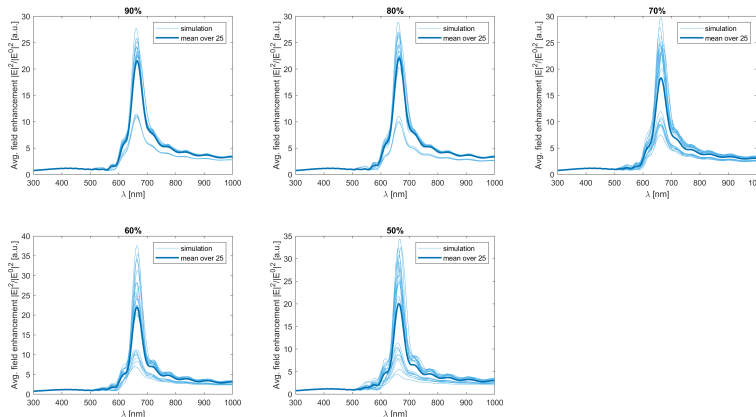
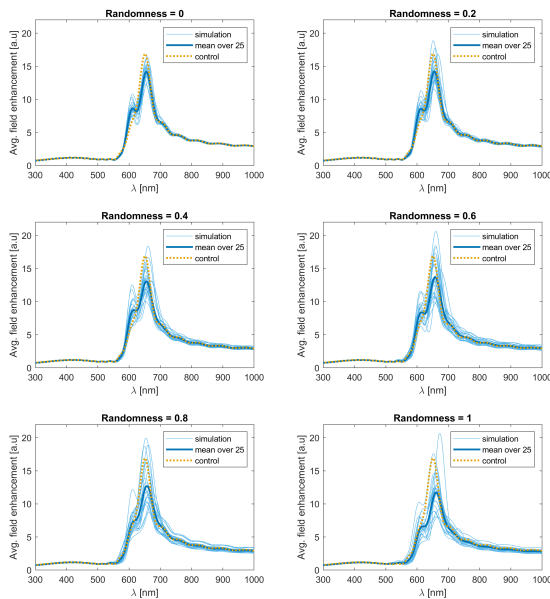


Figure 4.S1: Individual simulation results at different tip lengths. The results are aggregated in **Fig. 4.1d**.



4

Figure 4.S2: Individual simulation results at different randomness factors. The results are aggregated in **Fig. 4.1e**. The control corresponds to an ideal nanostar, optimally aligned with the field monitor.

4.5.2. ENERGY-DISPERSIVE X-RAY SPECTROSCOPY

Energy-dispersive X-ray (EDX) spectroscopy performed on the synthesized samples substantiated the purity of the gold nanostars (**Fig. 4.S3**).

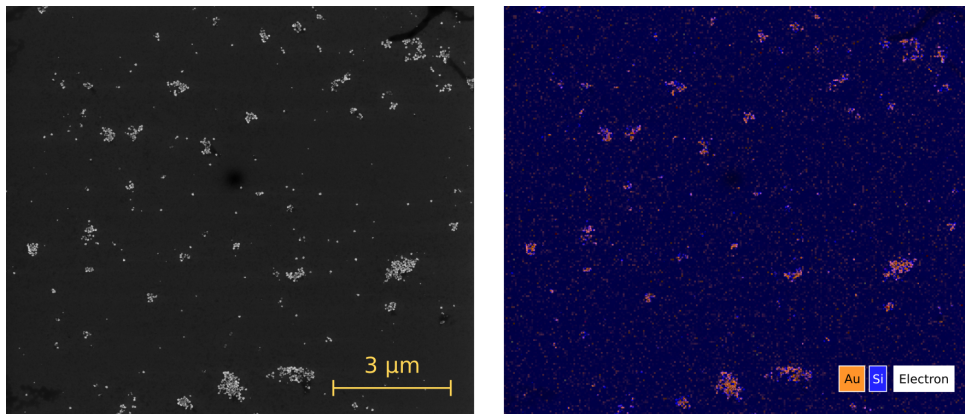


Figure 4.S3: Validation of the purity of gold nanostar samples, showing the absence of any residual gold in the specimen. On the left, the SEM micrograph of a nanostar sample bound to glass via MPTMS; on the right, the same field of view under EDX inspection.

4.5.3. FRÖHLICH-LIKE SHIFT DUE TO PVP COATING

The local dielectric environment has an effect on the plasmonic resonance frequency. To estimate this in the case of PVP-capped nanoparticles, let us assume that the red-shift due to the capping agent is Fröhlich-like:³⁰

$$\lambda_{PVP} = \frac{2\pi c \sqrt{\epsilon_{m,\infty} + 2\epsilon_{PVP}}}{\omega_p} \quad (S.1)$$

where λ_{PVP} is the resonance wavelength when considering the PVP as a capping agent, c the speed of light, $\epsilon_{m,\infty}$ the core polarization of gold, ϵ_{PVP} the dielectric constant of PVP and ω_p the plasma frequency of gold.

If the nanostars would be "bare", or simply said immersed in water without any capping agent, the resonance wavelength would be:

$$\lambda_{H_2O} = \frac{2\pi c \sqrt{\epsilon_{m,\infty} + 2\epsilon_{H_2O}}}{\omega_p} \quad (S.2)$$

We can then rewrite λ_{H_2O} in terms of λ_{PVP} :

$$\lambda_{H_2O} = \lambda_{PVP} \frac{\sqrt{\epsilon_{m,\infty} + 2\epsilon_{H_2O}}}{\sqrt{\epsilon_{m,\infty} + 2\epsilon_{PVP}}} \quad (S.3)$$

The plasmonic peak of nanostars coated in PVP is measured experimentally to be at 740nm. For gold $\epsilon_{m,\infty} = 7.9$,⁵⁶ for water $\epsilon_{H_2O} = 1.77$ ⁵⁷ and for PVP $\epsilon_{PVP} = 2.33$.⁵⁸

Plugging these values in Eq. (S.3) yields $\lambda_{H_2O} = 706$ nm, which aligns almost perfectly with the position of the peak of Archon¹³³ and could potentially correspond to the condition where the nanostars are immobilized on the glass substrates.

4.5.4. ESTIMATION OF THE QUANTUM YIELD ENHANCEMENT OF CY5

To estimate quantitatively the fluorescence enhancement of Cy5 when bound to a nanostar via bBSA (Fig. 3c of the main manuscript), we calculated the average field enhancement in a ring at 13 nm from the surface to better represent a realistic effect (ring thickness 1 nm, 13 nm away from the surface).

The average value in the ring is 1.78 (Fig. 4.S4). Then, from a reference³⁵ we took $Y = 0.30$ and $\tau = 2.33$ ns and calculated:

$$\Gamma = \frac{Y}{\tau} = 0.129 \text{ ns}^{-1} \quad (S.4)$$

$$\Gamma_{nr} = \frac{1 - Y}{\tau} = 0.300 \text{ ns}^{-1} \quad (S.5)$$

Given that the main effect is the enhancement of the radiative decay rate Γ , we can calculate the enhanced quantum yield using Eq. (1) (main manuscript):

$$Y_{enh} = \frac{\frac{|E|^2}{|E^0|^2} \cdot \Gamma}{\frac{|E|^2}{|E^0|^2} \cdot \Gamma + \Gamma_{nr}} = \frac{1.78 \cdot \Gamma}{1.78 \cdot \Gamma + \Gamma_{nr}} = 0.434 \quad (S.6)$$

the relative increase in the quantum yield is 45%, exactly what we measured.

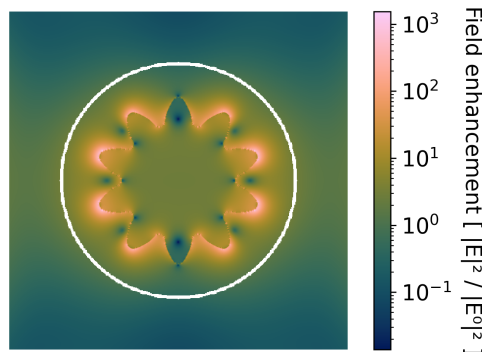


Figure 4.S4: In white, the anular region around the nanostar where the field enhancement is averaged. Ring thickness 1 nm.

4

4.5.5. ESTIMATION OF THE GLYCOCALYX SPACING EFFECT

Using the plasmonic ruler as calculated in the main manuscript, we can estimate the spacing due to the glycocalyx by comparing the field enhancement above and below the HEK cells. We use the quantum yield of Q6a $Y = 0.0367$.⁴²

We know that:

$$Y = \frac{\Gamma}{\Gamma + \Gamma_{nr}} \Rightarrow \Gamma = \frac{Y}{1 - Y} \Gamma_{nr} \quad (S.7)$$

and from our experiments:

$$Y_{below} = 1.69Y = 0.062 \quad (S.8)$$

$$Y_{above} = 1.28Y = 0.047 \quad (S.9)$$

The enhanced quantum yield due to field enhancement α is:

$$Y^* = \frac{\alpha\Gamma}{\alpha\Gamma + \Gamma_{nr}} = \frac{\alpha Y}{\alpha Y + (1 - Y)} \quad (S.10)$$

Therefore we can express the field enhancement as:

$$\alpha = \frac{Y^*}{1 - Y^*} \cdot \frac{1 - Y}{Y} \quad (S.11)$$

For the case of nanostars embedded in the fibronectin coating, we get:

$$\alpha_{below} = 1.73 \quad (S.12)$$

which corresponds, according to the plasmonic ruler, to 13.5 nm. For the case of nanostars dropped above the cells, we get:

$$\alpha_{above} = 1.29 \quad (S.13)$$

which corresponds, according to the plasmonic ruler, to 16 nm. Knowing that the fibronectin is 6 nm thick (Fig. 2), the thickness of the glycocalyx can be estimated to be:

$$\Delta d = (16 - (13.5 - 6)) \text{ nm} = 8.5 \text{ nm} \quad (S.14)$$

4.5.6. PHOTOCYCLE FITTING

The quantum yield of the fluorescent state is:

$$Y = \frac{\Gamma}{\Gamma + \Gamma_{nr}} \quad (S.15)$$

The enhanced quantum yield due to field enhancement α is:

$$Y^* = \frac{\alpha\Gamma}{\alpha\Gamma + \Gamma_{nr}} \approx \alpha Y \quad (S.16)$$

The approximation is valid for small Γ/Γ_{nr} . The measured fluorescence is the product of some efficiency factor (system dependent) η , the occupancy of state Q and the quantum yield Y :

$$F = \eta Q Y \quad (S.17)$$

$$F^* = \eta Q^* Y^* = \eta Q^* \alpha Y \quad (S.18)$$

Brightness enhancement:

$$\frac{F_l^* - F_l}{F_l} = \frac{\eta Q_l^* \alpha Y - \eta Q_l Y}{\eta Q_l Y} = \alpha \frac{Q_l^*}{Q_l} - 1 \quad (S.19)$$

Voltage sensitivity (control):

$$\frac{F_h - F_l}{F_l} = \frac{\eta Q_h Y - \eta Q_l Y}{\eta Q_l Y} = \frac{Q_h}{Q_l} - 1 \quad (S.20)$$

Voltage sensitivity (enhanced):

$$\frac{F_h^* - F_l^*}{F_l^*} = \frac{\eta Q_h^* \alpha Y - \eta Q_l^* \alpha Y}{\eta Q_l^* \alpha Y} = \frac{Q_h^*}{Q_l^*} - 1 \quad (S.21)$$

These quantities so defined can be used to directly compare the features between measurements (where F is known, but not the photocycle state population Q) and the simulations (where Q is known, but not the quantum yield Y or the efficiency factor η).

By implementing these criteria in a differential evolution algorithm (code available on GitHub⁵²), we obtained a set of parameters and results for each case (Table 4.S1 and 4.S2, simulated traces in Fig. 4.S5). Note that the measured time constant of the enhanced response was likely limited by the camera response time, rather than the protein kinetics.

Parameter		Q*	N → Q	N → Q, Q*
k_1 [s ⁻¹]		68238	67584	68432
$k_2 = k_{2m}V + k_{2q}$	k_{2m} [V ⁻¹ s ⁻¹]	3826	244031	294902
	k_{2q} [s ⁻¹]	2146	29905	27264
k_3 [s ⁻¹]	Control	110	212	437
	Enhanced	110	425	1133
k_4 [s ⁻¹]		310	224	169
k_5 [s ⁻¹]		9443	9691	9897
$ \vec{E} ^2 / \vec{E}^0 ^2$ [a.u.]		1.69	1	1.30

Table 4.S1: Best parameters from genetic algorithm fitting of the experimental data.

Output		Observed results	Q*	N → Q	N → Q, Q*
Brightness Enhancement [a.u.]		0.69	0.69	0.50	0.88
$\frac{\Delta F}{F}$ [a.u.]	Control	0.38	0.15	0.21	0.31
	Enhanced	0.11	0.15	0.15	0.15
k_{up} [s ⁻¹]	Control	170	320	369	471
	Enhanced	1300	320	524	952
k_{down} [s ⁻¹]	Control	220	331	329	327
	Enhanced	930	331	443	570
Huber loss [a.u.]			12.9	10.9	8.5

Table 4.S2: Comparison of the features and quantification of the Huber loss for experimental and simulated conditions.

4

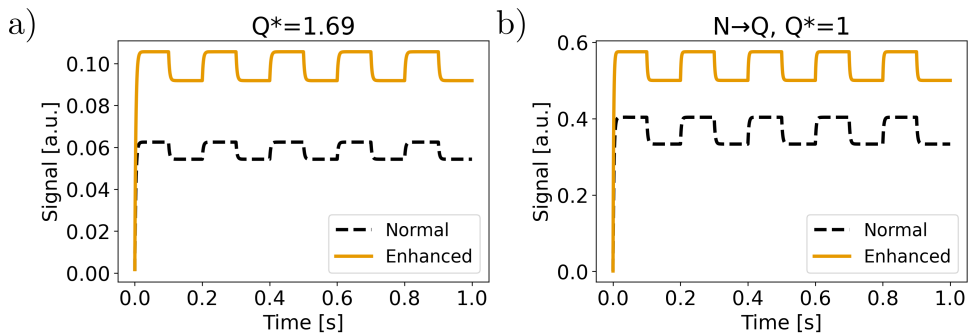


Figure 4.S5: Numerically simulated traces for the apparent occupancy of the Q-state of QuasAr6a under the influence of a square wave in membrane potential (-70 mV to $+30$ mV). **a**, Plasmonic enhancement is assumed to enhance the Q-state only. **b**, Plasmonic enhancement is assumed to enhance k_3 only.

BIBLIOGRAPHY

- [1] Pascal Anger, Palash Bharadwaj, and Lukas Novotny. "Enhancement and quenching of single-molecule fluorescence". In: *Physical Review Letters* 96.11 (2006). ISSN: 00319007. DOI: [10.1103/PhysRevLett.96.113002](https://doi.org/10.1103/PhysRevLett.96.113002).
- [2] Bart De Nijs et al. "Plasmonic tunnel junctions for single-molecule redox chemistry". In: *Nature Communications* 8.1 (2017). ISSN: 20411723. DOI: [10.1038/s41467-017-00819-7](https://doi.org/10.1038/s41467-017-00819-7).
- [3] Lin Yuan et al. "Sustainable chemistry with plasmonic photocatalysts". In: *Nanophotonics* 12.14 (2023). ISSN: 21928614. DOI: [10.1515/nanoph-2023-0149](https://doi.org/10.1515/nanoph-2023-0149).
- [4] Sergei Kühn et al. "Enhancement of single-molecule fluorescence using a gold nanoparticle as an optical nanoantenna". In: *Physical Review Letters* 97.1 (2006). ISSN: 00319007. DOI: [10.1103/PhysRevLett.97.017402](https://doi.org/10.1103/PhysRevLett.97.017402).
- [5] Martin Aeschlimann et al. "Adaptive subwavelength control of nano-optical fields". In: *Nature* 446.7133 (2007). ISSN: 14764687. DOI: [10.1038/nature05595](https://doi.org/10.1038/nature05595).
- [6] Janina Kneipp, Harald Kneipp, and Katrin Kneipp. "SERS—a single-molecule and nanoscale tool for bioanalytics". In: *Chemical Society Reviews* 37.5 (2008). ISSN: 14604744. DOI: [10.1039/b708459p](https://doi.org/10.1039/b708459p).
- [7] Lukas Novotny and Bert Hecht. "Optical antenna probes". In: *Principles of Nano-Optics*. 2nd. 2009. Chap. 6.5, pp. 188–192. DOI: [10.1017/CBO9780511794193](https://doi.org/10.1017/CBO9780511794193).
- [8] M. A. Noginov et al. "Demonstration of a spaser-based nanolaser". In: *Nature* 460.7259 (2009). ISSN: 00280836. DOI: [10.1038/nature08318](https://doi.org/10.1038/nature08318).
- [9] Anika Kinkhabwala et al. "Large single-molecule fluorescence enhancements produced by a bowtie nanoantenna". In: *Nature Photonics* 3.11 (2009). ISSN: 17494885. DOI: [10.1038/nphoton.2009.187](https://doi.org/10.1038/nphoton.2009.187).
- [10] Alberto G. Curto et al. "Unidirectional emission of a quantum dot coupled to a nanoantenna". In: *Science* 329.5994 (2010). ISSN: 00368075. DOI: [10.1126/science.1191922](https://doi.org/10.1126/science.1191922).
- [11] Daan Brinks et al. "Plasmonic antennas as design elements for coherent ultrafast nanophotonics". In: *Proceedings of the National Academy of Sciences of the United States of America* 110.46 (2013). ISSN: 00278424. DOI: [10.1073/pnas.1308652110](https://doi.org/10.1073/pnas.1308652110).
- [12] Janina Kneipp et al. "In vivo molecular probing of cellular compartments with gold nanoparticles and nanoaggregates". In: *Nano Letters* 6.10 (2006). ISSN: 15306984. DOI: [10.1021/nl061517x](https://doi.org/10.1021/nl061517x).
- [13] Fareeha Safir et al. "Combining Acoustic Bioprinting with AI-Assisted Raman Spectroscopy for High-Throughput Identification of Bacteria in Blood". In: *Nano Letters* 23.6 (2023). ISSN: 15306992. DOI: [10.1021/acs.nanolett.2c03015](https://doi.org/10.1021/acs.nanolett.2c03015).

- 4**
- [14] Yirui Zhang et al. "From Genotype to Phenotype: Raman Spectroscopy and Machine Learning for Label-Free Single-Cell Analysis". In: *ACS Nano* 18.28 (2024), pp. 18101–18117. DOI: [10.1021/acsnano.4c04282](https://doi.org/10.1021/acsnano.4c04282). URL: <https://doi.org/10.1021/acsnano.4c04282>.
 - [15] Mario Hentschel et al. "Dielectric Mie voids: confining light in air". In: *Light: Science and Applications* 12.1 (2023). ISSN: 20477538. DOI: [10.1038/s41377-022-01015-z](https://doi.org/10.1038/s41377-022-01015-z).
 - [16] Xiaohua Huang et al. "Cancer cell imaging and photothermal therapy in the near-infrared region by using gold nanorods". In: *Journal of the American Chemical Society* 128.6 (2006). ISSN: 00027863. DOI: [10.1021/ja057254a](https://doi.org/10.1021/ja057254a).
 - [17] Leming Sun et al. "Smart nanoparticles for cancer therapy". In: *Signal Transduction and Targeted Therapy* 8.1 (2023). ISSN: 20593635. DOI: [10.1038/s41392-023-01642-x](https://doi.org/10.1038/s41392-023-01642-x).
 - [18] Ioannis G. Theodorou et al. "Towards multiplexed near-infrared cellular imaging using gold nanostar arrays with tunable fluorescence enhancement". In: *Nanoscale* 11.4 (2019). ISSN: 20403372. DOI: [10.1039/c8nr09409h](https://doi.org/10.1039/c8nr09409h).
 - [19] Mahima Unnikrishnan et al. "Nanoparticle-assisted tubulin assembly is environment dependent". In: *Proceedings of the National Academy of Sciences* 121.28 (2024), e2403034121. DOI: [10.1073/pnas.2403034121](https://doi.org/10.1073/pnas.2403034121). URL: <https://www.pnas.org/doi/abs/10.1073/pnas.2403034121>.
 - [20] Bing Fu et al. "Super-Resolving the Distance-Dependent Plasmon-Enhanced Fluorescence of Single Dye and Fluorescent Protein Molecules". In: *Journal of Physical Chemistry C* 119.33 (2015). ISSN: 19327455. DOI: [10.1021/acs.jpcc.5b05154](https://doi.org/10.1021/acs.jpcc.5b05154).
 - [21] Andrés Guerrero-Martínez et al. "Nanostars shine bright for you. Colloidal synthesis, properties and applications of branched metallic nanoparticles". In: *Current Opinion in Colloid and Interface Science* 16.2 (2011). ISSN: 13590294. DOI: [10.1016/j.cocis.2010.12.007](https://doi.org/10.1016/j.cocis.2010.12.007).
 - [22] Chris D. Geddes and Joseph R. Lakowicz. "Metal-Enhanced Fluorescence". In: *Journal of Fluorescence*. Vol. 12. 2. 2002. DOI: [10.1023/A:1016875709579](https://doi.org/10.1023/A:1016875709579).
 - [23] Joel M. Kralj et al. "Optical recording of action potentials in mammalian neurons using a microbial rhodopsin". In: *Nature Methods* 9.1 (2012). ISSN: 15487091. DOI: [10.1038/nmeth.1782](https://doi.org/10.1038/nmeth.1782).
 - [24] Daniel R. Hochbaum et al. "All-optical electrophysiology in mammalian neurons using engineered microbial rhodopsins". In: *Nature Methods* 11.8 (2014). ISSN: 15487105. DOI: [10.1038/NMETH.3000](https://doi.org/10.1038/NMETH.3000).
 - [25] Willem J de Grip and Srividya Ganapathy. "Rhodopsins: An Excitingly Versatile Protein Species for Research, Development and Creative Engineering". In: *Frontiers in Chemistry* 10 (2022). ISSN: 2296-2646. DOI: [10.3389/fchem.2022.879609](https://doi.org/10.3389/fchem.2022.879609). URL: <https://www.frontiersin.org/articles/10.3389/fchem.2022.879609>.

- [26] Xin Meng et al. "Voltage Imaging with Engineered Proton-Pumping Rhodopsins: Insights from the Proton Transfer Pathway". In: *ACS Physical Chemistry Au* 3.4 (2023). ISSN: 26942445. DOI: [10.1021/acspyschemau.3c00003](https://doi.org/10.1021/acspyschemau.3c00003).
- [27] Jessica E. Donehue et al. "Plasmon-Enhanced brightness and photostability from single fluorescent proteins coupled to gold nanorods". In: *Journal of Physical Chemistry C* 118.27 (2014). ISSN: 19327455. DOI: [10.1021/jp504186n](https://doi.org/10.1021/jp504186n).
- [28] Aleksandr Barulin et al. "Deep Ultraviolet Plasmonic Enhancement of Single Protein Autofluorescence in Zero-Mode Waveguides". In: *Nano Letters* 19.10 (2019). ISSN: 15306992. DOI: [10.1021/acs.nanolett.9b03137](https://doi.org/10.1021/acs.nanolett.9b03137).
- [29] Stephen A. Lee and Julie S. Biteen. "Interplay of Nanoparticle Resonance Frequency and Array Surface Coverage in Live-Cell Plasmon-Enhanced Single-Molecule Imaging". In: *Journal of Physical Chemistry C* 122.10 (2018). ISSN: 19327455. DOI: [10.1021/acs.jpcc.8b01436](https://doi.org/10.1021/acs.jpcc.8b01436).
- [30] Marco Locarno and Daan Brinks. "Analytical calculation of plasmonic resonances in metal nanoparticles: A simple guide". In: *American Journal of Physics* 91.7 (July 2023), p. 538. ISSN: 0002-9505. DOI: [10.1119/5.0094967](https://doi.org/10.1119/5.0094967). URL: <https://doi.org/10.1119/5.0094967>.
- [31] Silvia Barbosa et al. "Tuning size and sensing properties in colloidal gold nanostars". In: *Langmuir* 26.18 (2010). ISSN: 07437463. DOI: [10.1021/la102559e](https://doi.org/10.1021/la102559e).
- [32] Ravi Shukla et al. "Biocompatibility of gold nanoparticles and their endocytotic fate inside the cellular compartment: A microscopic overview". In: *Langmuir* 21.23 (2005). ISSN: 07437463. DOI: [10.1021/la0513712](https://doi.org/10.1021/la0513712).
- [33] Arita Silapetere et al. "QuasAr Odyssey: the origin of fluorescence and its voltage sensitivity in microbial rhodopsins". In: *Nature Communications* 13.1 (2022), p. 5501. ISSN: 2041-1723. DOI: [10.1038/s41467-022-33084-4](https://doi.org/10.1038/s41467-022-33084-4). URL: <https://doi.org/10.1038/s41467-022-33084-4>.
- [34] Ondrej Stranik et al. "Plasmonic enhancement of fluorescence for sensor applications". In: *Sensors and Actuators, B: Chemical*. Vol. 107. 1 SPEC. ISS. 2005. DOI: [10.1016/j.snb.2004.08.032](https://doi.org/10.1016/j.snb.2004.08.032).
- [35] Yi Fu, Jian Zhang, and Joseph R. Lakowicz. "Plasmonic enhancement of single-molecule fluorescence near a silver nanoparticle". In: *Journal of Fluorescence* 17.6 (2007). ISSN: 10530509. DOI: [10.1007/s10895-007-0259-0](https://doi.org/10.1007/s10895-007-0259-0).
- [36] Nyssa T. Emerson and Haw Yang. "Reproducibly Measuring Plasmon-Enhanced Fluorescence in Bulk Solution across a 20-Fold Range of Optical Densities". In: *Analytical Chemistry* 93.22 (2021). ISSN: 15206882. DOI: [10.1021/acs.analchem.1c01210](https://doi.org/10.1021/acs.analchem.1c01210).
- [37] Camillo Rosano, Paolo Arosio, and Martino Bolognesi. "The X-ray three-dimensional structure of avidin". In: *Biomolecular Engineering* 16.1-4 (1999). ISSN: 13890344. DOI: [10.1016/S1050-3862\(99\)00047-9](https://doi.org/10.1016/S1050-3862(99)00047-9).
- [38] Scott H. Brewer et al. "Probing BSA binding to citrate-coated gold nanoparticles and surfaces". In: *Langmuir* 21.20 (2005). ISSN: 07437463. DOI: [10.1021/la050588t](https://doi.org/10.1021/la050588t).

- 4**
- [39] B. Jachimska and A. Pajor. "Physico-chemical characterization of bovine serum albumin in solution and as deposited on surfaces". In: *Bioelectrochemistry* 87 (2012). ISSN: 15675394. DOI: [10.1016/j.bioelechem.2011.09.004](https://doi.org/10.1016/j.bioelechem.2011.09.004).
 - [40] Nico Strohmeyer et al. "Fibronectin-bound $\alpha 5\beta 1$ integrins sense load and signal to reinforce adhesion in less than a second". In: *Nature Materials* 16.12 (2017). ISSN: 14764660. DOI: [10.1038/nmat5023](https://doi.org/10.1038/nmat5023).
 - [41] Yoav Adam et al. "Voltage imaging and optogenetics reveal behaviour-dependent changes in hippocampal dynamics". In: *Nature* 569.7756 (2019). ISSN: 14764687. DOI: [10.1038/s41586-019-1166-7](https://doi.org/10.1038/s41586-019-1166-7).
 - [42] He Tian et al. "Video-based pooled screening yields improved far-red genetically encoded voltage indicators". In: *Nature Methods* (2023). ISSN: 1548-7105. DOI: [10.1038/s41592-022-01743-5](https://doi.org/10.1038/s41592-022-01743-5). URL: <https://doi.org/10.1038/s41592-022-01743-5>.
 - [43] Kiryl D. Piatkevich et al. "A robotic multidimensional directed evolution approach applied to fluorescent voltage reporters article". In: *Nature Chemical Biology* 14.4 (2018). ISSN: 15524469. DOI: [10.1038/s41589-018-0004-9](https://doi.org/10.1038/s41589-018-0004-9).
 - [44] Miao Ping Chien et al. "Photoactivated voltage imaging in tissue with an archaerhodopsin-derived reporter". In: *Science Advances* 7.19 (2021). ISSN: 23752548. DOI: [10.1126/sciadv.abe3216](https://doi.org/10.1126/sciadv.abe3216).
 - [45] Dougal Maclaurin et al. "Mechanism of voltage-sensitive fluorescence in a microbial rhodopsin". In: *Proceedings of the National Academy of Sciences of the United States of America* 110.15 (2013). ISSN: 00278424. DOI: [10.1073/pnas.1215595110](https://doi.org/10.1073/pnas.1215595110).
 - [46] Carolyn R. Shurer et al. "Physical Principles of Membrane Shape Regulation by the Glycocalyx". In: *Cell* 177.7 (2019). ISSN: 10974172. DOI: [10.1016/j.cell.2019.04.017](https://doi.org/10.1016/j.cell.2019.04.017).
 - [47] Leonhard Möckl et al. "Quantitative Super-Resolution Microscopy of the Mammalian Glycocalyx". In: *Developmental Cell* 50.1 (2019). ISSN: 18781551. DOI: [10.1016/j.devcel.2019.04.035](https://doi.org/10.1016/j.devcel.2019.04.035).
 - [48] Matthew J. Paszek et al. "Integrin clustering is driven by mechanical resistance from the glycocalyx and the substrate". In: *PLoS Computational Biology* 5.12 (2009). ISSN: 15537358. DOI: [10.1371/journal.pcbi.1000604](https://doi.org/10.1371/journal.pcbi.1000604).
 - [49] Gaoxiang Mei et al. "Analog Retinal Redshifts Visible Absorption of QuasAr Transmembrane Voltage Sensors into Near-infrared". In: *Photochemistry and Photobiology* 96.1 (2020). ISSN: 17511097. DOI: [10.1111/php.13169](https://doi.org/10.1111/php.13169).
 - [50] Daniel Wüstner et al. "Photobleaching kinetics and time-integrated emission of fluorescent probes in cellular membranes". In: *Molecules* 19.8 (2014). ISSN: 14203049. DOI: [10.3390/molecules190811096](https://doi.org/10.3390/molecules190811096).
 - [51] Yasuo Mukohata et al. "An Australian halobacterium contains a novel proton pump retinal protein: Archaeorhodopsin". In: *Biochemical and Biophysical Research Communications* 151.3 (1988). ISSN: 10902104. DOI: [10.1016/S0006-291X\(88\)80509-6](https://doi.org/10.1016/S0006-291X(88)80509-6).

- [52] *GitHub repository*. URL: <https://github.com/Brinkslab/FDTD-Plasmonics/>.
- [53] Xin Meng et al. “A compact microscope for voltage imaging”. In: *Journal of Optics (United Kingdom)* 24.5 (2022). ISSN: 20408986. DOI: [10.1088/2040-8986/ac5dd5](https://doi.org/10.1088/2040-8986/ac5dd5).
- [54] Zheng Shi et al. “Cell Membranes Resist Flow”. In: *Cell* 175.7 (2018). ISSN: 10974172. DOI: [10.1016/j.cell.2018.09.054](https://doi.org/10.1016/j.cell.2018.09.054).
- [55] Xue Han et al. “A high-light sensitivity optical neural silencer: Development and application to optogenetic control of non-human primate cortex”. In: *Frontiers in Systems Neuroscience* APRIL 2011 (2011). ISSN: 16625137. DOI: [10.3389/fnsys.2011.00018](https://doi.org/10.3389/fnsys.2011.00018).
- [56] David R. Lide. “Optical Properties of Selected Elements”. In: *CRC Handbook of Chemistry and Physics*. 6th. CRC Press (Internet version), 2005. ISBN: 978- 0849332043.
- [57] George M. Hale and Marvin R. Querry. “Optical Constants of Water in the 200-nm to 200- μ m Wavelength Region”. In: *Applied Optics* 12.3 (1973). ISSN: 0003-6935. DOI: [10.1364/ao.12.000555](https://doi.org/10.1364/ao.12.000555).
- [58] Tobias A.F König et al. “Electrically tunable plasmonic behavior of nanocube-polymer nanomaterials induced by a redox-active electrochromic polymer”. In: *ACS Nano* 8.6 (2014). ISSN: 1936086X. DOI: [10.1021/nn501601e](https://doi.org/10.1021/nn501601e).

5

DEGENERATE PUMP-PROBE NON-LINEAR EXCITATION OF QUASAR6A

Building on the plasmonic enhancement strategies detailed in the previous chapters, this chapter explores the ultrafast dynamics of QuasAr6a via degenerate pump–probe excitation. While Chapter 4 demonstrated that steady-state plasmonic enhancement can modify QuasAr6a’s fluorescence efficiency and response kinetics, here we investigate whether ultrafast excitation can modulate its photocycle transitions. By applying femtosecond pulse shaping, we aimed to selectively control excitation pathways and uncover new mechanisms of non-linear response in QuasArs with sub-picosecond time resolution. Specifically, our approach targets the delicate balance between the transient intermediate states of the photocycle. Tailoring the delay of the pulses could enable us to enhance or suppress particular transitions, effectively “steering” the protein’s dynamic response and, ultimately, its function.

5.1. INTRODUCTION

Ultrafast pump–probe spectroscopy has emerged as a powerful technique to investigate coherent and non-linear processes in chemical and biological molecules.¹ By generating pairs of pulses, it becomes possible to interrogate the temporal evolution of electronic and vibrational states with great precision.^{1,2} In this context, we say that the excitation is “degenerate” when the pump and probe pulses have the same frequency and phase, implying that the pump and probe pulses are phase-locked and identical in terms of energy characteristics.³

A large body of research has been conducted in the “weak-field” or perturbative regime, where the response to the absorption of single photons is studied.⁴ In recent years, this method has been successfully applied to single molecules, revealing details about electronic dephasing and vibrational wave-packet dynamics that are otherwise

masked in ensemble measurements.^{5,6} Additionally, theoretical analyses have provided a solid foundation for interpreting the characteristic signatures observed in these experiments.⁷ At higher laser peak powers we hit the "strong-field" regime instead, where complex molecules usually exhibit multi-photon interactions.^{1,8,9} Many non-linear effects emerge in this regime, enabling selective control over reaction pathways.⁸

The degenerate pump–probe technique is particularly well suited for investigating the non-linear response of Archaeerhodopsins under conditions where conventional 1-photon excitation fails to capture the complexity of its photocycle. In fact, proteins in this family that exhibit high efficiency in 1-photon excitation often do not perform similarly well under 2-photon excitation and vice versa, contrary to what might be intuitively expected.^{10,11} This discrepancy suggests that the fundamental mechanisms driving these processes are not fully understood.¹² Understanding these mechanisms could enable the optimization of excitation strategies, therefore enhancing fluorescence emission without the need for further protein engineering.

In this context, the simultaneous interaction of two identical pulses would allow for the separation of the linear and non-linear contributions, and the controlled manipulation of coherent superposition states, even at room temperature.¹³ This precious information is necessary to understand how minimal modifications in pulse delay and phase can influence the energy landscape of the protein, and consequently affecting its overall performance.¹⁴ Inspired by advances in coherent pulse control, where phase-locked femtosecond pump and probe pulses were used to induce and manipulate oscillations in single molecules at room temperature,^{11,15} we propose to investigate the response of QuasAr6a under degenerate pump-probe non-linear excitation.

In this chapter, we investigate the principles of non-linear behavior resulting from the initial transition in the photocycle of QuasAr6a. We designed an optical delay line capable of splitting a pulsed 2-photon beam into two identical beams, allowing us to precisely control the delay between the pulses within a range of 0 fs to 1.13 ns, with an incremental step size of 0.67 fs. The system was calibrated to measure the pulse width and assess possible spatial effects. With this setup we performed excitation experiments on QuasAr6a at various delays, aiming to measure the response of the protein under these controlled conditions.

Although the results presented in this chapter are preliminary, they mark a significant step forward in the pump-probe investigation of the photocycle in Archaeerhodopsins, in particular QuasAr6a. These findings provide a preliminary platform to inform future studies and contribute to the broader goal of optimizing non-linear excitation techniques for enhanced fluorescence emission.

5.2. THEORETICAL FRAMEWORK FOR PUMP-PROBE EXCITATION

In the realm of physics, systems are often categorized as either linear or non-linear, each exhibiting distinct responses to time-varying inputs. A linear system is characterized by its adherence to both the superposition and homogeneity principles, resulting in a predictable response to varying inputs. Conversely, a non-linear system presents a more complex interaction, where the output is not directly proportional to the input, leading to a range of dynamic behaviors.

When studying the excitation of fluorescent proteins, understanding whether the

system behaves linearly or non-linearly is essential. Proteins exhibiting a linear response to excitation display a straightforward relationship between fluorescence intensity and input power; the fluorescence would increase proportionally with input power under 1-photon excitation, for example. Some properties of a system can be treated as linear even though other processes involved at other levels are non-linear. For example, 2-photon excitation is inherently non-linear and the fluorescence intensity depends quadratically on the laser intensity, but the response to two temporally separated, sequential pulses could simply be the sum of the responses to each individual pulse. That is the case, for example, if the intermediate state is stable, i.e. it has a sufficiently long lifetime. This type of linearity implies that the fluorescence intensity measured would remain constant regardless of the delay between the pulses, making the exploration of optimal delays unnecessary and the fixed repetition rate of the laser pulses non-limiting.

However, the scenario changes dramatically in the case of non-linear responses. Non-linear excitation of proteins introduces complex interactions between the input pulses and the resultant fluorescence. Under specific excitation conditions, proteins might exhibit unexpected and exotic behaviors. This non-linearity requires a thorough investigation to identify the optimal combination of input pulses, aimed at maximizing fluorescence brightness through optimization of the pulse delay and other excitation parameters. The existence of non-linear behavior would also explain the observed discrepancies in the performance of Archaeorhodopsins under 1-photon and 2-photon excitation, highlighting the underlying complexity of these processes.¹⁶

Given the centrality of linearity and non-linearity in this chapter, it is useful to establish a robust theoretical framework to examine the behavior of fluorescent proteins. This framework will provide the foundation for our experimental approach.

5.2.1. LINEAR SYSTEMS UNDER PUMP-PROBE EXCITATION

Although the derivations presented below are formulated independently using linear systems theory, they are inspired by and grounded in established principles of ultrafast optics, nonlinear spectroscopy and systems theory.^{17,18,19}

The pulse generated by a laser cavity can be generally represented as a Gaussian wave packet of central frequency ω_0 and standard deviation σ , where the electric field takes the form:

$$E(t, \varphi) = E_0 e^{-\frac{t^2}{2\sigma^2}} e^{i(\omega_0 t + \varphi)} \quad (5.1)$$

where the phase φ is unknown *a priori*. The corresponding Fourier transform is:

$$\tilde{E}(\omega, \varphi) = \int_{-\infty}^{+\infty} E(t, \varphi) e^{-i\omega t} dt = E_0 \sqrt{2\pi\sigma} e^{i\varphi} e^{-\frac{\sigma^2}{2}(\omega - \omega_0)^2} = \tilde{E}_0 e^{i\varphi} e^{-\frac{\sigma^2}{2}(\omega - \omega_0)^2} \quad (5.2)$$

Let us consider a system we aim to characterize using a controllable input electric field i . By using an optical delay line we can prepare this input to be the sum of two identical pulses delayed by Δt :

$$i(t, \Delta t, \varphi) = E(t, \varphi) + E(t - \Delta t, \varphi) \quad (5.3)$$

Invoking the properties:

$$\mathcal{F}[f(t) + g(t)] = \mathcal{F}[f(t)] + \mathcal{F}[g(t)] \quad \mathcal{F}[f(t + \Delta t)] = \mathcal{F}[f(t)] \cdot e^{i\omega\Delta t} \quad (5.4)$$

the Fourier transform of the input electric field then becomes:

$$I(\omega, \Delta t, \varphi) = \tilde{E}(\omega, \varphi) + \tilde{E}(\omega, \varphi) \cdot e^{-i\omega\Delta t} = \tilde{E}(\omega, \varphi) \left[1 + e^{-i\omega\Delta t} \right] \quad (5.5)$$

The output electric field o will depend on the nature of the probed system. In the linear regime, the process is fully coherent and the output will then be the convolution product (in time) of the input i and a certain response function f we have yet to determine:

$$o(t, \Delta t, \varphi) = i(t, \Delta t, \varphi) * f(t) \quad (5.6)$$

Note that f is expected to depend only on time and not other experimental conditions. Note also that fluorescence is not a coherent process either, so to be accurate this model would need to integrate molecular states, where the end state sees a collapse of coherence with energy absorbed in the molecular system, rather than given back to the field. However, when the absorption and emission spectra nearly overlap and the excited state decays faster than the pulse duration, the fluorescence emission closely mirrors the instantaneous coherent excitation, justifying an approximate linear treatment.

5

Exploiting one of the properties of Fourier transforms, in the frequency domain Eq. (5.6) simply becomes the product of the two transforms:

$$O(\omega, \Delta t, \varphi) = I(\omega, \Delta t, \varphi) \cdot F(\omega) \quad (5.7)$$

where $F(\omega)$ is the transform of $f(t)$ and $O(\omega, \Delta t, \varphi)$ the transform of $o(t, \Delta t, \varphi)$. While all of these are, in principle, complex functions, our measuring systems can only give information regarding the *intensity* of the fields, which are proportional to the absolute square of the electric fields. Moreover, the data acquisition devices integrate the incoming signals over a certain period T , dictated by the sampling frequency. In a typical pump-probe spectroscopy setup the sampling period T is much larger than the repetition time T' . The measured signal will result:

$$m(\Delta t) \propto \int_0^T \left| \sum_n o(t - nT', \Delta t, \varphi_n) \right|^2 dt \quad (5.8)$$

where $n = T/T'$ is the (integer) number of repetitions in a sampling period. In the linear regime, we can assume that each output is independent from the previous ones, so the mixed terms arising from the absolute square are all negligible. The integral can be split over each repetition:

$$m(\Delta t) \propto \int_0^T \sum_n |o(t - nT', \Delta t, \varphi_n)|^2 dt = \sum_n \left[\int_{nT'}^{(n+1)T'} |o(t - nT', \Delta t, \varphi_n)|^2 dt \right] \quad (5.9)$$

If the repetition time T' is long enough compared to the pulse duration, the output can be considered fully extinguished, and then each integration range can be extended to infinity without loss of generality. The nT' delay also loses meaning here and can be dropped with a silent notation change:

$$m(\Delta t) \propto \sum_n \left[\int_{-\infty}^{+\infty} |o(t, \Delta t, \varphi_n)|^2 dt \right] \quad (5.10)$$

Invoking Parseval's theorem, this integral is equivalent to the one in the frequency domain:

$$m(\Delta t) \propto \sum_n \left[\int_{-\infty}^{+\infty} |O(\omega, \Delta t, \varphi_n)|^2 d\omega \right] \quad (5.11)$$

Considering the absolute square of **Eq. (5.7)** we can write:

$$|O(\omega, \Delta t, \varphi_n)|^2 = |I(\omega, \Delta t, \varphi_n)|^2 \cdot |F(\omega)|^2 = 2(1 + \cos(\omega\Delta t))|\tilde{E}(\omega)|^2|F(\omega)|^2 \quad (5.12)$$

where the phase of the electric field vanishes. When the quantum yield approaches unity, $|F(\omega)|^2$ is experimentally recognized as the excitation spectrum of the molecule.

The fact that the phase vanishes considerably simplifies the calculations, as the sum will be over a term not dependent on n . Combining **Eq. (5.12)** in **Eq. (5.11)**:

$$m(\Delta t) \propto \int_{-\infty}^{+\infty} \left[\sum_n (1 + \cos(\omega\Delta t))|\tilde{E}(\omega)|^2|F(\omega)|^2 \right] d\omega \propto \int_{-\infty}^{+\infty} (1 + \cos(\omega\Delta t))|\tilde{E}(\omega)|^2|F(\omega)|^2 d\omega \quad (5.13)$$

We must now extract the spectrum $|F(\omega)|^2$. To do so, we can apply a second Fourier transform to go from the *time delay domain* (which is fundamentally different from the usual *time domain*) to the *frequency delay domain* (which again is fundamentally different from the usual *frequency domain*). The variables will then be $\Delta t \leftrightarrow \Omega$ and the transform of $m(\Delta t)$ in this new domain will be depicted as $M(\Omega)$:

$$M(\Omega) = \int_{-\infty}^{+\infty} m(\Delta t) e^{-i\Omega\Delta t} d(\Delta t) \propto \int_{-\infty}^{+\infty} \left[\int_{-\infty}^{+\infty} (1 + \cos(\omega\Delta t))|\tilde{E}(\omega)|^2|F(\omega)|^2 d\omega \right] e^{-i\Omega\Delta t} d(\Delta t) \quad (5.14)$$

The exponential term can be brought inside the inner integral (being independent of ω) and the integration order can be exchanged:

$$M(\Omega) \propto \int_{-\infty}^{+\infty} \left[\int_{-\infty}^{+\infty} (1 + \cos(\omega\Delta t))e^{-i\Omega\Delta t} d(\Delta t) \right] |\tilde{E}(\omega)|^2|F(\omega)|^2 d\omega = \int_{-\infty}^{+\infty} \mathcal{I}(\omega, \Omega) |\tilde{E}(\omega)|^2|F(\omega)|^2 d\omega \quad (5.15)$$

where the transform $\mathcal{I}(\omega, \Omega)$ is:

$$\mathcal{I}(\omega, \Omega) = \delta(\Omega) + \frac{\delta(\Omega + \omega) + \delta(\Omega - \omega)}{2} \quad (5.16)$$

The other integrals are now fairly easy to solve, given the definition of the Dirac's delta:

$$M(\Omega) \propto \delta(\Omega) \underbrace{\int_{-\infty}^{+\infty} |\tilde{E}(\omega)|^2|F(\omega)|^2 d\omega}_{c = \text{constant}} + \frac{|\tilde{E}(\Omega)|^2|F(\Omega)|^2 + |\tilde{E}(-\Omega)|^2|F(-\Omega)|^2}{2} \quad (5.17)$$

Since $\tilde{E}(-\Omega) \approx 0$ we can simplify to:

$$M(\Omega) \propto c \cdot \delta(\Omega) + \frac{|\tilde{E}(\Omega)|^2|F(\Omega)|^2}{2} \quad (5.18)$$

Looking back at the measured signal $m(\Delta t)$, we can rewrite it as the sum of its average and a supplementary function which is dependent on Δt and has zero average:

$$m(\Delta t) = \langle m \rangle + \bar{m}(\Delta t) \quad (5.19)$$

This way, the constant corresponds to the Dirac's delta in the frequency delay domain.

Denoting the Fourier transform of $\bar{m}(\Delta t)$ with $\bar{M}(\Omega)$ we finally get:

$$\bar{M}(\Omega) \propto |\tilde{E}(\Omega)|^2 |F(\Omega)|^2 \quad (5.20)$$

From which:

$$|F(\Omega)|^2 \propto \frac{\bar{M}(\Omega)}{|\tilde{E}(\Omega)|^2} \quad (5.21)$$

Equation (5.21) is valid for any input, so it holds regardless of the shape of the pulse (Gaussian, Lorentzian, etc.) as long as a certain Δt delays it. It is important to notice that even if, conceptually, the transform from the time delay domain and the frequency domain are not directly related, a simple notation change gives us the usual molecular excitation spectrum $|F(\omega)|^2$. Mathematically, this is possible only because of the arising of Dirac's deltas in **Eq. (5.16)**, which leaves $|F(\omega)|^2$ unchanged under the integral.

Making all the variables explicit in the specific case of a Gaussian pulse we obtain:

$$|F(\omega)|^2 \propto \frac{\int_{-\infty}^{+\infty} (m(\Delta t) - \langle m \rangle) e^{-i\omega\Delta t} d(\Delta t)}{e^{-\sigma^2(\omega - \omega_0)^2}} \quad (5.22)$$

5

In practice, the transform will be a Discrete Fourier Transform (DFT) on a finite delay interval. The finer the Δt and the bigger the integration range, the better the resolution of the molecular excitation spectrum will be.

It is important to recognize that a system displaying linear response characteristics to ultrafast delayed pulses within a specific range does not necessarily indicate overall linearity. Non-linear behaviors may emerge under different conditions, such as higher intensities, varied delays, or with combinations involving more than two pulses. These potential non-linearities stress the need for varied experiments to fully understand the complex dynamics of protein excitation.

5.2.2. NON-LINEAR SYSTEMS IN THE WEAK-FIELD REGIME

In the previous section it was already mentioned how fluorescence is a fundamentally incoherent process, and how the linear approximation might not be valid for a variety of molecules. To complicate things, the linear framework does not account for 2-photon absorption or second harmonic generation, nor does it incorporate dynamic dephasing processes that can significantly influence the observed fluorescence. Luckily, it is still possible to describe non-linear behaviour using the formalism for second harmonic generation (SHG) without abandoning the weak-field regime.²⁰

When an electromagnetic field is applied to a system, charges start to oscillate driven by the electromagnetic force, inducing a polarization P . In the linear regime the polarization has the same frequency of the incident field:

$$P = \epsilon_0 \chi E \quad (5.23)$$

where ϵ_0 is the permittivity of vacuum and χ the electric susceptibility of the system. However, when a pulsed laser is used instead, the linear approximation is not valid anymore and the non-linear polarization must account for a quadratic term:

$$P = \epsilon_0 \chi^{(1)} E + \epsilon_0 \chi^{(2)} E^2 \quad (5.24)$$

where $\chi^{(2)}$ characterizes the non-linear response of the system.

Recall that the electric field of a single gaussian pulse is:

$$E(t) = E_0 e^{-\frac{t^2}{2\sigma^2}} e^{i(\omega t + \varphi)} \quad (5.25)$$

corresponding to an instantaneous intensity $I(t)$:

$$I(t) \propto |E(t)|^2 \propto e^{-\frac{t^2}{\sigma^2}} \quad (5.26)$$

In the case of pump-probe excitation, the incoming electric field will be the sum of two identical pulses delayed in time, therefore the non-linear polarization P_{NL} will be:

$$P_{NL} \propto (E(t) + E(t - \Delta t))^2 \quad (5.27)$$

The measured non-linear intensity will then be:

$$I(\Delta t) \propto \int_{-\infty}^{\infty} |(E(t) + E(t - \Delta t))^2|^2 dt \quad (5.28)$$

It can be immediately noticed how the phase φ is, similarly to the linear case, lost when measuring the intensity of the field. It can be shown²⁰ that for the Gaussian pulses the total non-linear intensity is given by four terms:

$$\begin{aligned} I(\Delta t) = & \underbrace{2 \int_{-\infty}^{\infty} e^{\frac{2t^2}{\sigma^2}} dt}_{\text{background}} + \underbrace{4 \int_{-\infty}^{\infty} e^{-\frac{t^2}{\sigma^2}} e^{-\frac{(t-\Delta t)^2}{\sigma^2}} dt}_{\text{intensity autocorrelation}} + \\ & + \underbrace{4 \operatorname{Re} \left[\left(\int_{-\infty}^{\infty} e^{-\frac{3t^2}{2\sigma^2}} e^{-\frac{(t-\Delta t)^2}{2\sigma^2}} dt + \int_{-\infty}^{\infty} e^{-\frac{3t^2}{2\sigma^2}} e^{-\frac{(t+\Delta t)^2}{2\sigma^2}} dt \right) e^{i\omega_0 \Delta t} \right]}_{\text{first-order interference}} + \\ & + \underbrace{2 \operatorname{Re} \left[\left(\int_{-\infty}^{\infty} e^{-\frac{t^2}{\sigma^2}} e^{-\frac{(t-\Delta t)^2}{\sigma^2}} dt \right) e^{i2\omega_0 \Delta t} \right]}_{\text{second-order interference}} \end{aligned} \quad (5.29)$$

The second-order interference term is responsible for the frequency doubling in the system, a crucial phenomenon in SHG. By calculating every term and normalizing to the background:

$$\begin{aligned} I(\Delta t) = & \sqrt{2\pi} \sigma + 2\sqrt{2\pi} \sigma e^{-\frac{\Delta t^2}{2\sigma^2}} + 4\sqrt{2\pi} \sigma \cos(\omega_0 \Delta t) e^{-\frac{3\Delta t^2}{8\sigma^2}} + \sqrt{2\pi} \sigma \cos(2\omega_0 \Delta t) e^{-\frac{\Delta t^2}{2\sigma^2}} \\ \propto & 1 + 2e^{-\frac{\Delta t^2}{2\sigma^2}} + 4 \cos(\omega_0 \Delta t) e^{-\frac{3\Delta t^2}{8\sigma^2}} + \cos(2\omega_0 \Delta t) e^{-\frac{\Delta t^2}{2\sigma^2}} \end{aligned} \quad (5.30)$$

This equation describes the non-linear intensity in response to pump-probe excitation with Gaussian (ultrafast) pulses. It can immediately be seen from Eq. (5.30) that the first-order peak has higher amplitude ($A_1 = 4A_2$) and slightly shorter pulse width ($\sigma_1 = \frac{\sqrt{3}}{2}\sigma_2$) compared to the second-order peak. In the frequency domain, the broadening of the second-order component corresponds then to a narrower bandwidth. Also in this

case, the applicability to modeling fluorescence is limited to molecules for which the excitation and emission spectra are nearly overlapping and the lifetime of the excited state shorter than the pulse width.

This theoretical framework will be necessary in the interpretation of the signal from QuasAr6a, beyond the expected 2-photon absorption. But one last question remains: how to interpret any deviation from this predicted non-linear behavior?

5.2.3. NON-LINEAR SYSTEMS UNDER MULTI-PHOTON EXCITATION

In the context of fluorescent Genetically Encoded Voltage Indicators (GEVIs), Archaeorhodopsins exhibit a photocycle that is fundamentally non-linear. Upon absorbing the first photon, these proteins undergo a series of conformational changes before emitting light in the form of fluorescence. A second photon can only be absorbed after a specific time delay, highlighting the intrinsic non-linear response to light in all Archaeorhodopsins. This is also a fundamental difference with SHG as discussed in the previous section.

We model the photocycle of QuasAr6a making use of Maclaurin's model,²¹ which describes four states, only one of which fluorescent (state Q), several photoactivatable transitions, and one voltage-sensitive transition (from M to N). Just like in the previous chapter, this model provides a detailed framework for understanding the non-linear dynamics of these proteins.

It is particularly intriguing to explore the non-linear effects arising from different responses to 1-photon continuous excitation and 2-photon pump-probe experiments. Various pathways could emerge, as illustrated in Figure 5.1, including, but not limited to:

- a) **Enhanced transition:** the transition from G to M is faster due to a more efficient absorption of photons;
- b) **Enhanced transition through an intermediate state:** probing an intermediate state M' causes the system to immediately fall into M, rather than slowly decaying into it;
- c) **Shortcut transition through an intermediate state:** probing the intermediate state M' at the correct time could provide a shortcut to state N;
- d) **Shortcut transition (potentially voltage sensitive):** the timely combination of two pulses could provide a shortcut to state N;
- e) **Shortcut transition (not voltage sensitive):** the timely combination of two pulses could provide a shortcut directly to the fluorescent state Q, potentially disrupting voltage sensitivity;
- f) **Branched alternative photocycle:** the pump-probe pulses could unlock different states and transitions otherwise inaccessible under 1-photon excitation.

The corresponding mathematical model can be treated as a continuous-time Markov chain expressed as a system of linear ODEs and solved numerically. In general, the mas-

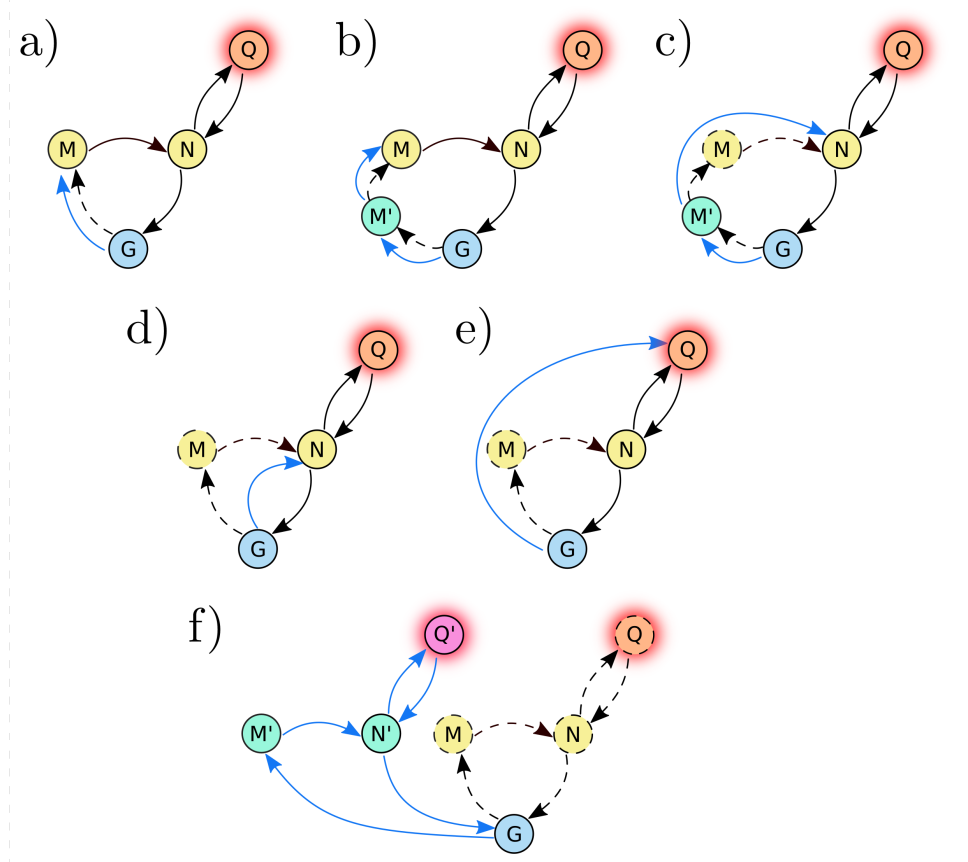


Figure 5.1: Various hypothetical mechanisms that would result in non-linear behavior under 2-photon pump-probe excitation (blue lines) compared to 1-photon continuous wave excitation (dashed lines).

ter equation takes the form:

$$\frac{d\vec{P}}{dt} = \mathbf{A}(t)\vec{P} \quad (5.31)$$

where \vec{P} is a column vector, and \mathbf{A} is the matrix of connections.

Under linear excitation, the system can be studied in its steady-state condition $\mathbf{A}(t) = \mathbf{A}$. There, the photoactivatable transitions will take the form $A_{ij} = k_{ij,m}I + k_{ij,q}$ where I is the excitation intensity, $k_{ij,m}$ and $k_{ij,q}$ are the light-dependent and light-independent components, respectively. Notice that this was the framework for the photocycle modeling employed in Chapter 4.

Modeling non-linear transitions can either be done by finding a steady-state solution in which photoactivatable transitions are in the non-linear form $A_{ij} = k_{ij,m}I_{2P}^2$, where I_{2P}^2 reflects the quadratic dependency on the average 2-photon excitation intensity, or by solving the more complicated time-dependent, non-stationary master equation where

in $A_{ij}(t) = k_{ij,m}I(t)^2$ the instant excitation intensity $I(t)$ is taken into account. The dark transitions $k_{ij,q}$ are contained in the linear transitions and would be redundant if included again.

Given these premises, it is of great interest to map these states and transitions. This mapping would offer an engineering approach to enhance and manipulate the photocycle at will, eliminating the need for protein evolution in order to achieve a desired function.

5.3. EXPERIMENTAL SETUP DESIGN

A significant limitation in the study of non-linear excitation of fluorescent proteins is typically imposed by the fixed repetition rate of mode-locked laser cavities,¹⁰ usually set at a value around 80 MHz, corresponding to a pulse every 12.5 nanoseconds. This constraint restricts the flexibility required to probe the interactions and transitions within the photocycle of these proteins. While it is true that pulse pickers extend the inter-pulse interval, they cannot generate delays shorter than the laser inherent pulse separation.

5

This limitation can be overcome by splitting the beam in two and delaying one of them via a longer optical path. As the employment of a dispersive medium would certainly cause dispersion and loss of phase alignment, one of the two arms of this delay system is instead made longer or shorter via a set of mirrors onto a movable stage. The experimental setup we developed, referred to as the optical delay line, drew inspiration from Van Dijk et al.²² and the well-known Michelson interferometers, with a key difference: to prevent unwanted reflections back into the resonant cavity, the pulse recombination is achieved using a second beam splitter (Fig. 5.2a). This recombination comes at the cost of a significant energy loss, as each pulse contains only a quarter of the original energy.

It was important for this experiment to design a setup that would fit as an add-on to the current microscope²³ and that could be reliably switched in and out without requiring realignment each time; for this reason, we used two mirrors that can be simply switched in or out manually.

In the developed setup, a pulsed beam is generated by an ultrafast laser source (Spectra-Physics Insight X3) tunable in the 680 - 1300 nm range. The first 50/50 beam splitter (Thorlabs BS015) divides the incoming pulse into two identical ones, each carrying half of the energy. Then, by controlling the position d of the mirrors in one of the two arms one can precisely control the temporal delay between the two pulses (Fig. 5.2b). This is achieved thanks to a free space optical delay line (Thorlabs ODL220/M). Distance h is fixed by design. After the second beam splitter, an IR beam block (Thorlabs LB2/M) absorbs the transmitted beam, while the reflected beam continues on the path to the sample. The pulsed beam is scanned in the XY-plane by the fastest galvanometric scanner on the market (Cambridge Technology 6215HR). Along the pathway, a long-pass dichroic mirror (Semrock Di03-R785-t3-32x44) filters the excitation from the emission. The 2-photon fluorescence or second-harmonic generation is detected by a photomultiplier tube (Hamamatsu H10721-20), amplified, filtered and digitalized by a National Instruments DAQ.

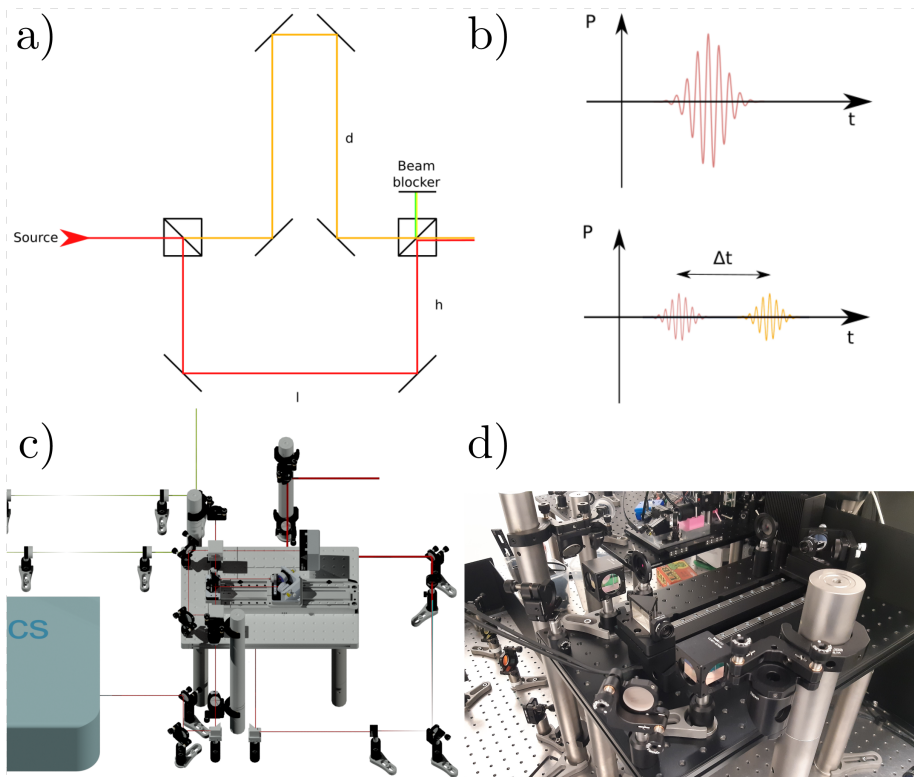


Figure 5.2: **a**, Conceptual design of the optical delay line. **b**, Pulse splitting and delay. **c**, CAD design fitting the actual microscope size. **d**, Photo of the realized design.

Given the design, the delay between the pulses will correspond to:

$$\Delta t = \frac{2|h-d|}{c} \quad (5.32)$$

where c is the speed of light in vacuum and the factor of 2 accounts for the round-trip travel in the adjustable arm. The distance h was, for practical reasons, fixed at around 5 cm; since the delay line can move between 0 and 22 cm, the maximum delay obtainable is roughly 1.13 ns. This limit was considered acceptable, as the phenomena we want to study are expected to be in the hundreds of picoseconds range.

5.4. OPTICAL DELAY LINE CALIBRATION

Before directly applying the delay line to fluorescent proteins, we needed to perform some preliminary calibration experiments. The rationale behind this calibration was multifaceted: to determine the exact position corresponding to zero delay (i.e., where $d = h$), to characterize the generated pulse (ensuring the wavelength and pulse width matched the manufacturer's specifications) and to map any spatial distortions and aberrations caused by the objective.

After carefully aligning the system, we measured the power after the objective and observed a power loss due to beam expansion, which becomes more and more significant at large delays (Fig. 5.3a). The beam expansion is inevitable given the free-space propagation for relatively long distances in the delay line. Any longer range measurement has been corrected for this drop in excitation.

5

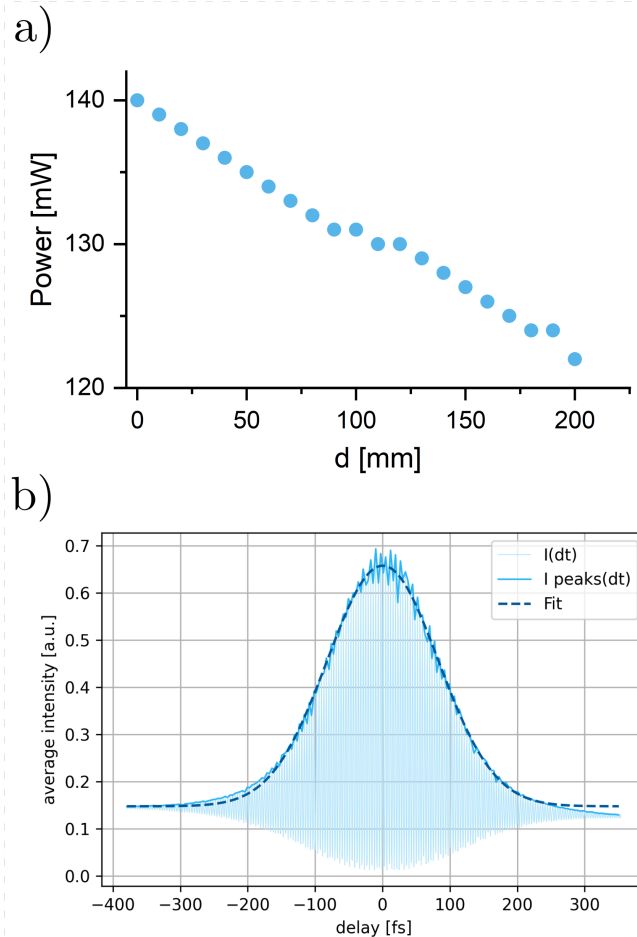


Figure 5.3: **a**, Power losses due to beam expansion measured after the objective ($\lambda = 1100$ nm). **b**, Autocorrelation measured from the second harmonic generation of iron iodate nanoparticles ($\lambda = 1100$ nm). The gaussian envelope is fitted from the peaks only.

We chose iron iodate nanoparticles ($\text{Fe}(\text{IO}_3)_3$) as our calibration sample due to their strong second harmonic generation.²⁴ These nanoparticles allow us to measure the autocorrelation of the pulse by employing Eq. (5.30). From this, we obtain two crucial pieces of information: first, the location where the autocorrelation is maximum, corresponding to total constructive interference and indicating the "zero delay" of the delay line; second, scanning around the zero fully maps the autocorrelation of the pulse, from

which we can determine the pulse width. The relationship between the full-width half-maximum (FWHM) of the pulse as a function of the delay and the standard deviation σ of the autocorrelation in space is given by:²⁵

$$\text{FWHM} = 4\sqrt{\ln 2} \frac{\sigma}{c} \quad (5.33)$$

Every pixel in the measured field of view is accounted for in the computation of the mean autocorrelation given the rather uniform sample. From the autocorrelation measurement (Fig. 5.3b), we establish the zero of the delay line (6.9766 mm) and the pulse width (138 fs). For reference, the manufacturer guarantees a pulse width of less than 200 fs, which aligns with our measurement.

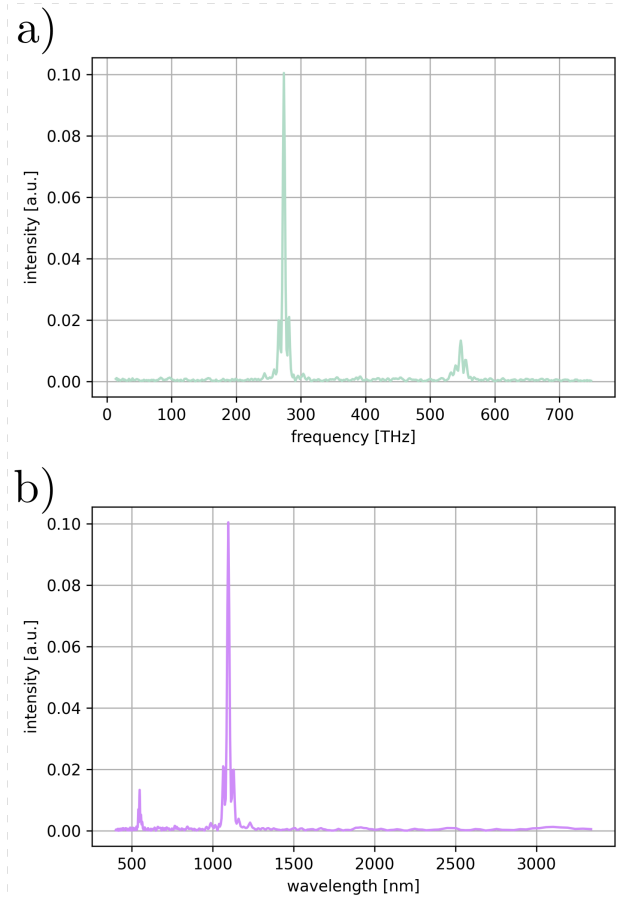


Figure 5.4: **a**, Frequency and **b** wavelength spectrum of the autocorrelation signal. The signature first- and second-order interference peaks confirm what expected from second harmonic generation.

By calculating the FFT in the frequency domain (Fig. 5.4a) and transforming it to the wavelength domain (Fig. 5.4b) we could confirm that the first-order peak corresponded

exactly to 1100 nm (Eq. (5.30)), as set on the instrument. The clear appearance of this peak in the FFT spectrum confirms that our system calibration is accurate and that the delay line preserves the intended pulse characteristics. The second-order peaklet corresponds to the expected signature of frequency doubling in second harmonic generation Eq. (5.30)).

5.5. AUTOCORRELATION SPATIAL IMAGING

An important aspect to consider in pump–probe experiments is the potential for spatial variation in the interference pattern across the objective’s field of view. It cannot be assumed a priori that the pulses will interfere identically at every position; differences in incidence angle may lead to variations such as peak broadening or shifts in the zero-delay point. Recognizing this, we performed a systematic spatial mapping of the autocorrelation signal. Specifically, we repeated the autocorrelation measurement over 9 distinct fields of view, calculated the zero-delay and full-width at half-maximum (FWHM) for each pixel, and then created a mask to isolate pixels responsive to the delay sweep. These masks were subsequently averaged to generate composite maps representing the zero position and the pulse width (see Fig. 5.5).

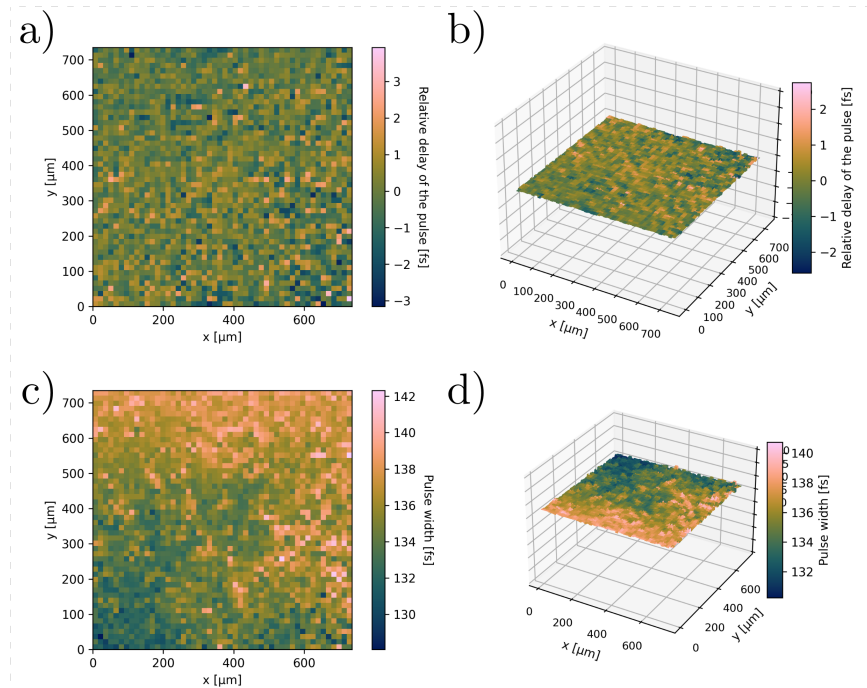


Figure 5.5: Spatial effects on the zero-delay (a-b) and pulse width (FWHM, c-d). The maps show that while the zero-delay remains uniform across the field of view, only minimal variations in pulse width are observed.

Our analysis revealed no appreciable variation in the zero-delay position across the field of view. More importantly, while there was a minimal effect on the pulse width, this

was negligible given the time scales involved. This result is significant because spatial mapping of pump-probe autocorrelation signals is not commonly performed due to the inherent technical challenges of ultrafast measurements. Mapping how spatial position within the objective affects pulse width not only serves as a rigorous calibration check, but also provides a new tool to perform ultrafast spectroscopic imaging. The ability to resolve these features in space can be useful in future studies beyond live cell imaging.

5.6. PRELIMINARY EXPERIMENTS ON LIVE CELLS

Initial experiments on live cells were conducted on QuasAr1 (Q1), QuasAr2 (Q2) and QuasAr6a (Q6a) to assess their performance under two-photon excitation within our experimental conditions. To reproduce these, we set the excitation to 1170 nm, the ND filter to 0.5 and the amplification gain to 10^7 . The fluorescence data collected over time was segmented to isolate the cells from the background. A standard deviation threshold was applied to identify areas with significant variation in fluorescence, assumed to correspond to cells. The resulting mask was used to extract the average fluorescence from these regions across all time frames. The fluorescence traces were then normalized to the initial mean intensity to account for the inherent cell-to-cell variability in brightness (Fig. 5.6).

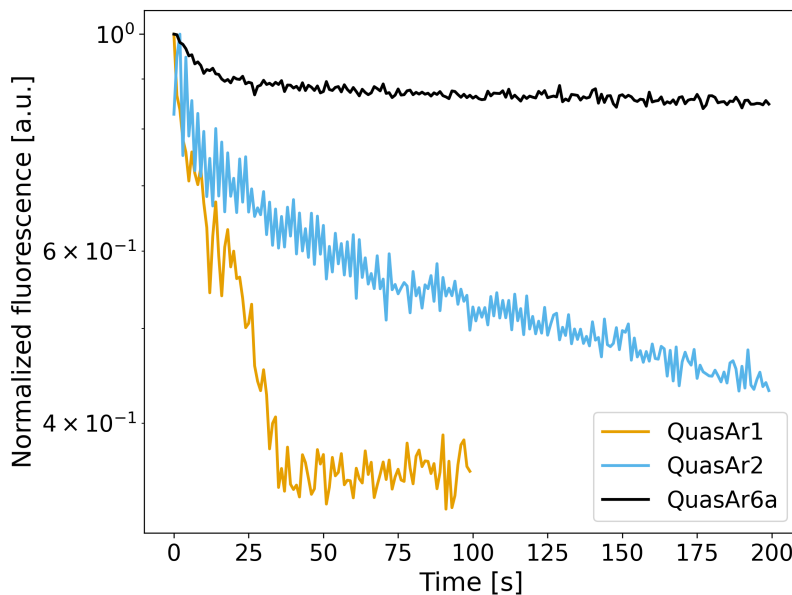


Figure 5.6: Photobleaching curves for different QuasAr variants. Q1 and Q2 exhibit low photostability and insufficient brightness, while Q6a demonstrates suitability for prolonged measurement.

Both the Q1 and Q2 variants presented significant limitations: at the power levels required for sufficient fluorescence signal, rapid photobleaching occurred within seconds, making them impractical for extended measurements. In contrast, Q6a showed

significantly improved stability, maintaining fluorescence over extended excitation periods without rapid decay. Additionally, Q6a exhibited a sufficient brightness under two-photon excitation, making it the preferred candidate for non-linear pump-probe tests.

5.6.1. AUTOCORRELATION REGIME

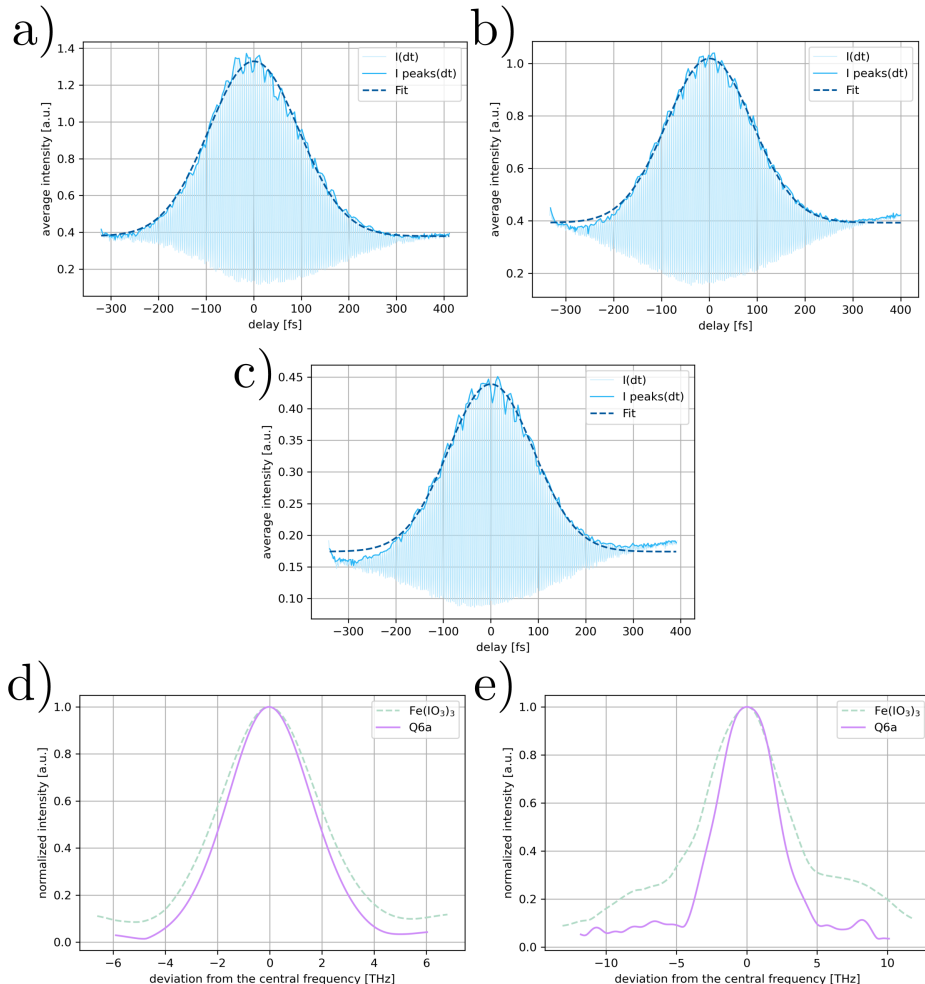


Figure 5.7: **0-400 fs time scale:** Q6a does not exhibit non-linearities in the autocorrelation regime, neither in the delay space (**a-c**) nor in the Fourier space (**d** first-order and **e** second-order interference peak). The spectra presented are the average from the spectra of the three measurements above.

To investigate potential non-linear effects in the fluorescence response of Q6a, we performed an autocorrelation analysis around zero delay in the same way it was performed on the calibration sample. This time scale (hundreds of femtoseconds) falls within the autocorrelation regime, where the pump and probe pulses interfere before

directly exciting the fluorescent protein. If significant non-linear interactions occurred at this timescale, deviations from the calibration autocorrelation in **Fig. 5.3b** would be expected. Any deviations observed in this regime would suggest spectral non-linearity rather than a process linked to the photocycle.

One potential detrimental factor in this analysis was photobleaching, which introduced a systematic decay in the fluorescence intensity. To mitigate this, we subtracted the decay trend from the autocorrelation data. The measured autocorrelation curve did not reveal strong deviations indicative of non-linear processes (**Fig. 5.7a-c**).

The Fourier transform of the corrected signal was calculated to verify whether any frequency components corresponding to unexpected transitions emerged. The curves were also interpolated in the frequency space via artificial zero-padding, which does not add information but prevents discontinuity of the data. Despite these refinements, no strong evidence of previously unreported non-linear fluorescence effects was observed within the explored delay range (**Fig. 5.7d,e**). We notice only a slight narrowing of the bandwidth when comparing Q6a fluorescence with the SHG of the $\text{Fe}(\text{IO}_3)_3$ calibration sample, corresponding to a slightly wider pulse in time. This effect can be attributed to a coherence in Q6a with a slightly longer lifetime.

This lack of significant deviation confirms that any strong non-linear effect, if present, would likely not be rooted in the immediate interference of the pulses.

5.6.2. MOLECULAR VIBRATIONS REGIME

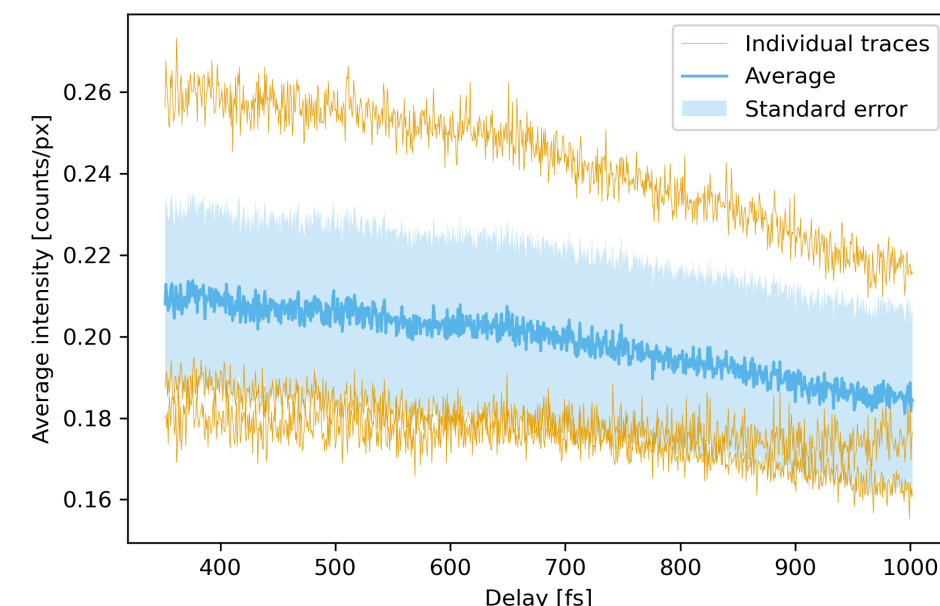


Figure 5.8: **350 fs-1 ps time scale:** the background-subtracted data exhibit a flat response with no significant oscillatory features distinguishable from pink noise.

In the molecular vibrations regime, spanning approximately 350 fs to 1 ps, we aimed to probe the rapid vibrational dynamics inherent to the protein's structure. In this time window, vibrational wave-packets generated in the protein are expected to evolve and interfere, producing oscillatory modulations in the fluorescence intensity. Such modulations arise from the periodic constructive and destructive interference of vibrational coherences.

By sweeping the delay in fine increments of 0.67 fs, our objective was to resolve oscillatory features that may arise from the coherent excitation of specific vibrational modes. These vibrational excitations, potentially linked to bond stretching and bending within the protein structure, could modulate the electronic transitions and, consequently, the fluorescence yield. For all measurements in the said range, the background was subtracted from the signal by segmenting the cells with a simple threshold on the standard deviation. A χ^2 test confirmed that the trend was consistent with a constant (reduced $\chi^2 = 0.16$, $DOF = 975$, p -value = 1.00). The random deviations throughout the measurement are indistinguishable from pink noise, possibly arising from the PMT flicker noise.

5

The data in **Fig. 5.8** indicate that, under our current experimental conditions, the expected vibrational dynamics does not manifest as measurable modulations in the fluorescence signal. Despite the fine delay increments, the consistent flat trend suggests that any coherent vibrational excitations are either too subtle to detect, or are masked by dominant electronic transitions. This emphasizes the need for either enhanced signal-to-noise sensitivity or alternative probing methods, at least in this range.

5.6.3. ULTRAFAST TRANSITIONS REGIME

Beyond the molecular vibrations regime, experiments were extended to longer delay times, in different ranges, up to 1 ns. This regime corresponds to the ultrafast transition in the photocycle, or in other words the first transition in MacLaurin's model.

A key challenge in these measurements was maintaining internal consistency, as photobleaching effects could introduce artifacts over long acquisition times. To counteract this, an interleaved measurement strategy was implemented, where delays were alternated with the first delay (acting as a reference point) to correct for photobleaching.

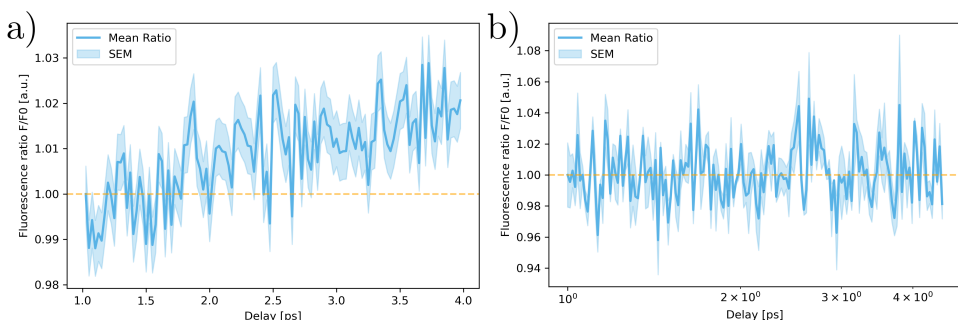


Figure 5.9: 1 ps-4 ps time scale: Relative fluorescence intensity measurements obtained using both linear (a, 25 fs steps) and logarithmic (b) delay sampling. Although an apparent upward trend is seen in the linear data, the signal remains statistically constant, indicating no detectable non-linear transition in this regime.

Despite the apparent upward trend in **Fig. 5.9a**, a χ^2 test confirmed that the measured relative intensity was consistent with a constant (reduced $\chi^2 = 0.28$, $\text{DOF} = 118$, $p\text{-value} = 1.00$). The absence of non-linearities is confirmed by the measurement tested in the same range, but using a logarithmic sampling instead (**Fig. 5.9b**). As in previous measurements, the random deviations are indistinguishable from pink noise.

Similar measurements were conducted in the 4–12 ps delay range. Here the fluorescence signal of Q6a remained remarkably stable (**Fig. 5.10**), exhibiting, again, no significant deviations from a constant baseline, undistinguishable from pink noise. Both the uniform and logarithmic sampling approaches consistently confirmed the absence of any non-linear transition that might point to additional rapid photodynamic processes. It is likely that any non-linear contributions, potentially arising from complex conformational changes or cooperative interactions, must occur at different time scales, if present.

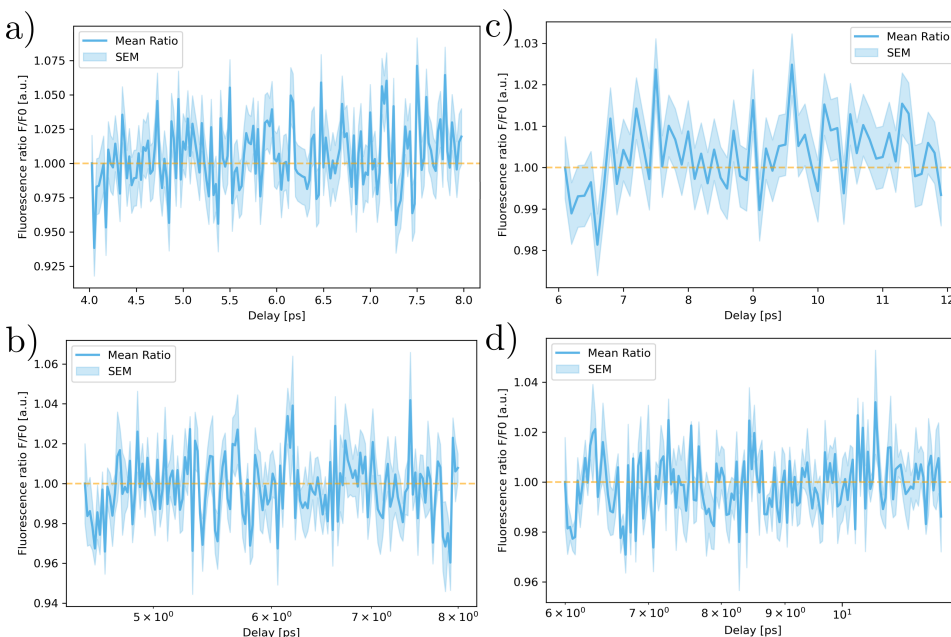


Figure 5.10: 4 ps–12 ps time scale: Relative fluorescence intensity measurements in the ultrafast regime from 4 ps to 12 ps, obtained using both uniform 25 fs steps (a,c) and logarithmic (b,d) delay sampling. The data reveal no detectable non-linearities, suggesting that the photocycle dynamics remain predominantly linear in this interval.

To probe the 10 ps–1 ns delay range, a logarithmic sampling approach was deemed the only feasible strategy given the extended range. However, some significant technical challenges arose: the delay line struggled to reach setpoints when provided with overly precise numerical values, calculated digitally via our Python script, which caused the system to crash multiple times. This instability hampered data reliability in this range, and the issue was only fully recognized toward the end of the project, leaving insufficient time to implement a better, more robust solution.

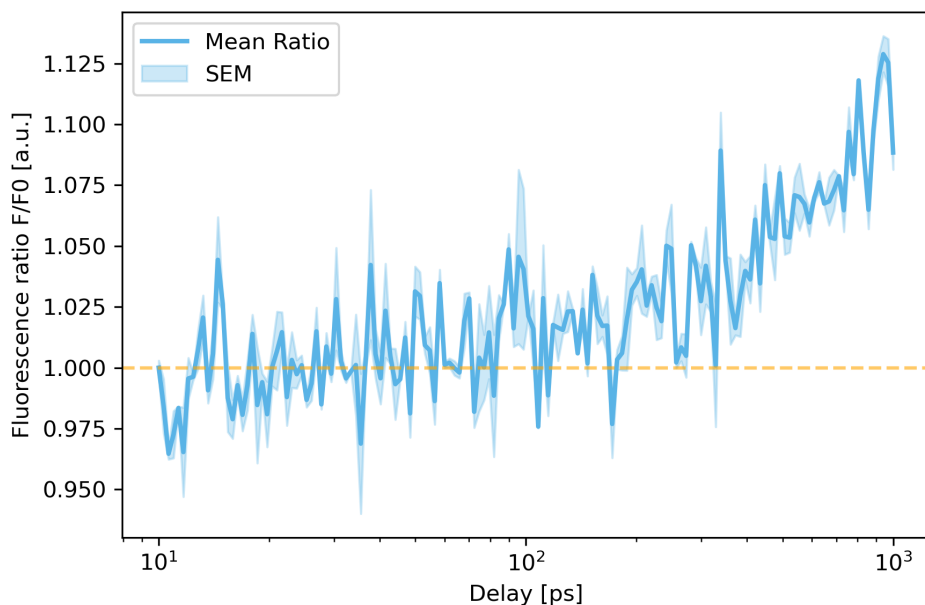


Figure 5.11: **10 ps–1 ns time scale:** A moderate, reproducible enhancement in fluorescence intensity up to 10% above the baseline is noticeable from a delay of approximately 300 ps onward.

In this range (Fig. 5.11), we observed a moderate yet reproducible enhancement in fluorescence intensity, reaching up to 10% above the baseline, particularly evident from delays of approximately 300 ps onward. This upward trend may signal the some sort of non-linear transition associated with the initial conformational change described in MacLaurin's photocycle model. In other words, the system appears to begin diverging from a purely linear response under these conditions.

To fully validate this observation, repeated measurements are still needed. Among the various options for extending the photocycle model (Fig. 5.1), assessing any change in voltage sensitivity is very important. The first phototransition could be either amplified, or completely redirected to a different state, with implications on the protein conformation too. For this reason, integrating these experimental findings with refined theoretical models could reveal the interplay between electronic excitation and early structural rearrangements, advancing our understanding of the underlying non-linear dynamics.

5.7. INTERPRETATION AND FUTURE OUTLOOK

In light of the preliminary nature of these experiments, it is important to approach our findings with both cautious optimism and a realization of the inherent limitations of the current setup. Given the limited size of the dataset, particularly in the critical 300 ps to 1 ns delay range, repeated measurements are still needed. The current delay line,

constrained by the physical dimensions of the setup, limits our ability to explore longer delays. Substituting it with a longer delay line could be a necessary upgrade to fully capture the non-linear dynamics at extended timescales.

A practical challenge encountered during these experiments was the generation of a logarithmic delay range without truncating numerical values. This led to situations where the step motor could not reach the setpoint with the required precision, consuming valuable troubleshooting time. Future implementations must incorporate proper numerical truncation to ensure that the step motor setpoint remain within the operational accuracy.

Preliminary results suggest that, as delays approach 1 ns, a non-linear behavior may be stimulated. This result is of particular interest because the ultrafast regime is not commonly probed in rhodopsin research, as typically inaccessible to conventional transient-absorption spectroscopy. By exploring these ultrafast timescales, we believe we could gain deeper insights into the photocycle dynamics, refine existing models and enable more accurate quantitative predictions, especially when excitation deviates from linearity or interacts with a nanoantenna (as discussed in Chapter 4).

For fundamental understanding, any deviation from a flat, unresponsive baseline is of great interest. Should such deviations be confirmed, the underlying models must be revisited to incorporate modifications in the photocycle dynamics, as elaborated in previous sections. From an application perspective, an additional practical requirement arises: the signal at a fixed delay should ideally double relative to the baseline. Considering that the optical delay line inherently loses 50% of the power, achieving the same output with reduced photobleaching would open the door to the design of a compact, cost-effective mini-delay line. Such a device, precisely aligned and integrated with a laser source, could be calibrated and fixed for each protein of interest.

All experiments reported in this chapter have been conducted using pulses centered at 1170 nm, which corresponds to the peak of two-photon absorption for QuasAr6a.²⁶ A systematic scan of the excitation spectrum around this central wavelength may reveal alternative non-linearities, possibly manifesting at different time scales or intensities. Such findings would indicate specific action spectra associated with the initial photo-transition, rather than a uniform response from the protein as a whole.

Finally, considering the goal of developing more effective genetically encoded voltage indicators, it is advisable to extend the same approach to a broader selection of Archaeorhodopsins. Despite sharing a similar photocycle, small variations among these proteins could elucidate the fundamental mechanisms underlying fluorescence emission in voltage-sensitive systems. This comparative analysis holds promise for both enhancing our fundamental understanding and guiding the practical engineering of the next-generation voltage indicators.

5.8. METHODS

5.8.1. IRON IODATE SAMPLE PREPARATION

To prepare the calibration sample, 10 mg of iron iodate nanopowder (PlasmaChem PL-FeIO80) were dispersed in 150 μ L of MilliQ water and thoroughly mixed until the formation of a homogeneous, white solution. Then the solution was drop-casted onto a

glass bottom dish (Cellvis, D35-14-1.5-N) and let dry overnight. The sample was stored at room temperature.

5.8.2. HEK293T CULTURE

HEK293T cells (Catalog number ATCC® CRL-3216™) with passage number <30 were cultured in Dulbecco's Modified Eagle Medium (DMEM) supplemented with 10% Fetal Bovine Serum (VWR Seradigm Premium Grade), 50 units/mL Penicillin (Life Technologies), 50 µg/mL Streptomycin (Life Technologies), and 1% GlutaMAX (Life Technologies) at 37 °C under 10% CO₂.

5.8.3. LENTIVIRUS PREPARATION AND TRANSDUCTION

For lentivirus production, HEK293T cells were seeded at 4·10⁶ cells per 100 mm polystyrene dish (Sarstedt) 1 day before transfection in order to achieve 80% confluence at the moment of transfection. Cells were co-transfected with 1.5 µg transfer plasmid carrying either QuasAr1, QuasAr2 or QuasAr6a, 5 µg of pMDLg/RRE (Addgene plasmid #12251), 5 µg of pRSV/Rev (Addgene plasmid #12253), and 3.5 µg of pMD2.G (Addgene plasmid #12259) mixed in 400 µL pre-warmed opti-MEM with 60 µL polyethylenimine solution (1 µg/µL in PBS). 8 hours post-transfection, medium was replaced with fresh cell culture medium including 25 mM HEPES. Lentivirus-containing supernatant was collected 48 and 72 hours post-transfection. Supernatant collected 48 hours post-transfection was stored overnight at 4 °C before pooling it with lentivirus collected 72 hours post-transfection. Supernatant was filtered through 0.22 µm PVDF filters. Lentivirus was concentrated 15-fold using Lentix concentrator reagent (Takara), resuspended in PBS, and stored at -80 °C in 100 µL aliquots.

For lentiviral transduction, 2.5·10⁵ cells were seeded per 35 mm polystyrene dish (Sarstedt) 1 day before transduction in order to achieve 50% confluence at the moment of transduction. Lentiviral aliquots were rapidly thawed in a 37 °C water bath. 100 µL of concentrated virus was added per dish. Cells were incubated with lentivirus for 24 hours, after which the media was replaced with fresh cell culture medium.

5.8.4. MULTIPHOTON FLUORESCENCE MICROSCOPY

A pulsed beam was generated by an ultrafast laser source (Spectra-Physics Insight X3) tunable in the 680 - 1300 nm range. The first 50/50 beam splitter (Thorlabs BS015) divided the incoming pulse into two identical ones, and delayed one of the two thanks to a free space optical delay line (Thorlabs ODL220/M). After the second beam splitter, an IR beam block (Thorlabs LB2/M) absorbs the transmitted beam, while the reflected beam continues on the path to the sample. The pulsed beam is scanned in the XY-plane by the fastest galvanometric scanner on the market (Cambridge Technology 6215HR). Along the pathway, a long-pass dichroic mirror (Semrock Di03-R785-t3-32x44) filters the excitation from the emission. The 2-photon fluorescence or second-harmonic generation is detected by a photomultiplier tube (Hamamatsu H10721-20), amplified, filtered and digitalized by a National Instruments DAQ. The precise control of the optical delay line, scanning of the galvos and registration of the PMT signal was done via custom-written Python code.

BIBLIOGRAPHY

- [1] Marcos Dantus and Vadim V. Lozovoy. "Experimental coherent laser control of physicochemical processes". In: *Chemical Reviews* 104.4 (2004). ISSN: 00092665. DOI: [10.1021/cr020668r](https://doi.org/10.1021/cr020668r).
- [2] Lukasz Piatkowski, Nicolò Accanto, and Niek F. Van Hulst. "Ultrafast Meets Ultra-small: Controlling Nanoantennas and Molecules". In: *ACS Photonics* 3.8 (2016). ISSN: 23304022. DOI: [10.1021/acspophotonics.6b00124](https://doi.org/10.1021/acspophotonics.6b00124).
- [3] Ahmed H. Zewail. *Femtochemistry: Atomic-scale dynamics of the chemical bond using ultrafast lasers*. 2000. DOI: [10.1002/1521-3773\(20000804\)39:15<2586::AID-ANIE2586>3.0.CO;2-0](https://doi.org/10.1002/1521-3773(20000804)39:15<2586::AID-ANIE2586>3.0.CO;2-0).
- [4] Moshe Shapiro and Paul Brumer. *Quantum Control of Molecular Processes: Second Edition*. 2012. DOI: [10.1002/9783527639700](https://doi.org/10.1002/9783527639700).
- [5] Daan Brinks et al. "Visualizing and controlling vibrational wave packets of single molecules". In: *Nature* 465.7300 (2010). ISSN: 00280836. DOI: [10.1038/nature09110](https://doi.org/10.1038/nature09110).
- [6] Richard Hildner, Daan Brinks, and Niek F. Van Hulst. "Femtosecond coherence and quantum control of single molecules at room temperature". In: *Nature Physics* 7.2 (2011). ISSN: 17452481. DOI: [10.1038/nphys1858](https://doi.org/10.1038/nphys1858).
- [7] Elisa Palacino-González, Maxim F. Gelin, and Wolfgang Domcke. "Theoretical aspects of femtosecond double-pump single-molecule spectroscopy. I. Weak-field regime". In: *Physical Chemistry Chemical Physics* 19.48 (2017). ISSN: 14639076. DOI: [10.1039/c7cp04809b](https://doi.org/10.1039/c7cp04809b).
- [8] A. Assion et al. "Control of chemical reactions by feedback-optimized phase-shaped femtosecond laser pulses". In: *Science* 282.5390 (1998). ISSN: 00368075. DOI: [10.1126/science.282.5390.919](https://doi.org/10.1126/science.282.5390.919).
- [9] Herschel Rabitz et al. *Whither the future of controlling quantum phenomena?* 2000. DOI: [10.1126/science.288.5467.824](https://doi.org/10.1126/science.288.5467.824).
- [10] Norbert F. Scherer et al. "Fluorescence-detected wave packet interferometry: Time resolved molecular spectroscopy with sequences of femtosecond phase-locked pulses". In: *The Journal of Chemical Physics* 95.3 (1991). ISSN: 00219606. DOI: [10.1063/1.461064](https://doi.org/10.1063/1.461064).
- [11] Daan Brinks et al. "Ultrafast dynamics of single molecules". In: *Chemical Society Reviews* 43.8 (2014). ISSN: 14604744. DOI: [10.1039/c3cs60269a](https://doi.org/10.1039/c3cs60269a).
- [12] F. Phil Brooks et al. "Optical constraints on two-photon voltage imaging". In: *bioRxiv* (2024). DOI: [10.1101/2023.11.18.567441](https://doi.org/10.1101/2023.11.18.567441).

- 5
- [13] Gitt Panitchayangkoon et al. "Long-lived quantum coherence in photosynthetic complexes at physiological temperature". In: *Proceedings of the National Academy of Sciences of the United States of America* 107.29 (2010). ISSN: 00278424. DOI: [10.1073/pnas.1005484107](https://doi.org/10.1073/pnas.1005484107).
 - [14] Richard Hildner et al. "Quantum coherent energy transfer over varying pathways in single light-harvesting complexes". In: *Science* 340.6139 (2013). ISSN: 10959203. DOI: [10.1126/science.1235820](https://doi.org/10.1126/science.1235820).
 - [15] Richard Hildner et al. "Electronic coherences and vibrational wave-packets in single molecules studied with femtosecond phase-controlled spectroscopy". In: *Physical Chemistry Chemical Physics* 13.5 (2011). ISSN: 14639076. DOI: [10.1039/c0cp02231d](https://doi.org/10.1039/c0cp02231d).
 - [16] Margherita Maiuri, Marco Garavelli, and Giulio Cerullo. "Ultrafast Spectroscopy: State of the Art and Open Challenges". In: *Journal of the American Chemical Society* 142.1 (2020). ISSN: 15205126. DOI: [10.1021/jacs.9b10533](https://doi.org/10.1021/jacs.9b10533).
 - [17] Shaul Mukamel. *Principles of Nonlinear Optical Spectroscopy*. Oxford University Press, 1999. ISBN: 9780195132915.
 - [18] Andrew M. Weiner. *Ultrafast Optics*. 2009. ISBN: 9780470473467. DOI: [10.1002/9780470473467](https://doi.org/10.1002/9780470473467).
 - [19] Robert W. Boyd. *Nonlinear Optics*. 2020. ISBN: 9780128110027. DOI: [10.1016/C2015-0-05510-1](https://doi.org/10.1016/C2015-0-05510-1).
 - [20] Ursula Keller. *Ultrafast Lasers*. Cham: Springer International Publishing, 2021. ISBN: 978-3-030-82531-7. DOI: [10.1007/978-3-030-82532-4](https://doi.org/10.1007/978-3-030-82532-4).
 - [21] Dougal Maclaurin et al. "Mechanism of voltage-sensitive fluorescence in a microbial rhodopsin". In: *Proceedings of the National Academy of Sciences of the United States of America* 110.15 (2013). ISSN: 00278424. DOI: [10.1073/pnas.1215595110](https://doi.org/10.1073/pnas.1215595110).
 - [22] E. M.H.P. Van Dijk et al. "Single-molecule pump-probe experiments reveal variations in ultrafast energy redistribution". In: *Journal of Chemical Physics* 123.6 (2005). ISSN: 00219606. DOI: [10.1063/1.1940567](https://doi.org/10.1063/1.1940567).
 - [23] Xin Meng et al. "A compact microscope for voltage imaging". In: *Journal of Optics (United Kingdom)* 24.5 (2022). ISSN: 20408986. DOI: [10.1088/2040-8986/ac5dd5](https://doi.org/10.1088/2040-8986/ac5dd5).
 - [24] Nicolò Accanto et al. "Phase control of femtosecond pulses on the nanoscale using second harmonic nanoparticles". In: *Light: Science and Applications* 3 (2014). ISSN: 20477538. DOI: [10.1038/lsa.2014.24](https://doi.org/10.1038/lsa.2014.24).
 - [25] Eric W. Weisstein. *Gaussian Function*. URL: <https://mathworld.wolfram.com/GaussianFunction.html>.
 - [26] Arita Silapetere et al. "QuasAr Odyssey: the origin of fluorescence and its voltage sensitivity in microbial rhodopsins". In: *Nature Communications* 13.1 (2022), p. 5501. ISSN: 2041-1723. DOI: [10.1038/s41467-022-33084-4](https://doi.org/10.1038/s41467-022-33084-4). URL: <https://doi.org/10.1038/s41467-022-33084-4>.

6

CONCLUSIONS, SOCIETAL IMPACT AND FUTURE OUTLOOK

Scientific breakthroughs often arise at the intersection of disciplines, where innovations in one area find transformative applications in another. Among the many examples, DeepMind's AlphaFold has redefined protein structure prediction by combining artificial intelligence with structural biology,¹ soft robotics is inspired by natural design to develop flexible machines that interact with complex environments,² brain–computer interfaces blend neuroscience, engineering and computer science to translate neural signals into direct control commands,³ and lab-on-a-chip technologies combine microfluidics and photonics to miniaturize laboratory processes.⁴ This thesis embodies that spirit, merging nanophotonics, ultrafast spectroscopy and optogenetics to look for new strategies for manipulating the function of Genetically Encoded Voltage Indicators (GEVIs). At the same time, the dissertation revolved around a single, overarching idea: the manipulation of the photocycle of QuasAr6a. In contrast to traditional strategies that rely on genetic modifications to improve voltage sensitivity or fluorescence brightness, this work demonstrated that physical interventions like plasmonic enhancement and ultrafast pulse shaping can alter the dynamics and performance of microbial GEVIs.

Chapter 2 followed a rigorous analytical treatment of plasmonic resonances in metal nanoparticles, reviewing the complete classical model that connects material properties, geometry and environmental factors. This groundwork was expanded in Chapter 3 through Finite-Difference Time-Domain (FDTD) simulations to study the behavior of nanoparticles with non-trivial shapes, especially nanostars, where sharp tips enabled the achievement of intense and tunable field enhancements. In Chapter 4, these enhanced fields were made interact with GEVIs (QuasAr6a in particular) expressed in living cells, to control their fluorescence and voltage-response kinetics. Finally, Chapter 5 tried a completely different approach, although grounded in the same idea of physically manipulating the photocycle, by employing degenerate pump–probe techniques in the ultrafast domain.

6.1. KEY SCIENTIFIC CONTRIBUTIONS

The contributions of this work are significant both within the realm of nanophotonics and in the broader context of bioengineering and optogenetics, where they find a direct application.

The analytical framework for understanding plasmonic resonances in metal nanoparticles is a useful resource for scholars and educators in electromagnetism, advanced optics and nanotechnology. By developing an analytical model that incorporates various levels of corrections, I provided a robust tool for predicting and tuning the optical behavior of virtually any ellipsoidal nanoparticle. In particular, original work includes the derivation of the generalized Clausius-Mossotti relation for ellipsoids and of the Fröhlich condition, novel proofs for the normalization of depolarization factors, the surface damping correction and the Modified Long-Wavelength Approximation, and the formulation of a unified analytical model for plasmonic resonances in ellipsoids. The derivations are complete and logical, and are explained consistently without assuming prior knowledge.

With regard to the use of Finite-Difference Time-Domain (FDTD) simulations, the simulation of the optical properties of various nanoparticle shapes is extremely useful for practical applications, where tailored enhancements can be obtained given a specific application. These insights can be used to help improve fluorescence signals and modulate protein kinetics. Original contributions include the simulation of optical properties of nanospheres, nanorods and different types of nanostars, the formulation of an empirical curve to predict the resonance of nanorods and the study of the rotational properties of nanostars.

One of the major contributions of this thesis is definitely the paradigm shift stemming from the use of plasmonic nanoparticles to enhance the function of fluorescent voltage sensors in living cells. This approach circumvented the limitations of genetic engineering by directly manipulating the optical properties of proteins, enabling faster response times and higher signal intensities in voltage imaging. Although the entire work related to this chapter is novel and original, the most important contributions related to the coupling of fluorophores to nanostars under different conditions (in solution, embedded in artificial lipid membranes, drop-cast or fixed and embedded in a fibronectin layer) and the voltage sensitivity experiments. The photocycle model formulated is also innovative and, in a sense, disruptive, as it matches experimental results by considering a phototransition that is manipulated, for the first time, via plasmonic coupling.

The pioneering use of degenerate pump–probe excitation to study the non-linear dynamics of QuasAr6a also will surely inspire new insights into the protein’s photocycle. By establishing a link between ultrafast excitation and selective modulation of transition rates, this work could open up the possibility of controlling protein function on previously inaccessible timescales. Original contributions include the rigorous demonstration of the relation between the signal measured at different pump-probe delays and the (linear) fluorophore spectrum, the design and development of the optical delay line, the comparison between the performance of different QuasAr GEVIs and the search for non-linearities in the ultrafast delay range. While preliminary, the results will inspire future research in the manipulation of protein function through non-linear excitation.

6.2. FUTURE OUTLOOK

Although the results reported in this thesis represent a significant step forward, many improvements can still be implemented in the short- and medium-term.

First and foremost, refining the functionalization protocols to control the exact spacing of nanoparticles relative to the target proteins could further enhance coupling efficiency, as extensively discussed in Chapter 4. Additionally, the synthesis of gold nanostars with optimal geometries remains a critical area of focus. I expect the search for optimized nanoparticle design to be boosted in the coming years thanks to the use of AI predictions.⁵

Plasmonic enhanced voltage imaging finds its natural application in neuroscience, where real-time monitoring of neuronal activity with high spatial and temporal resolution is essential for understanding the complexities of brain function and disorders. For instance, understanding electrical compartmentalization within dendritic spines, a key element in synaptic integration and plasticity,⁶ remains challenging with conventional techniques.⁷ The enhanced signals provided by plasmonic nanoparticles could enable unprecedented access to these nanoscopic subcellular domains in neuronal stem cell samples from patients (Fig. 6.1), enabling the optical detection of sub-threshold voltage changes in these otherwise invisible structures. Such an approach would enable the mapping of rapid electrical events across complex neuronal networks, facilitating the study of phenomena such as synaptic transmission and dendritic integration in real time.

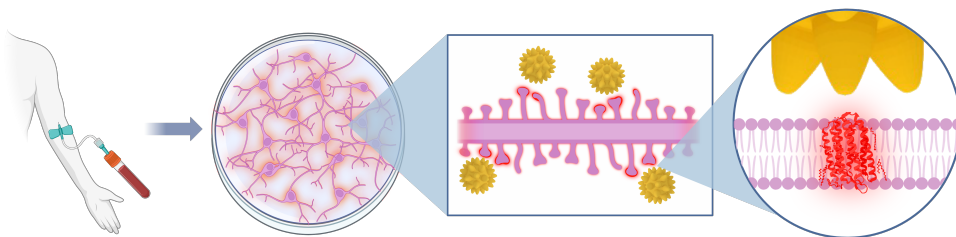


Figure 6.1: Neural stem cells can be differentiated from a blood sample of a patient. The electrical properties of neurological diseases can be studied at a dendritic spine level thanks to targeted plasmonic enhancement. Illustration made in BioRender.

Then, the preliminary observations in the ultrafast regime, especially the moderate non-linear enhancements observed at delays beyond 300 ps, call for repeated experiments. Once statistical significance is reached, the next step would involve modeling the non-linear effects in the photocycle of QuasAr6a. Future experiments with improved delay line stability and broader sensitivity detection could provide more insights in the complex mechanisms underlying fluorescence generation and voltage sensitivity. The combinations tested in the parameter space were very limited, and a lot of potential still lies in the systematic exploration of this space.

Although the focus of this dissertation revolved around QuasAr6a, the methodologies developed are broadly applicable to virtually any fluorophore that undergoes a photo-

cycle. Extending the approach to other genetically encoded voltage indicators or even different classes of light-sensitive proteins could lead to new non-invasive tools for measuring and controlling cellular behavior. Comparative studies across different protein families may reveal universal principles governing the interaction between non-linear excitations and protein photocycle dynamics.

The convergence of optics, nanotechnology and biology in this work highlights the importance of an holistic, interdisciplinary approach to science. The logical evolution of this research is then the direct combination of plasmonic enhancement and ultrafast excitation to manipulate the photocycle (Fig. 6.2). While this dissertation explored these approaches separately, their synergistic application could offer a fundamentally new way to control protein function. One possible strategy is to exploit plasmonic resonances to locally enhance not only the excitation of the fluorophore, but also its interaction with ultrafast pulses. This could be leveraged to enhance specific transitions, thereby modulating brightness, response time and even voltage sensitivity in a way that is not possible with either technique alone.

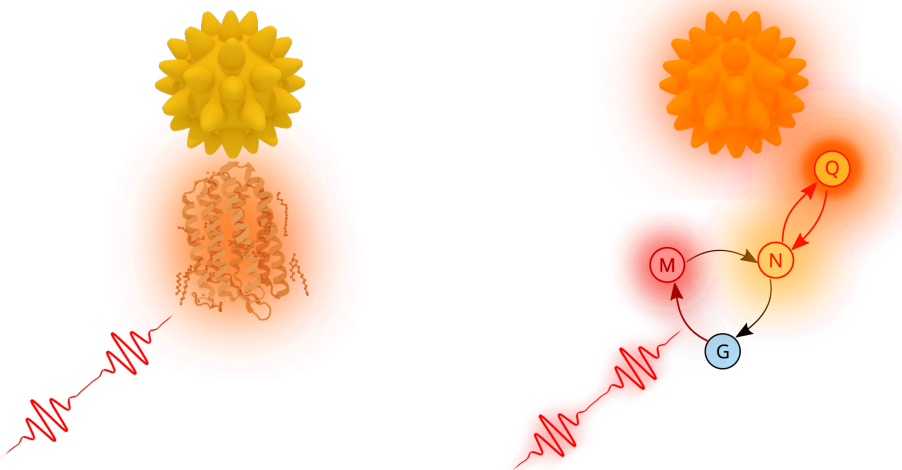


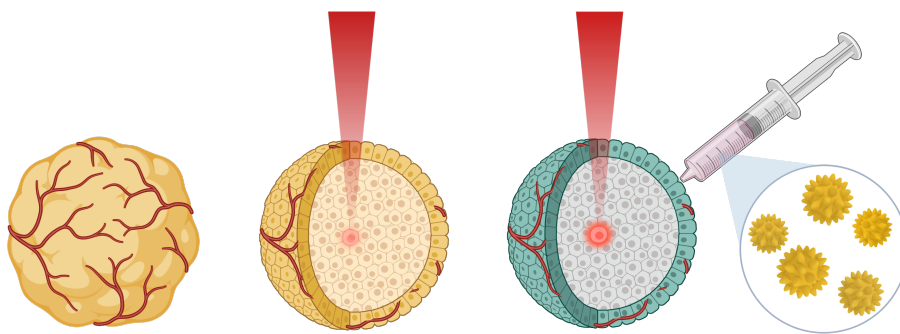
Figure 6.2: Schematic illustrating the synergy of plasmonic field enhancement and ultrafast optical excitation in modulating the QuasAr6a photocycle. The plasmonic nanostar locally amplifies the excitation field around the protein, while the ultrafast pump-probe approach selectively targets specific transitions, enabling precise control over fluorescence brightness, response kinetics and voltage sensitivity.

6.3. SOCIETAL IMPACT

The advancements presented in this thesis have far-reaching implications not only for science, but for society as well. At a fundamental level, the work deepens the understanding of light-matter interactions at the nanoscale in physiologically relevant environments, and offers new strategies for manipulating biological function through physical means. Multiple fields would greatly benefit from this knowledge.

NANOSCOPIC VOLTAGE IMAGING OF NEUROLOGICAL DISEASES

Perhaps the most obvious consequence of enabling brighter and faster fluorescent signals, by bridging plasmonic field enhancement with ultrafast spectroscopy, is the development of an entirely new form of all-optical control over GEVIs. This is extremely relevant for expanding their potential to advanced neuroscience applications. In particular, multiphoton voltage imaging offers a platform for real-time, high-resolution monitoring of neuronal activity deep within living tissue, either *in vivo* or in organoid models (Fig. 6.3). By combining the deep penetration and reduced phototoxicity of multiphoton techniques with the enhanced signal strength provided by plasmonic nanostructures, one could visualize subcellular voltage dynamics with unprecedented clarity. Such advances could shed light on the underlying mechanisms of neurodegenerative diseases, such as epilepsy, Alzheimer's and Parkinson's,^{8,9} and ultimately inform the development of targeted therapeutic strategies.¹⁰



6

Figure 6.3: Application of the combined approach in neural tissue can enhance the dim signal of GEVIs deep in the organoid core. Illustration made in BioRender.

NON-INVASIVE CONTROL OF CELLULAR PROCESSES WITH LIGHT

The ability to manipulate the photocycle of light-sensitive proteins through physical interventions without altering the genetic makeup of cells opens up new opportunities for non-invasive control of cellular functions. Unlike genetic modifications, which are typically irreversible and may incur off-target effects or immune responses, physical approaches offer reversible and finely tunable modulation.¹¹ For example, plasmonic enhancement techniques can amplify local electromagnetic fields, thereby dynamically altering the excitation and de-excitation processes of these proteins.^{12,13} Similarly, ultrafast pulse shaping would enable precise control over the timing of phototransitions, allowing selective enhancement (or suppression) of specific steps in the photocycle.^{14,15,16} In neurological disorders such as epilepsy or cardiac arrhythmia, where abnormal electrical activity causes the pathology, the ability to reversibly modulate protein function with light could provide targeted treatments that avoid the risks associated with permanent genetic alterations.¹¹

SCALABLE TECHNOLOGIES

The approaches outlined in this thesis, from plasmonic enhancement to non-linear excitation, are inherently scalable. Recent advancements in nanoparticle synthesis now enable the production of uniform plasmonic nanospheres on an industrial scale,¹⁷ with machine learning promising to solve the bottlenecks in the synthesis of more exotic morphologies.¹⁸ Similarly, high-throughput 2-photon imaging techniques involving multifocal approaches and advanced scanning mechanisms have been developed.¹⁹ These techniques enhance imaging speed and efficiency, allowing simultaneous detection of multiple focal planes, thus improving overall imaging throughput. This enables rapid analysis of thousands of samples in a relatively short time, a capability that is indispensable in fields such as drug discovery and biomedical diagnostics. Together, these scalable techniques lay the groundwork for next-generation technologies that could address real-world challenges in healthcare.

COMMERCIAL AND TRANSLATIONAL OPPORTUNITIES

This work presents significant potential for commercial and translational applications. For instance, the optical delay line developed in this project could be packaged as an add-on for other advanced microscopy systems. By offering precise control over ultrafast pulse timing, it could enhance a wide range of imaging techniques. Similarly, properly functionalized plasmonic nanoparticles have applications in nanomedicine, a rapidly growing field. Their ability to enhance fluorescence and modulate protein function could lead to the development of new biosensing platforms or therapeutic tools, especially in fields requiring high sensitivity and rapid response, or even be integrated in lab-on-a-chip devices. Furthermore, an important guiding principle in this thesis was that of open science. Key analysis and modeling software has been released open-source, not only encouraging collaboration but also providing educational tools that help train the next generation of scientists. In this context, this research can catalyze broader innovation. The integration of these tools into commercial products and diagnostic platforms may drive growth across multiple sectors, from biomedical research to industrial applications, contributing to healthcare and economic advancement.

6.4. CONCLUDING REMARKS

In reflecting on the journey that this thesis represents, one never stops being amazed by how crossing disciplinary boundaries is the most effective way forward in science. This thesis tells the story of how a deeper understanding of physics, from plasmonic nanophotonics to ultrafast dynamics, can guide the improvement of the tools available for measuring and controlling biological processes. In this sense, the manipulation of the photocycle through physical means was not merely an academic exercise: it is a step toward a future where the limits of biological function can be redefined by the precision of modern optics and nanotechnology, rather than by the structure of a biomolecule. As the field moves forward, the hope is that these strategies will push for a transformative shift in biomedical sciences, one that prioritizes non-invasive, reversible and highly tunable interventions for probing the mysteries of the brain and other biological systems.

This journey has come to an end, but for biophysics an exciting adventure, made of plasmonically enhanced biosensors and ultrafast pump-probe excitations, nanotechnology and non-linear optics, innovation and interdisciplinarity, has just begun.

BIBLIOGRAPHY

- [1] John Jumper et al. "Highly accurate protein structure prediction with AlphaFold". In: *Nature* 596.7873 (2021). ISSN: 14764687. DOI: [10.1038/s41586-021-03819-2](https://doi.org/10.1038/s41586-021-03819-2).
- [2] Daniela Rus and Michael T. Tolley. "Design, fabrication and control of soft robots". In: *Nature* 521.7553 (2015). ISSN: 14764687. DOI: [10.1038/nature14543](https://doi.org/10.1038/nature14543).
- [3] Mikhail A. Lebedev and Miguel A.L. Nicolelis. "Brain-machine interfaces: From basic science to neuroprostheses and neurorehabilitation". In: *Physiological Reviews* 97.2 (2017). ISSN: 15221210. DOI: [10.1152/physrev.00027.2016](https://doi.org/10.1152/physrev.00027.2016).
- [4] Samuel K. Sia and Larry J. Kricka. *Microfluidics and point-of-care testing*. 2008. DOI: [10.1039/b817915h](https://doi.org/10.1039/b817915h).
- [5] John Peurifoy et al. "Nanophotonic particle simulation and inverse design using artificial neural networks". In: *Science Advances* 4.6 (2018). ISSN: 23752548. DOI: [10.1126/sciadv.aar4206](https://doi.org/10.1126/sciadv.aar4206).
- [6] Rafael Yuste. "Electrical compartmentalization in dendritic spines". In: *Annual Review of Neuroscience* 36 (2013). ISSN: 0147006X. DOI: [10.1146/annurev-neuro-062111-150455](https://doi.org/10.1146/annurev-neuro-062111-150455).
- [7] Lou Beaulieu-Laroche and Mark T. Harnett. "Dendritic Spines Prevent Synaptic Voltage Clamp". In: *Neuron* 97.1 (2018). ISSN: 10974199. DOI: [10.1016/j.neuron.2017.11.016](https://doi.org/10.1016/j.neuron.2017.11.016).
- [8] Leslie Crews and Eliezer Masliah. "Molecular mechanisms of neurodegeneration in Alzheimer's disease". In: *Human Molecular Genetics* 19.R1 (2010). ISSN: 09646906. DOI: [10.1093/hmg/ddq160](https://doi.org/10.1093/hmg/ddq160).
- [9] Katarzyna Lepeta et al. "Synaptopathies: synaptic dysfunction in neurological disorders – A review from students to students". In: *Journal of Neurochemistry* (2016). ISSN: 14714159. DOI: [10.1111/jnc.13713](https://doi.org/10.1111/jnc.13713).
- [10] Khushi R. Mittal et al. "Nanotechnology-based drug delivery for the treatment of CNS disorders". In: *Translational Neuroscience* 13.1 (2022). ISSN: 20816936. DOI: [10.1515/tnsci-2022-0258](https://doi.org/10.1515/tnsci-2022-0258).
- [11] Haichao Zhao et al. "Modulation of brain activity with noninvasive transcranial direct current stimulation (tDCS): Clinical applications and safety concerns". In: *Frontiers in Psychology* 8.MAY (2017). ISSN: 16641078. DOI: [10.3389/fpsyg.2017.00685](https://doi.org/10.3389/fpsyg.2017.00685).

- [12] Stephan Link and Mostafa A. El-Sayed. "Spectral Properties and Relaxation Dynamics of Surface Plasmon Electronic Oscillations in Gold and Silver Nanodots and Nanorods". In: *Journal of Physical Chemistry B* 103.40 (1999). ISSN: 15206106. DOI: [10.1021/jp9917648](https://doi.org/10.1021/jp9917648).
- [13] Daan Brinks et al. "Plasmonic antennas as design elements for coherent ultrafast nanophotonics". In: *Proceedings of the National Academy of Sciences of the United States of America* 110.46 (2013). ISSN: 00278424. DOI: [10.1073/pnas.1308652110](https://doi.org/10.1073/pnas.1308652110).
- [14] Richard Hildner, Daan Brinks, and Niek F. Van Hulst. "Femtosecond coherence and quantum control of single molecules at room temperature". In: *Nature Physics* 7.2 (2011). ISSN: 17452481. DOI: [10.1038/nphys1858](https://doi.org/10.1038/nphys1858).
- [15] Richard Hildner et al. "Electronic coherences and vibrational wave-packets in single molecules studied with femtosecond phase-controlled spectroscopy". In: *Physical Chemistry Chemical Physics* 13.5 (2011). ISSN: 14639076. DOI: [10.1039/c0cp02231d](https://doi.org/10.1039/c0cp02231d).
- [16] Daan Brinks et al. "Ultrafast dynamics of single molecules". In: *Chemical Society Reviews* 43.8 (2014). ISSN: 14604744. DOI: [10.1039/c3cs60269a](https://doi.org/10.1039/c3cs60269a).
- [17] Hiroki Hiramatsu and Frank E. Osterloh. "A simple large-scale synthesis of nearly monodisperse gold and silver nanoparticles with adjustable sizes and with exchangeable surfactants". In: *Chemistry of Materials* 16.13 (2004). ISSN: 08974756. DOI: [10.1021/cm049532v](https://doi.org/10.1021/cm049532v).
- [18] Huachen Tao et al. "Nanoparticle synthesis assisted by machine learning". In: *Nature Reviews Materials* 6.8 (2021). ISSN: 20588437. DOI: [10.1038/s41578-021-00337-5](https://doi.org/10.1038/s41578-021-00337-5).
- [19] Ramón Carriles et al. "Invited Review Article: Imaging techniques for harmonic and multiphoton absorption fluorescence microscopy". In: *Review of Scientific Instruments* 80.8 (2009). ISSN: 00346748. DOI: [10.1063/1.3184828](https://doi.org/10.1063/1.3184828).

CURRICULUM VITÆ

Marco LOCARNO

18-04-1995 Born in Genova, Italy.

EDUCATION

2009–2014	Diploma in Electronics and Telecommunications Istituto di Istruzione Superiore Italo Calvino, Genova, Italy
2014–2017	BSc. in Physics Università degli Studi di Genova, Genova, Italy
2017–2019	MSc. in Physics Università degli Studi di Genova, Genova, Italy

PROFESSIONAL EXPERIENCE

2020–2024	PhD candidate in Physics Delft University of Technology, Delft, The Netherlands <i>Thesis:</i> Finding light in the darkness <i>Supervisor:</i> Dr.ir. D. Brinks
2023–Today	Biophysics Lecturer Utrecht University, Utrecht, The Netherlands

QUALIFICATIONS

- University Teaching Qualification (UTQ) - June 2023
- Laboratory Animal Science (Basic course) - September 2020
- Laboratory Animal Science (Rodents and Rabbits) - September 2020

PUBLICATIONS

Marco Locarno. "Cultured Human Meat Acceptability: From Inviolability of Human Body to Prevention of Induced Human Meat Craving". *Food Ethics* (2023).

DOI: 10.1007/s41055-023-00121-x

Marco Locarno, Daan Brinks. "Analytical calculation of plasmonic resonances in metal nanoparticles: a simple guide". *American Journal of Physics* (2023).

DOI: 10.1119/5.0094967

Marco Locarno, Qiangrui Dong, Xin Meng, Cristiano Glessi, Daan Brinks. "Fluorescence enhancement of fluorophores in live cells using metallic nanoparticles". *Proceedings SPIE, Neurophotonics II* (2024).

DOI: 10.1117/12.3017177

Marco Locarno, Qiangrui Dong, Xin Meng, Cristiano Glessi, Nynke Marije Hettema, Nidas Brandsma, Sebbe Blokhuizen, Alejandro Castañeda Garcia, Thieme Schmidt, Srividya Ganapathy, Marco Post, Lars van Roemburg, Bing Xu, Chun-Ting Cho, Liedewij Laan, Miao-Ping Chien, Daan Brinks. "Plasmonic Enhancement of Protein Function". Submitted to *Advanced Materials* (2025).

DOI: 10.1101/2024.02.07.579195 (preprint)

ACKNOWLEDGEMENTS



“La vita non ha narrativamente senso” afferma la citazione all’inizio di questa tesi, selezionata da una delle mie serie TV preferite in quanto ottimo riassunto degli scorsi cinque anni e mezzo. Ricordo a chi legge che ho iniziato questo mio ultimo percorso accademico nel Febbraio 2020. Un mese dopo, il grande shock che è stata la pandemia, la quale ha scombusolato i piani e cambiato radicalmente le traiettorie delle nostre vite. Sono convinto che, senza quegli ostacoli e imprevisti, il mio percorso di crescita forse non sarebbe nemmeno iniziato. Se la mia vita avesse avuto “narrativamente senso”, non sarei la persona che sono oggi. Eppure, non sono grato per il periodo cupo che ha seguito il periodo forse migliore della mia vita, ma sono grato delle molte persone che hanno reso quel periodo quantomeno sopportabile. Quindi eccomi qui, a scrivere di getto una serie di ringraziamenti che senso narrativo non hanno, ma che non per questo sono meno sinceri.

La prima persona che mi viene in mente se ripenso all’inizio del dottorato è sicuramente **Chiara**. A dire il vero, lei è la persona che mi viene in mente in moltissime altre occasioni, per cui sarebbe scorretto associarla solamente al momento in cui ci siamo davvero ritrovati. Abitavi a cinquanta metri da casa mia, eppure ci siamo conosciuti solo alla fine delle elementari. Chissà se quel cuore fatto in DAS per San

“Life doesn’t make narrative sense” states the quote at the beginning of this thesis, taken from one of my favorite TV series as a fitting summary of the past five and a half years. Let me remind the reader that I began this final academic journey in February 2020. One month later came the great shock of the pandemic, which disrupted plans and radically changed the trajectories of our lives. I’m convinced that, without those obstacles and unforeseen events, my path of growth might never have even begun. If my life had had “narrative sense”, I wouldn’t be the person I am today. And yet, I am not grateful for the bleak times that followed perhaps the best period of my life, but I am grateful for the many people who made that time at least bearable. So here I am, spontaneously writing a series of acknowledgements that have no narrative sense, but aren’t for this reason less sincere.

The first person that comes to mind when I think back to the beginning of my PhD is undoubtedly **Chiara**. To be honest, she’s the person that comes to mind on many other occasions too, so it wouldn’t be fair to associate her only with the moment we truly reconnected. You lived just fifty meters from my house, and yet we only met at the end of primary school. Who knows if that heart made of clay for Valen-

Valentino andava letto come un segno che saresti diventata la mia amica del cuore. La vita ci ha portato su percorsi diversi per molti anni, come a volerci prima far fare una scorpacciata di esperienze per poi farci sbattere su un treno verso Brignole e dirci “ecco, ora potete condividere quello che avete imparato”. Grazie, insomma, a KLM per avere cancellato tre voli e aver così consolidato un’amicizia che porterò nel cuore per sempre. Hai visto tutto il mio percorso da allora ad oggi, e non vorrei nessun altro al tuo posto come testimone di dottorato. Sei una sorella per me.

Se Chiara ha assistito principalmente alla mia crescita emotiva, 鑫 (per gli amici, **Xin**) è stato testimone della mia crescita intellettuale. Ero davvero un bambino quando mi hai conosciuto, credevo di sapere tutto della vita e della scienza. Tu non hai mai contrastato le mie convinzioni, ma al contrario ti sei seduto di fianco a me e hai ascoltato con empatia tutto quello che avevo da dire. Da colleghi abbiamo imparato cosa significhi essere scienziati, da coquinilini abbiamo imparato cosa significhi l’amicizia. Sei un amico leale, sincero, che capisce quando è il momento di tirare fuori il gelato dal freezer mentre stai piangendo e quando è il momento di rimanere in ufficio un po’ più a lungo in attesa di un messaggio WhatsApp. Grazie per la nostra amicizia.

Un sincero *bedankt* è dovuto al vero motivo per cui mi sono ritrovato a Delft e non in altre parti del mondo, il mio supervisore **Daan**. È bastato chiedermi se volessi tornare nel tuo laboratorio, e a me è bastato rispondere “sì” in un pomeriggio di Settembre. Hai sempre fatto del tuo meglio per far muovere i macchinosi processi burocratici in mio favore, in modo che potessi concentrarmi solo sulla sostanza del mio incarico. Grazie per avere supportato le mie decisioni accademiche,

tine’s Day was a sign that you’d become my best friend. Life took us on separate paths for many years, as if it wanted us to first gorge ourselves on experience before throwing us onto a train headed for Brignole and saying, “there, now you can share what you’ve learned”. So thank you, in short, to KLM for cancelling three flights and thus helping to solidify a friendship I will always carry in my heart. You’ve seen my whole journey from then to now, and I wouldn’t want anyone else but you as my paranympth. You are a sister to me.

If Chiara mostly witnessed my emotional growth, 鑫 (to friends, **Xin**) was a witness to my intellectual growth. I was truly a child when you met me, I thought I knew everything about life and science. You never challenged my convictions directly; instead, you sat next to me and listened with empathy to everything I had to say. As colleagues, we learned what it means to be scientists; as flatmates, we learned what friendship means. You are a loyal and sincere friend, who knows when it’s time to pull the ice cream out of the freezer while someone is crying, and when it’s time to stay in the office a bit longer waiting for a WhatsApp message. Thank you for our friendship.

A sincere *bedankt* is due to the real reason I ended up in Delft and not elsewhere in the world: my supervisor **Daan**. It only took you asking whether I wanted to come back to your lab, and it only took me saying “yes” on a September afternoon. You always did your best to set the slow bureaucratic gears in motion in my favor, so that I could focus solely on the substance of my position. Thank you for supporting my academic decisions, for paving the way for my projects without trying to change their

per aver spianato la strada ai miei progetti senza tentare di cambiarne la direzione, per avermi permesso di parlarti come un pari anche in caso di disaccordo. Senza il tuo supporto non avrei mai ottenuto il lavoro dei miei sogni prima ancora di finire il dottorato.

Inevitabile a questo punto il ringraziamento al dipartimento di Imaging Physics che mi ha ospitato, al suo fantastico capo nonché mio promotore **Jacob**, e al resto del Brinks Lab e “affini”. Grazie a **Florian** e **Hylkje** per le possibilità di insegnamento fin dall'inizio del dottorato. Grazie a **Nicolò** per il tuo grande cuore e la tua grande intelligenza che, come per tutti i “grandi”, si esprime sempre come affilato umorismo. Grazie a **Vidya** per tutto l'amore incondizionato che hai riversato nella nostra amicizia, per gli abbracci sinceri, per la cura che ti sei presa di me anche quando non me ne accorgevo. Grazie ad **Alejandro** per il tempo assieme, per la sensibilità e la comprensione reciproca, sempre. Grazie a **Mike** per l'affetto, l'empatia, le nostre profonde discussioni sulla vita, e la certezza di un'amicizia che, anche ad intermittenza, c'è sempre nel momento del bisogno. Grazie a **Cristiano** per le risate e la leggerezza, ma anche i preziosi consigli sul mondo accademico. Grazie a **Marco**, con cui non condivido praticamente nessuna idea (specie quelle controverse sul cibo!!!), per aver reso le nostre discussioni sempre stimolanti, accese, provocatorie e, più di tutto, divertenti, ma grazie anche per la tua immensa disponibilità in laboratorio di cui spero di non avere abusato. Grazie ad **Arent** per avermi scelto come testimone di dottorato, per tutti i caffè per cui si deve aspettare, per l'aiuto nella nuova casa in un periodo così complicato. Grazie ad **Huma**, **Apilena** e **Mariska**, per le chiacchiere in amicizia e per il preziosissimo aiuto tecnico in laboratorio. Grazie ai miei pazzi

direction, and for allowing me to speak to you as an equal, even when in disagreement. Without your support, I would have never landed the job of my dreams before even finishing my PhD.

At this point, it's inevitable to thank the Imaging Physics department that hosted me, its fantastic head and my promotor **Jacob**, as well as the rest of the Brinks Lab and its “peers”. Thanks to **Florian** and **Hylkje** for the teaching opportunities from the very beginning of the PhD. Thanks to **Nicolò** for your big heart and sharp mind, which, like for all the “great ones”, always shows through witty humor. Thanks to **Vidya** for all the unconditional love you poured into our friendship, for the heartfelt hugs, and for the care you took of me even when I wasn't noticing. Thanks to **Alejandro** for the time spent together, for your sensitivity and our mutual understanding, always. Thanks to **Mike** for your affection, empathy, our deep conversations about life, and the certainty of a friendship that, even if intermittent, is always there when needed. Thanks to **Cristiano** for the laughs and lightness, but also for your valuable advice on the academic world. Thanks to **Marco**, with whom I practically share no opinion at all (especially your controversial ones about food!!!), for making our discussions always stimulating, heated, provocative, and, above all, fun, but also thank you for your immense availability in the lab, which I hope I didn't take too much advantage of. Thanks to **Arent** for choosing me as your paranympth, for all the coffees worth waiting for, and for your help with my new home during such a difficult period. Thanks to **Huma**, **Apilena**, and **Mariska** for the friendly chats and the incredibly valuable technical support in the lab. Thanks to my crazy office mates, **Laura** and **Martijn**;

compagni di ufficio, **Laura** e **Martijn**; alla prima per aver sopportato i miei scleri, per tutto il cibo buonissimo cucinato assieme e per le risate con le lacrime; al secondo per aver reso gli ultimi anni di dottorato divertenti e mai monotoni, per i tuoi collegamenti illogici e per i nostri intensissimi dibattiti anche se eravamo d'accordo quasi sempre. Sei praticamente la versione di Marco in antimateria, ora che ci penso. Grazie a tutti voi e a chi non è qui esplicitamente nominato per aver reso il laboratorio e l'ufficio dei posti a me così cari e familiari.

Un ringraziamento speciale a parte va alla mia carissima amica e collega 珍珍 **Zhenzhen**, che ha condiviso gran parte delle gioie e dei dolori del dottorato assieme a me. Assieme al mitico 定浩 **Dinghao** abbiamo passato innumerevoli serate a ridere, sfogarci, piangere, parlare delle nostre vite. Avete conosciuto la mia città e i miei genitori, dove sarete per sempre i benvenuti. Nonostante tutti i momenti difficili ci siamo sempre fatti forza e rialzati, e sono onorato di potervi chiamare “casa lontano da casa”.

Lo stesso affetto incondizionato lo dedico ai miei portoghesi preferiti, **Rui** e **Catarina**. Abbiamo condiviso con noi il nostro piccolo appartamento qualche anno fa, e da allora ci siamo conosciuti ad un livello più profondo. Nel momento del bisogno ci siete sempre, ed è meraviglioso vedere come stiamo tutti crescendo in adulti che ogni tanto giocano ancora a fare i ragazzini. Vi voglio bene.

Voglio anche ringraziare tutti coloro che hanno contribuito a rendere i Paesi Bassi un posto che posso chiamare casa. In particolare ringrazio la fantastica delegazione genovese di **Andrea**, **Benedetta**, **Bruk** e **Amalia**, che rende sempre ogni incontro una festa. **Can** e **Robin**, che ho incontrato più tardi nel mio percorso acca-

to the former for putting up with my melt-downs, for all the amazing food we cooked together, and for the tears of laughter; to the latter for making the final years of the PhD fun and never monotonous, for your illogical associations, and for our intense debates, even though we actually agreed on almost everything. You're basically the antimatter version of Marco, now that I think about it. Thanks to all of you and to those not explicitly named here, for making the lab and the office such dear and familiar places to me.

A special thanks goes to my dear friend and colleague 珍珍 **Zhenzhen**, who shared much of the joy and pain of the PhD with me. Together with the legendary 定浩 **Dinghao**, we spent countless evenings laughing, venting, crying, and talking about our lives. You got to know my city and my parents, where you will always be welcome. Despite all the difficult times, we always supported each other and got back on our feet, and I am honored to be able to call you “home away from home”.

The same unconditional affection goes to my favorite Portuguese friends, **Rui** and **Catarina**. You shared our little apartment with us a few years ago, and since then we've gotten to know each other on a much deeper level. You're always there in times of need, and it's wonderful to see how we're all growing into adults who still sometimes play at being kids. I love you both.

I also want to thank everyone who helped make the Netherlands a place I can call home. In particular, I thank the fantastic Genoese delegation of **Andrea**, **Benedetta**, **Bruk**, and **Amalia**, who always turn every gathering into a celebration. **Can** and **Robin**, whom I met later in my academic journey, but with whom I imme-

demico, ma con cui ho fin da subito creato una sincera amicizia. **Jillian**, non solo per prendersi cura di quello stordito del mio amico nonché suo compagno, ma anche per il tempo piacevole passato assieme. E sempre in questo gruppo ringrazio **Vadim** e **Nastya** perché da una conferenza abbiamo creato un rapporto sincero in cui possiamo parlare davvero di qualsiasi cosa.

Un enorme supporto ed interminabile affetto l'ho ricevuto anche da chi non ha mai smesso di fare il tifo per me da Genova: **Alba**, **Beatrice**, **Denise**, **Daniele**, **Erica** (che di tutte le Eriche esistenti al mondo tecnicamente a Genova non abita più) ed in generale tutti gli affiatati membri del **Partito del Nocciovino** che resiste nonostante ognuno di noi abbia ormai preso una strada diversa. Ma da Genova l'affetto non ha mai smesso di arrivare anche da **Valentina** e **Marta**, che lo hanno portato per qualche giorno proprio qua, e da **Alice** ed **Esther**, su cui so che posso contare in qualsiasi momento anche tramite un semplice messaggio.

Se ho imparato a convivere con la mancanza di senso narrativo nella vita è solamente grazie a **Serena**, mia psicologa e psicoterapeuta, che voglio ringraziare di cuore. Negli ultimi due anni e mezzo sei stata e continui ad essere per me una preziosissima guida, un porto sicuro quando il mare è in tempesta, una lente puntata sui lati di me che non riuscivo a mettere a fuoco, una mappa nel labirinto della vita, l'Omero della mia Odissea. Ti sono grato perché grazie a te non solo ho ritrovato chi sono, ma sto diventando chi posso essere.

Infine, voglio ringraziare i miei genitori per avermi supportato e mai ostacolato nella ricerca del mio posto nel mondo, anche se era lontano da loro. Crescendo si scopre che nessuno ha mai tutti gli strumenti per affrontare la vita, e che si possono solo prendere in prestito quelli degli

diately formed a genuine friendship. **Jillian**, not only for taking care of that scatterbrained friend of mine—who also happens to be her partner—but also for the enjoyable time we've spent together. And still within this group, I thank **Vadim** and **Nastya**, because from a single conference we built a sincere bond where we can truly talk about anything.

I also received enormous support and endless affection from those who never stopped cheering for me from Genova: **Alba**, **Beatrice**, **Denise**, **Daniele**, **Erica** (who, of all the Ericas in the world, technically no longer lives in Genova), and in general all the tight-knit members of the **Partito del Nocciovino**, which lives on despite each of us having now taken a different path. But affection from Genova has also continued to arrive from **Valentina** and **Marta**, who even brought it here in person for a few days, and from **Alice** and **Esther**, whom I know I can always count on, even with just a simple message.

If I've learned to live with the lack of narrative sense in life, it is only thanks to **Serena**, my psychologist and psychotherapist, whom I want to thank from the bottom of my heart. Over the past two and a half years, you have been and continue to be a most precious guide, a safe harbor when the sea is stormy, a lens pointing on the parts of me I couldn't bring into focus, a map through the maze of life, the Homer to my Odyssey. I am grateful to you, because thanks to you I have not only found myself again, but I am becoming who I can be.

Finally, I want to thank my parents for supporting me and never standing in the way as I searched for my place in the world, even if it meant being far from them. Growing up, one discovers that no one ever has all the tools to face life, and that you can only borrow those of others until you craft

altri finché non si preparano i propri. Grazie per aver attentamente scelto dal vostro bagaglio gli strumenti che meglio pensate fossero per me, a volte facendo un lavoro titanico per non ripetere gli sbagli delle generazioni prima di voi, a volte inciampando, ma mai smettendo di provarci. A volte comprendete le mie scelte, a volte no, ma stiamo imparando che va bene così. Grazie **papà** per avere riconosciuto il mio bisogno di indipendenza e aver fatto ogni tanto un passo indietro, per quanto molte volte sarebbe stato più facile aspettarsi che io agissi come avresti fatto tu, così simili siamo per carattere, ambizioni e situazioni della vita. Grazie **mamma** per tutto l'affetto silenzioso che sottintendi quando brontoli che "non ci sentiamo mai", quando mi chiedi di mandarti un vocale dicendo come sto, quando ti preoccupi se ho preso l'Aerius per l'allergia. Non ve lo dico abbastanza spesso, e mi scuso di questo, ma vi voglio un bene infinito e siete per me l'universo.

Grazie anche al mio fratellone **Luca**, che non ha mai per un momento dubitato di me né giudicato chi fossi e cosa facessi, anche se siamo diversi come il giorno e la notte. Grazie a **Lina** per l'affetto, sia quando ci vediamo sia quando siamo a distanza, e grazie a **Nicole** per ricordarmi quanto è bello essere bambini. A lei auguro anche di trovare sempre il divertimento nello studio, perché con la sua curiosità continuo a pensare un giorno seguirà i miei passi.

La persona più speciale l'ho tenuta per ultima, il mio amore **Ferhat**. *Aşkim, kalbim*, sei stato e sei per me una luce buio, ti sei preso cura di me e grazie all'amore che mi hai donato io sono la persona che vedi oggi. In questo mio successo, un po' ci sei anche tu. Non vedo l'ora di iniziare un nuovo capitolo della mia vita al tuo fianco. Grazie di esistere.

your own. Thank you for carefully choosing from your own toolkit the tools you thought were best for me, sometimes making a titanic effort not to repeat the mistakes of the generations before you, sometimes stumbling, but never ceasing to try. Sometimes you understand my choices, sometimes you don't, but we are learning that that's okay. Thank you, **dad**, for recognizing my need for independence and occasionally taking a step back, even when it might have been easier to expect me to act as you would have, so similar we are in character, ambition, and life circumstances. Thank you, **mom**, for all the silent affection you express when you complain that "we never talk", when you ask me to send a voice message to tell how I'm doing, when you worry about whether I've taken Aerius for my allergy. I don't say it often enough, and I'm sorry for that, but I love you endlessly, and you are my whole universe.

Thanks also to my big brother **Luca**, who has never for a moment doubted me or judged who I am and what I do, even though we are as different as night and day. Thanks to **Lina** for your affection, both when we see each other and when we're apart, and thanks to **Nicole** for reminding me how beautiful it is to be a child. I also wish for her to always find joy in learning, because with her curiosity, I keep thinking that one day she'll follow in my footsteps.

I saved the most special person for last: my love, **Ferhat**. *Aşkim, kalbim*, you have been, and still are, a light in the darkness for me. You took care of me, and thanks to the love you gave me, I am the person you see today. In this success of mine, there is a part of you, too. I can't wait to start a new chapter of my life by your side. Thank you for existing.

